AFRL-ML-WP-TR-2004-4237

RESEARCH ON ADVANCED NONDESTRUCTIVE EVALUATION (NDE) METHODS FOR AEROSPACE STRUCTURES

Thomas Boehnlein, Jeffrey Fox, Brian Frock, Edward Klosterman, Dr. Ray Ko, Dr. Victoria Kramb, Richard Martin, Dr. Theodoras Matikas, Richard Reibel, Mark Ruddell, Dr. Shamachary Sathish, Dr. James Blackshire, Adam Cooney, Christopher Kacmar, and Sonya Martinez

University of Dayton Research Institute
300 College Park
Dayton, OH 45469-0120

Courtney Daniels, Dr. Nicola Dusaussoy, and Trent Neel

Advanced Research and Applications Corporation (ARACOR)

Dr. Yellapregada Prasad (consultant)

MARCH 2004

Final Report for 30 September 1998 – 31 December 2003

STINFO FINAL REPORT

MATERIALS AND MANUFACTURING DIRECTORATE
AIR FORCE RESEARCH LABORATORY
AIR FORCE MATERIEL COMMAND
WRIGHT-PATTERSON AIR FORCE BASE, OH 45433-7750

NOTICE

Using government drawings, specifications, or other data included in this document for any purpose other than government procurement does not in any way obligate the U.S. Government. The fact that the government formulated or supplied the drawings, specifications, or other data does not license the holder or any other person or corporation; or convey any rights or permission to manufacture, use, or sell any patented invention that may relate to them.

This report has been reviewed by the Office of Public Affairs (ASC/PA) and is releasable to the National Technical Information Service (NTIS). At NTIS, it will be available to the general public, including foreign nationals.

This technical report has been reviewed and is approved for publication.

/s/

_____
CLAUDIA KROPAS-HUGHES
Project Engineer
Nondestructive Evaluation Branch
Metals, Ceramics & NDE Division

/s/

_____
JAMES C. MALAS, Chief
Metals Branch
Metals, Ceramics & NDE Division

/s/

_____
GERALD J. PETRAK, Assistant Chief
Metals, Ceramics & NDE Division
Materials & Manufacturing Directorate

REPORT DOCUMENTATION PAGE			*Form Approved* *OMB No. 0704-0188*

The public reporting burden for this collection of information is estimated to average 1 hour per response, including the time for reviewing instructions, searching existing data sources, searching existing data sources, gathering and maintaining the data needed, and completing and reviewing the collection of information. Send comments regarding this burden estimate or any other aspect of this collection of information, including suggestions for reducing this burden, to Department of Defense, Washington Headquarters Services, Directorate for Information Operations and Reports (0704-0188), 1215 Jefferson Davis Highway, Suite 1204, Arlington, VA 22202-4302. Respondents should be aware that notwithstanding any other provision of law, no person shall be subject to any penalty for failing to comply with a collection of information if it does not display a currently valid OMB control number. **PLEASE DO NOT RETURN YOUR FORM TO THE ABOVE ADDRESS**.

1. REPORT DATE *(DD-MM-YY)* March 2004	2. REPORT TYPE Final	3. DATES COVERED *(From - To)* 09/30/1998 – 12/31/2003

4. TITLE AND SUBTITLE RESEARCH ON ADVANCED NONDESTRUCTIVE EVALUATION (NDE) METHODS FOR AEROSPACE STRUCTURES	5a. CONTRACT NUMBER F33615-98-C-5217
	5b. GRANT NUMBER
	5c. PROGRAM ELEMENT NUMBER 62102F

6. AUTHOR(S) Thomas Boehnlein, Jeffrey Fox, Brian Frock, Edward Klosterman, Dr. Ray Ko, Dr. Victoria Kramb, Richard Martin, Dr. Theodoras Matikas, Richard Reibel, Mark Ruddell, Dr. Shamachary Sathish, Dr. James Blackshire, Adam Cooney, Christopher Kacmar, and Sonya Martinez (UDRI) Courtney Daniels, Dr. Nicola Dusaussoy, and Trent Neel (ARACOR) Dr. Yellapregada Prasad (consultant)	5d. PROJECT NUMBER 4349
	5e. TASK NUMBER 44
	5f. WORK UNIT NUMBER 03

7. PERFORMING ORGANIZATION NAME(S) AND ADDRESS(ES) University of Dayton Research Institute / 300 College Park / Dayton, OH 45469-0120 Advanced Research and Applications Corporation (ARACOR)	8. PERFORMING ORGANIZATION REPORT NUMBER UDR-TR-2004-00026

9. SPONSORING/MONITORING AGENCY NAME(S) AND ADDRESS(ES) Materials and Manufacturing Directorate Air Force Research Laboratory Air Force Materiel Command Wright-Patterson AFB, OH 45433-7750	10. SPONSORING/MONITORING AGENCY ACRONYM(S) AFRL/MLLP
	11. SPONSORING/MONITORING AGENCY REPORT NUMBER(S) AFRL-ML-WP-TR-2004-4237

12. DISTRIBUTION/AVAILABILITY STATEMENT
Approved for public release; release is unlimited.

13. SUPPLEMENTARY NOTES
Report contains color.

14. ABSTRACT

Efforts were conducted to develop nondestructive acoustic and energy-dispersive x-ray spectroscopy techniques for quantitative determination of residual stress and depth-wise residual stress gradients in aerospace materials. Cross-correlation techniques were studied for precise determination of acoustic velocity as a function of frequency. Studies were conducted using eddy-current techniques with GMR sensors to determine their capabilities for detection and monitoring hidden corrosion in multi-layer aerospace structures. Nonlinear acoustic and eddy-current techniques with GMR sensors were used to optimize the retrogression and reaging process in AA7075-T6. Experimental eddy-current data was acquired to aid in development of a model of the eddy-current corrosion-characterization process. ATR-FTIR spectroscopy combined with White Light Interference Microscopy was studied for monitoring corrosion-preventive coatings. X-ray CT was used to monitor 3D corrosion growth. Acoustic emission was studied for its potential for nondestructively monitoring metalworking processes. Small projects were initiated in vehicle health monitoring.

15. SUBJECT TERMS
Ultrasonics, Acoustic Microscopy, Nonlinear Acoustics, Three-element Transducer, X-ray Diffraction, Fretting Fatigue, Residual Stress, Residual Stress Gradient, GMR, Hidden Corrosion Detection, Hidden Corrosion Monitoring, 3D Corrosion Growth, Corrosion Preventive Coatings, X-Ray CT, Vehicle Health Monitoring, Acoustic Emission, Metal Processing, Cross Correlation.

16. SECURITY CLASSIFICATION OF:			17. LIMITATION OF ABSTRACT: SAR	18. NUMBER OF PAGES 122	19a. NAME OF RESPONSIBLE PERSON (Monitor) Claudia Kropas-Hughes
a. REPORT Unclassified	b. ABSTRACT Unclassified	c. THIS PAGE Unclassified			19b. TELEPHONE NUMBER *(Include Area Code)* (937) 255-9795

Standard Form 298 (Rev. 8-98)
Prescribed by ANSI Std. Z39-18

Table of Contents

List of Figures

List of Tables

Foreword

This report describes the technical work accomplished during the period from 30 September 1998 through 31 December 2003 for the AFRL/Materials Directorate, Metals, Ceramics and NDE Division, Nondestructive Evaluation Branch (MLLP) under Contract Number F33615-98-C-5217. The University of Dayton Research Institute (UDRI) was the prime contractor for the effort and the Advanced Research and Applications Corporation (ARACOR) was the major subcontractor in charge of x-ray computed tomography (CT) research and development. Dr. Thomas Moran was the Contract Monitor at the beginning of the contract; Captain Craig Neslon and Dr. Claudia Kropas-Hughes were subsequent contract monitors during the middle and ending phases of the contract.

Mr. Brian Frock of the UDRI Structural Integrity Division was the Principal Investigator from the start of the contractual effort through May 2001; Mr. Robert Andrews, Division Head of the Structural Integrity Division was the Program Manager throughout the entire contract, and was the Principal Investigator from June 2001 until the end of the contract. The following UDRI employees contributed to the accomplishments on this contract: Mr. Thomas Boehlein, Mr. Jeffrey Fox, Mr. Brian Frock, Mr. Edward Klosterman, Dr. Ray Ko, Dr. Victoria Kramb, Mr. Richard Martin, Dr. Theodoras Matikas, Mr. Richard Reibel, Mr. Mark Ruddell and Dr. Shamachary Sathish. UDRI graduate students who contributed to the work were: Dr. James Blackshire, Mr. Adam Cooney, Mr. Christopher Kacmar, and Ms. Sonya Martinez. Mr. Courtney Daniels, Dr. Nicola Dusaussoy, and Mr. Trent Neel of ARACOR contributed to the x-ray CT work effort. Dr. Yellapregada Prasad was a consultant on the contract for acoustic emission research efforts. Ms. Marla McCleskey was responsible for typing and assembling the monthly progress reports. Ms. Andrea Snell was responsible for the work processing this final report.

Section 1
Executive Summary

The goal of this program was to speed the transition of basic nondestructive evaluation (NDE) research results to end-use Air Force applications. To achieve that goal, major projects were conducted in two broad areas of NDE: (1) characterization of fatigue-prevention treatments (compressive residual stress), as well as detection and monitoring of fatigue; and (2) characterization of corrosion-preventive coatings, as well as corrosion detection and monitoring. Smaller projects were conducted in vehicle health monitoring and in metals processing. One special commercial-entity-related program – the Collaborative Technology Clusters (CTeC) program – was conducted in collaboration with AFRL/ML and the State of Ohio's Edison Materials Technology Center. AFRL/MLLP-branch laboratory systems were upgraded, new laboratory equipment was added, and obsolete equipment was removed.

1.0   Results

1.0.1   Residual Stress Measurement and Fatigue-Related Research

- Acoustic surface wave velocity was shown to be capable of distinguishing among areas of differing stress. The results correlate well with x-ray diffraction measurements, but can't yet be used to measure residual stress gradients in aerospace materials.

- The use of mathematical cross-correlation techniques for phase-velocity determination yields precision sufficient for determination of residual stress gradients.

- Energy-dispersive x-ray spectroscopy techniques hold promise for measuring residual stress gradients in aerospace materials; but they are not yet capable of achieving that goal.

- X-ray diffraction techniques have successfully measured stress relaxation in the vicinity of fretting fatigue scars.

- Experimental results support theoretical calculations which show that material fatigue leads to a change in the nonlinear acoustic parameter value of 9 to 12 prior to failure.

1.0.2   Corrosion-Related Research

- GMR sensors can measure eddy-current signals in the frequency range required to inspect thick multi-layered aircraft structures for hidden corrosion.

- The phase output from GMR sensors has been shown to be a potential metric for monitoring local thickness variations caused by hidden corrosion.

- GMR measurements of eddy-current phase lag can be used to optimize the heat-treatment time in the retrogression and reaging (RRA) processing of aerospace aluminum alloys.

- UDRI-acquired experimental data was used to improve an eddy-current modeling procedure developed by Mr. Jeremy Knopp, a civilian employee of AFRL/MLLP.

- Attenuated Total Reflection – Fourier Transform Infrared (ATR-FTIR) spectroscopy combined with White Light Interference Microscopy (WLIM) was shown to be applicable for characterizing corrosion-preventive-coating degradation during weathering exposure.

- The Honeywell Corrosion Environment Monitor (CEM) system was calibrated and data was acquired during flight in a C-141 aircraft. That data was downloaded, stored, and analyzed.

- X-ray CT successfully imaged three-dimensional corrosion growth in an aluminum rod.

- The SAIC Ultra Image IV scanning system with eddy-current and with ACES™ ultrasound was shown to be capable of imaging hidden corrosion in aircraft structures.

1.0.3   Vehicle Health Monitoring

- The self-power generation for in-flight ultrasonic NDE has not progressed to the point at which any definitive conclusions can be reached.

- Rayleigh surface wave velocity was shown to be capable of indicating characteristics of bending similar to that which might occur in turbine engine blades.

1.0.4   Monitoring Metal Processes

- Acoustic emission was shown to have a very high potential for nondestructively monitoring metalworking processes.

Section 2
Introduction

This program was established to speed the transition of basic research results to end-use Air Force applications. It was specifically designed to serve as a bridge between: (1) the basic 6.1 research output from both the in-house research group in AFRL/ML and other Air Force and DoD-sponsored basic research, and (2) the exploratory and advanced development (6.2 and 6.3 program elements) contractual programs.

The Air Force decision to extend the use of many of its aircraft to times that are well beyond the design lives steered the program efforts into two major nondestructive materials-characterization research areas that, if successful, could significantly improve the reliability of remaining-life predictions. These areas are: (1) characterization for fatigue-damage prevention, detection and monitoring; and (2) characterization for corrosion prevention, detection and monitoring.

By contractual agreement, the program was organized into two major tasks as shown in Table 2.1-1. However, because of the nature of the research endeavors during the contractual period, this report will be divided into sections that describe the NDE efforts in: (1) fatigue-related materials characterization; (2) corrosion-related materials characterization; (3) vehicle health monitoring; (4) special projects; and (5) systems upgrades, maintenance and repair. The directions of some of the efforts in these areas are briefly described in the following paragraphs.

Table 2.1-1 – Two-Task Technical Program Organization

Task I – Technique Advantages and Limitations Assessment
• Investigate reliability and accuracy of measurement and/or data analyses methods for ability to nondestructively and quantitatively characterize properties of materials.
• Place particular emphasis on techniques for characterizing properties of coatings, thin films, and materials undergoing high cycle fatigue, and for detecting and characterizing corrosion.
• Identify and quantify the degrading effects of physical inspection situations (geometry, etc.).
• Upgrade laboratory systems and software.
Task II – Application Feasibility Assessment
• Select most likely application areas for techniques from Task I by consulting with Air Force personnel, making fact-finding trips to Air Logistics centers, and attending technical conferences.
• Determine applicability of each Task I technique to the selected application area by considering technique sensitivity, reliability, cost effectiveness and capabilities relative to existing techniques.

2.0   NDE Research for Fatigue-Related Characterization of Materials

Most of the NDE effort for characterization of fatigue-damage prevention, detection, and monitoring was directed toward materials that are used in rotating parts of gas turbine engines. The driving force for this direction was the Air Force's Engine Rotor Life Extension (ERLE) Program. Ultrasonic surface wave and x-ray diffraction techniques were explored for their capabilities and limitations in measuring the surface residual stress and depth-wise residual stress gradients that are deliberately introduced into materials to prevent fatigue-crack initiation and growth. X-ray diffraction techniques were examined for their abilities to detect and monitor fatigue damage. X-ray diffraction techniques were also used to study the changes in stress states that occur during fretting fatigue and how those stress-state changes affect damage initiation and progression. A small study was conducted to determine the capabilities and limitations of using energy-dispersive x-ray spectroscopy for measurement of residual stress gradient in aerospace materials.

2.1   NDE Research for Corrosion-Related Materials Characterization

Studies in this area were concentrated in assessing the capabilities and limitations of NDE methods for detecting and quantifying corrosion in multi-layer airframe structures and in assessing the capabilities and limitations of specific NDE methods for characterization of corrosion-prevention coatings. New eddy-current techniques and devices were studied for the nondestructive detection and characterization of corrosion in multi-layer structures. In particular, the capabilities and limitations of the relatively-new giant magnitoresistive (GMR) transducers were investigated for detection and characterization of corrosion. Nondestructive coatings research was focused toward the changes in physical and chemical states of corrosion-prevention coatings that occur as a result of weathering.

A small, but significant, fundamental study was initiated to study the three-dimensional growth aspects of corrosion in aluminum. Most previous efforts have only emphasized the two-dimensional growth of corrosion. Both high-resolution x-ray diffraction and ultrasonic techniques were used for this effort.

A study to determine the feasibility of using SAIC's Ultra Image IV system for automated detection of corrosion in aircraft structures was funded through this contractual effort, but was conducted offsite by SAIC personnel. Another study was conducted (onsite in AFRL/MLLP) to

determine the capabilities and limitations of using a Honeywell-developed system to monitor the corrosion environment in the wheel well of an operational C-141 aircraft.

A University of Dayton graduate student, Mr. Chris Kacmar, conducted experimental studies in collaboration with Dr. James Blackshire, a civilian employee in AFRL/MLLP, to provide information about fatigue cracks that originated from a variety of sources. Sources studied were corrosion damage, notch damage, treatment damage, and supposedly-undamaged aluminum and titanium specimens.

2.2   Vehicle Health Monitoring

Two vehicle-health-monitoring-related projects were conducted during the course of this project. The one, "Self-Power Generation for In-Flight Ultrasonic NDE" was focused on developing a system that would generate power from in-flight aircraft structural vibrations. The power would then be used to transmit, receive, and store ultrasonic data related to the detection of fatigue cracks and the monitoring of subsequent growth of such cracks.

The second project, "Sensing Technology for *In Situ* Health Monitoring of Gas Turbine Engine Blades Feasibility Study", was directed toward determining the feasibility of using surface acoustic waves (SAW) for monitoring the vibration modes and frequencies experienced by blades on rotating engine components. Changes in the vibration modes and frequencies during operation could provide information about material properties changes that might presage in-service failure.

2.3   Special Projects

The so-called "special projects" included a wide variety of smaller, but important, efforts that were conducted during the contractual period. Among these were the following:

- A theoretical study of the "Feasibility of Using Acoustic Emission Techniques for Monitoring Metal Processing" by Dr. Yellapregada Prasad, a world expert in that specialty from India;
- An experimental data-gathering effort for "Eddy-Current Characterization of Cracks Around Fasteners in Multi-Layer Structures" that was conducted in collaboration with Dr. Claudia Kropas-Hughes and Mr. Larry Dukate, civilian employees in AFRL/MLLP;
- "Characterizing Particulate-Matter Distribution in Metal-Matrix Composites" via x-ray CT;
- Several studies initiated through the Collaborative Technology Clusters (CTeC) program; and
- A variety of small service-type projects.

2.4   System Upgrades, Maintenance and Repair

Many of the systems that existed at the start of this contract were upgraded and/or repaired during the period-of-performance. The major upgrades and repairs are listed in Section 7, titled "Systems Upgrades, Maintenance and Repair".

Section 3
Residual Stress Measurement Research

3.0   Introduction

3.0.1   Air Force Need

Many aircraft structures – especially turbine-engine components – are shot peened or laser-shock peened after fabrication. Such surface treatments induce a compressive residual stress that is parallel to the surface, thereby inhibiting the initiation and growth of cracks during cyclic fatigue and increasing the service life of the treated component. The residual stress varies with depth, increasing for a few microns and then decreasing. The depth of the compressive residual stress varies from 10 to 500 μm depending on the material, peening intensity, and density of coverage.

The current predictive service-life models do not take full credit for the beneficial effects of compressive residual stress. This non-inclusion results in predicted service lives that are most likely considerably less than actual service lives, leading to premature component replacements and increased maintenance costs. Uncertainty as to the continued existence of such stresses after subjecting the component to service, and a lack of a suitable NDE technique for measuring the stress and stress gradients, are often cited as reasons for non-inclusion in service-life-prediction models. Development of an NDE method for measuring residual stresses in components before and after service would allow for significant savings through improvements in life prediction models and, thus, longer component useful life.

3.0.2   Potential Solutions

Ultrasonic

Ultrasonic methods can be used to measure stress because the stress state in a material is directly related to the acousto-elastic constants which are, in turn, directly related to the velocity of sound in the material [1]. Thus, the velocity of surface waves, such as Rayleigh surface waves (RSWs), surface-skimming longitudinal waves (SSLWs), and surface-skimming shear waves (SSSW), can provide surface and near-surface residual stress information. RSWs are advantageous for measuring the stress gradients because

the penetration depth of an RSW is approximately equal to its wavelength. Depth-wise residual stress gradients cause the RSW velocity to vary as a function of wavelength (frequency); this frequency-dependent velocity variation (velocity dispersion) should be usable for the measurement of the depth-wise stress gradient. Thus, UDRI initiated a program to determine the feasibility of calculating depth-wise residual stress gradients from measurements of the velocity dispersion curve (velocity versus frequency) of Rayleigh surface waves. However, the anticipated change in velocity as a function of frequency in depth-wise stress gradients is on the order of 1% or less, and achieving this precision in ultrasonic velocity measurements is not an easy task. Therefore, much of the effort to date has been concentrated in determining and improving the precision in measurements of RSW velocity dispersion.

Energy-Dispersive X-Ray Spectroscopy

The measurement of residual stress as a function of depth by x-ray techniques is limited by practical considerations, e.g., counting time. The basic limits on penetration depth, set by background and peak overlap, imply that the required energies are high relative to standard diffraction sources. However, ARACOR conducted a series of tests in their California laboratories that demonstrated that shifts in diffraction peaks due to material stress could be measured using energy-dispersive spectroscopy. Therefore, ARACOR extended those studies for measurement of residual stress as a function of depth in Aerospace materials.

X-Ray Diffraction

Very little is currently understood about the behavior of surface residual stress under fretting-conditions. However, fretting fatigue is of considerable importance to the Air Force because it can result in catastrophic failures in aerospace components. Therefore, UDRI initiated a program to determine the feasibility of using well-established x-ray diffraction techniques for gaining an understanding of the behavior of residual stress under fretting-fatigue conditions.

3.1   Two-Point Defocus Method for Practical Quantitative Acoustic Imaging of Near-Surface Material Stress

3.1.1   Air Force Need

As explained in the introductory segments of this section, compressive residual stresses are intentionally introduced into many aircraft structures to inhibit the initiation and growth of cracks in critical components. However, no current methodology exists for the rapid nondestructive quantitative measurement of such stresses. Thus, the stress states of the components remain largely unknown.

3.1.2   Classical Acoustic Microscopy Technique for Estimating Elastic Properties

One of the classic methods for measuring local elastic properties is through V(Z) curve analysis. In this method, the distance between the lens and sample is varied and the amplitude of the acoustic signal returning to the transducer is measured. Due to the presence of a mode-converted surface acoustic wave (SAW), the amplitude undergoes periodic oscillations. The velocity of the SAW can be calculated from the periodicity of the amplitude oscillations; that calculated velocity can then be used to estimate the value of the elastic constants from which the surface residual stress can be determined. This methodology has been used for measurement of local elastic properties of many different materials [2,3]. Although the method is powerful, it is very slow and, therefore, is not practical for scanning aircraft components. Extending the method to obtain a quantitative map is prohibitively time-consuming. Thus, acoustic microscopy has mostly been used to provide a qualitative image, or to measure local elastic properties at a few discrete locations.

3.1.3   Two-Point Defocus Technique for Scanning Quantitative Imaging of Elastic Properties

The goal of this project was to develop a relatively rapid nondestructive scanning acoustic microscopy methodology for generating quantitative images of the local elastic properties from which local residual stress values could be determined. For this purpose, the High Precision Scanning Acoustic Microscope was used with a commercial acoustic lens operating at a frequency of 50 MHz. The principle of the methodology is shown in Figure 3.1.3-1. A sharp electrical impulse excitation is used to excite the transducer. The acoustic waves that are generated converge to focus on the surface of the sample. When

the lens is defocused, SAWs are generated. The transducer receives two different signals. The first signal is a signal that is directly reflected from the sample surface. The SAWs propagating at the interface between water and the sample arrive at a later time. The two signals can be separated and the time difference can be measured. The SAW velocity can be determined from the time difference between the two signals at two different defocus distances, Z1 and Z2, (see Figure 3.1.3-2). The SAW velocity can be calculated using the following formula:

$$V_{saw} = \frac{2(Z_1 - Z_2)}{\sqrt{\left[(\Delta t_1 - \Delta t_2)^2 - (\Delta t_{saw1} - \Delta t_{saw2})^2\right]}} \qquad (1)$$

Z_1 and Z_2 are the two defocuses. Δt_1 and Δt_2 are the times measured from a reference position to the direct-reflected signal at two defocuses. Δt_{saw1} and Δt_{saw2} are the time from the same reference to the SAW signal at the two defocuses (Figure 3.1.3-2). This is the time difference method of SAW velocity measurement.
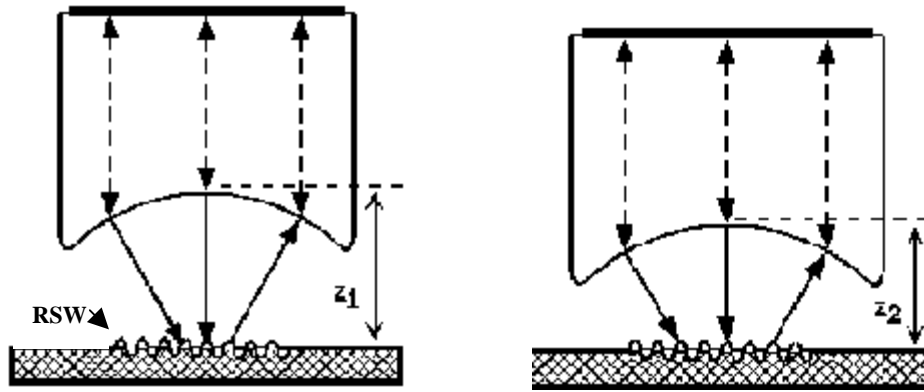
Figure 3.1.3-1. Transducer defocused 0.4 mm at Z1 (left) and 1.0 mm at Z2 (right).
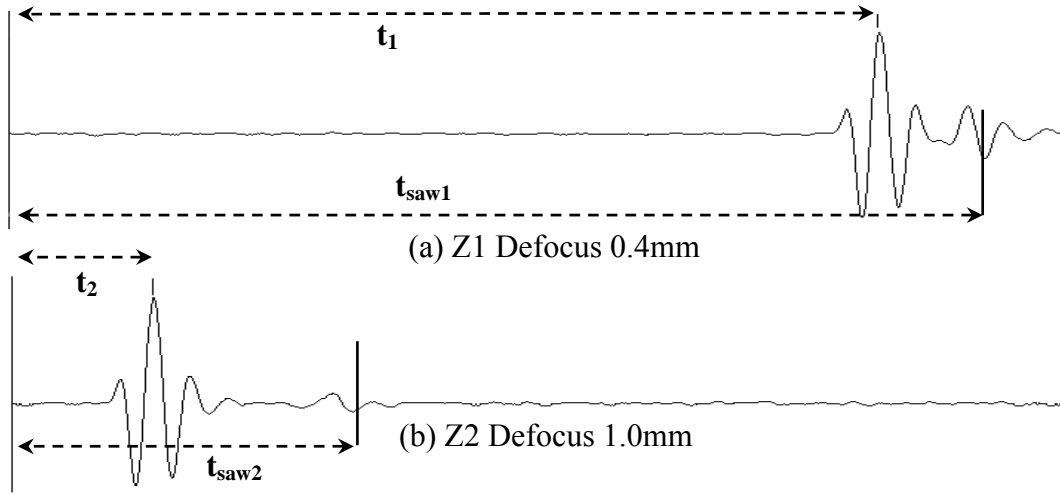
Figure 3.1.3-2. Waveforms of the direct-reflected and SAW signals at two different defocus positions.

In practice, the arrival times (Δt_1 and Δt_{saw1}) at defocus positions Z1 and Z2 are calculated and the velocity is determined from equation 1. Then, the arrival-time measurements and velocity calculations are repeated several times at the two defocus positions and the results are averaged to provide a single velocity value at the data-acquisition point. The acoustic lens is moved to a new position and the measurements are repeated. The entire procedure is repeated at periodic locations on the sample to generate an image of SAW velocities (or elastic properties).

3.1.4   Verification

The two-point defocus technique was verified by applying it to the measurement of the SAWs on a disk-shaped E-6 glass specimen. The results were in very good agreement with results obtained via more standard SAW velocity measurements.

During these verification measurements, it was discovered that it was possible to observe the Surface Skimming Longitudinal Wave (SSLW) and the Surface Skimming Shear Wave (SSSW), and to measure their velocities with the two-point defocus technique [4,5]. The accuracy and the precision of the SSLW and the SSSW velocity measurements made via the two-point defocus technique were compared with velocity measurements of the same waves using other techniques. The results were found to be in good agreement.

3.1.5   Applications

Imaging Microstructure of Large-Grain-Size Ti-6Al-4V

The two-point defocus technique was used to image the microstructure of large-grain-size Ti-6Al-4V. The Rayleigh SAW velocity was measured and mapped over a 15 mm × 15 mm area of the sample. The amplitude of the Rayleigh SAW was also used to generate a C-scan map of the sample's surface. The amplitude and the velocity images are provided in Figure 3.1.5-1.

(a)   (b)
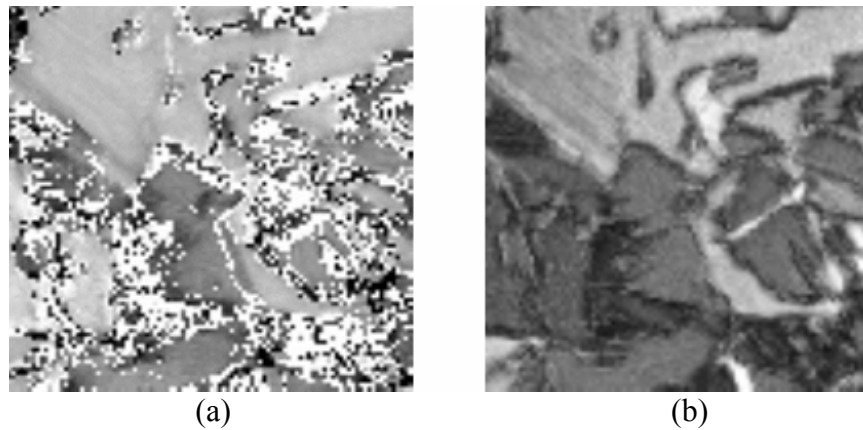
Figure 3.1.5-1. Rayleigh-surface-wave images of large grains in a Ti-6Al-4V material: (a) velocity and (b) amplitude.

Imaging Stress Distribution Near a Crack Tip

The two-point defocus technique was also applied to image the SAW velocity distribution around a crack tip in a Ti-6Al-4V specimen. The velocity varies proportionally with stress; thus, such velocity images are essentially images of the distribution of surface stress. It is well known that Rayleigh SAWs penetrate to a depth of approximately 70 to 170 μm at 50 MHz, whereas, surface-skimming longitudinal waves (SSLWs) only penetrate to a depth of 20 to 25 μm at the same frequency. It is also well known from fracture mechanics calculations and experiments that the stress distribution around a crack is three-dimensional, and that significant variations in stress as a function of depth can be expected in the vicinity of a crack. Thus, SSLWs were used to image the near-surface stress (velocity) distribution in the vicinity of the crack in the Ti-6Al-4V sample. The results are shown in Figure 3.1.5-2a.

12

X-ray diffraction measurements of very-near surface stress were also made at a large number of locations near the same crack tip and an image was constructed from these measurements. The images constructed from these x-ray diffraction measurements are provided in Figure 3.1.5-2b. The visual similarity of the image constructed from the SSLW measurements and the image constructed from the x-ray diffraction measurements is striking.
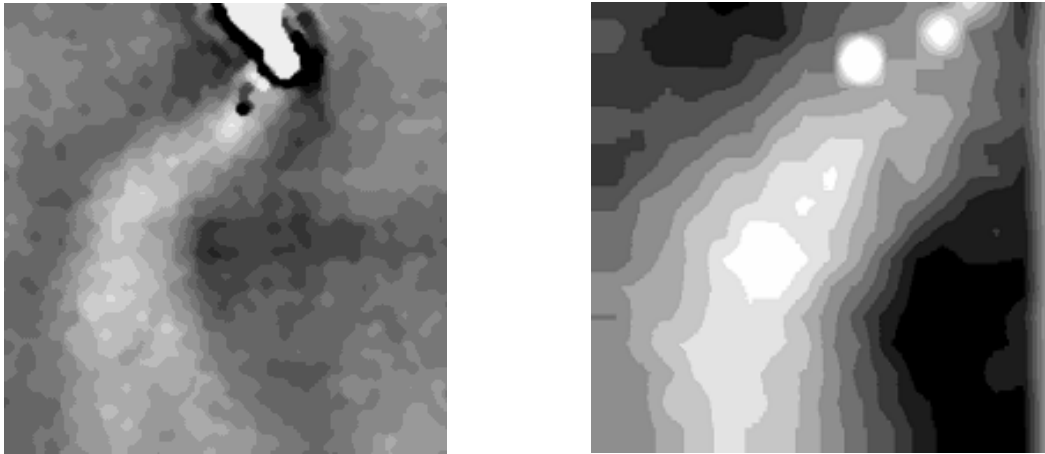
Figure 3.1.5-2. Images of stress around a crack tip in Ti-6Al-4V: (a) SSLW velocity measurements of stress and (b) x-ray diffraction measurements of stress.

3.1.6   For Additional Information

Additional information about this two-point defocus acoustic microscopy technique can be found in Appendix A. Please see the papers titled: "Quantitative Imaging of Rayleigh Wave Velocity with a Scanning Acoustic Microscope", "Development of a Scan System for Rayleigh, Shear, and Longitudinal Wave Velocity Mapping", "Scanning Acoustic Microscopy and X-Ray Diffraction Investigation of Near Crack Tip Stresses", "Local Surface Skimming Longitudinal Wave Velocity and Residual Stress Mapping" and "Rayleigh Wave Velocity Mapping Using Scanning Acoustic Microscope".

3.2   Residual Stress Gradient Measurements by Ultrasonic Techniques

3.2.1   Air Force Need

The compressive residual stress that is induced by shot peening varies as a function of depth. The compressive stress first increases with depth and then gradually decreases to zero, after which there is a compensatory tensile stress that eventually falls to zero. A generalized profile of the residual stress gradient as a function of depth in a

material is shown in Figure 3.2.1-1. Air Force engineers need a nondestructive technique for measuring that profile so that they can accurately estimate the remaining fatigue life of specific components. Thus, UDRI initiated a project to develop a nondestructive technique for measuring the residual stress gradient as a function of depth in aerospace materials.
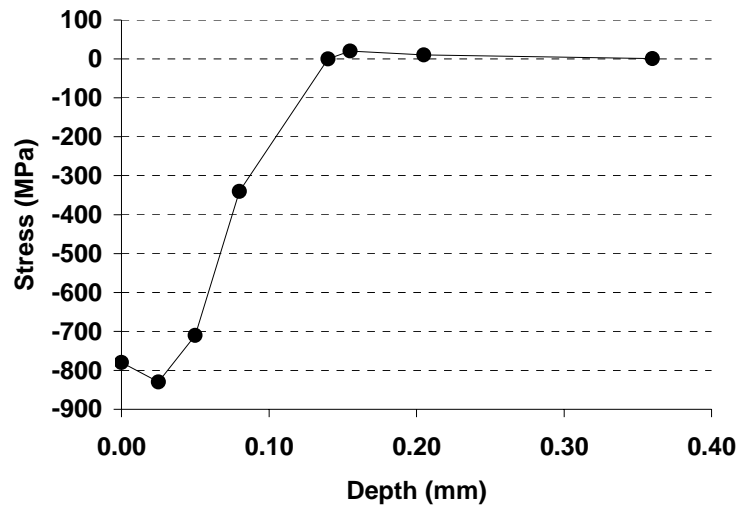
Figure 3.2.1-1. Typical stress versus depth curve for shot-peened titanium-alloy specimen.

3.2.2   Potential Technique for Measuring Depth-Wise Residual Stress Gradients

The velocity of a Rayleigh surface wave (RSW) is stress dependent, and the penetration depth of an RSW increases as the frequency of the RSW decreases. Therefore, measurement of RSW velocities at different frequencies should provide an estimate of the change in residual stress as a function of depth. However, there are some stringent requirements for the successful quantitative measurement of residual stress as a function of depth by use of RSW velocity measurements. These requirements are:

1. A well-established, precise, and accurate method for independently measuring the residual stress must be available;

2. A mechanism for introducing different levels of compressive and tensile stress into a material is required;

3. Very high precision measurements of RSW velocity as a function of frequency (velocity dispersion); and,

4. A model to convert the RSW velocity dispersion into a depth-dependent residual stress gradient.

UDRI has concentrated on the first three of these requirements, the first two of which constitute a method for independently calibrating the acoustic technique.

3.2.3   An Independent Calibration Technique

X-ray diffraction was chosen as the well-established, precise, and accurate technique for independently measuring the stress induced into a material. A four-point bending device (Figure 3.2.3-1) was designed and fabricated for introducing different levels of stress into a material sample. Both the upper and lower plates have rectangular cutouts to allow access by the x-ray beam. The screws at either end of the plates are tightened to cause bending that induces tensile stresses on one side and compressive stresses on the other. X-ray diffraction and two-point defocus acoustic microscopy measurements of RSW velocity were made on both sides of a Ti-6Al-4V sample at several different stress levels. The results are shown in Figure 3.2.3-2. That figure clearly indicates that the RSW velocity decreased as the compressive stress decreased. Unfortunately, the velocity measurements at low stress levels are difficult and require more precision than could be obtained with the current two-point defocus technique.

Side view

Top view

Opening for X-Ray and Acoustic Measurements
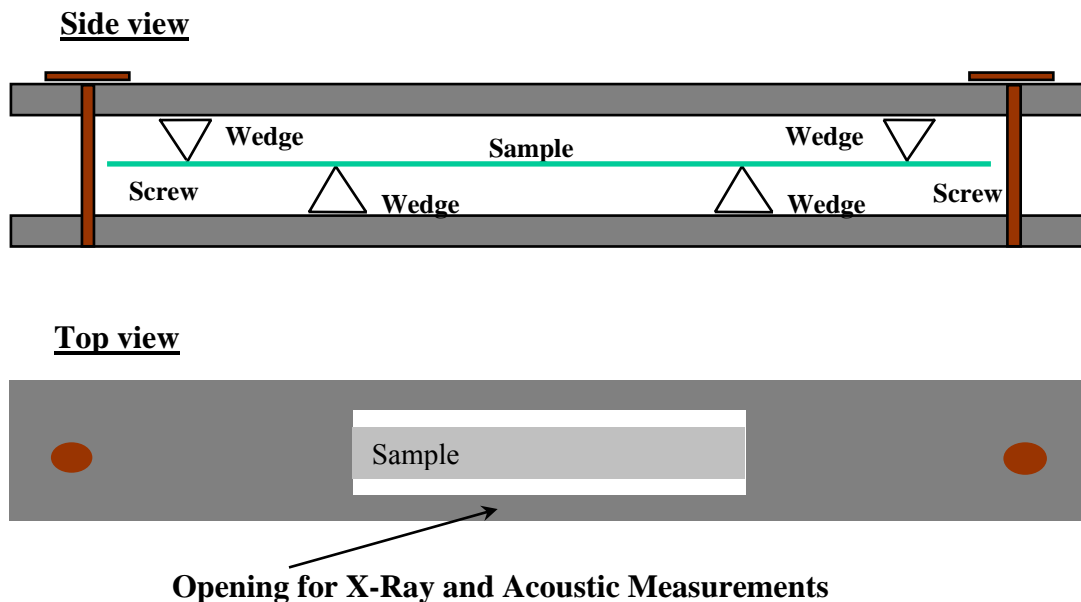
Figure 3.2.3-1. Four-point-bending apparatus for introducing different levels of compressive and tensile stress into material specimens for calibration measurements.

15
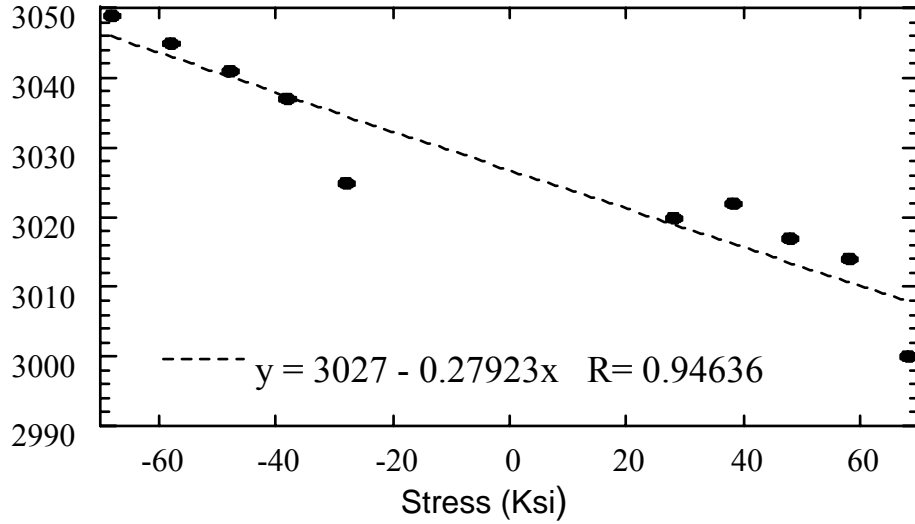
Figure 3.2.3-2. Rayleigh surface wave velocity as a function of stress in Ti-6Al-4V.

3.2.4   Three-Element Transducer for High-Precision RSW-Velocity Measurements

A new focused acoustic transducer (lens) was designed (Figure 3.3.3-3) to improve the precision of the velocity measurements. That lens consists of three separate elements that have a common focus. The central element generates a longitudinal acoustic wave that impinges on the material surface at normal incidence. When the lens is defocused toward the surface, one of the two lower elements excites an RSW on the surface of the sample. The other transducer detects the RSW that leaks back into the water. During measurements, a tone burst signal is used to excite the central element and one of the lower elements. The central element detects the directly-reflected signal and one of the lower elements detects the RSW. The phase difference between the directly-reflected signal and the RSW signal is measured. That phase difference ($\Delta\varphi_{L-R}$) is related to the Rayleigh wave velocity through equation 2,

$$\Delta\varphi_{L-R} = (4\pi F \tan\theta_R/V_R) (\Delta V_R/V_R) \Delta z \qquad (2)$$

In equation 2, F is the acoustic frequency, V_R is the Rayleigh wave velocity in the material, ΔV_R is the change in the Rayleigh wave velocity, θ_R is the Rayleigh wave critical angle, and Δz is the defocus distance. The smallest velocity change that can be measured using the phase measurement approach is about 1 part in 10^6.

16
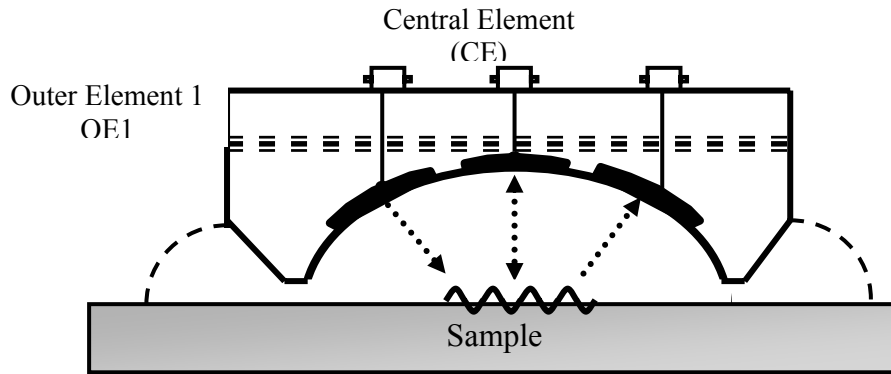
Figure 3.2.4-1. Three-element acoustic microscope transducer.

Two methods were developed to measure the phase difference. In the first method, the directly-reflected, normal-incidence acoustic signal and the received RSW signal were amplified and input to a mixer. The output of the mixer is a combination of two signals; the frequency of the first signal is the sum of the frequencies of the two input signals, and the frequency of the second signal is the difference of the two signals. Since the frequencies of the input signals are identical, the frequency of the second signal is zero, i.e., it is a DC level. The sum-frequency component was filtered out and the amplitude of remaining signal (a DC component that was directly proportional to the phase difference) was measured. In the second method, the two signals were fed into a lock-in amplifier and the phase difference was measured directly by that instrument.

The applicability of the lens and instrumentation was first tested by measuring the change in the RSW velocity across an electron beam weld line in a Ti-6Al-4V specimen. The weld specimen is depicted in Figure 3.2.4-2a. A velocity image map of the weld specimen using the three-element lens is shown in Figure 3.2.4-2b. Both of the phase-measurement methods were used with the three-element transducer to generate a phase-change profile across weld in the specimen. A stress profile across the specimen was also measured directly with an X-ray diffraction system (XRD). The results of the acoustic-wave phase-difference measurements and the X-ray diffraction measurement are shown in Figure 3.2.4-3. The results clearly show that the RSW velocity is higher (darker color) in the region of compressive residual stress around the weld, while in the region of tensile stress, it is lower (lighter color). The measurement techniques can detect phase changes caused by residual stress variations of the order of 1-2 MPa. This sensitivity is at least an order of magnitude improvement over the earlier two-point defocus method.
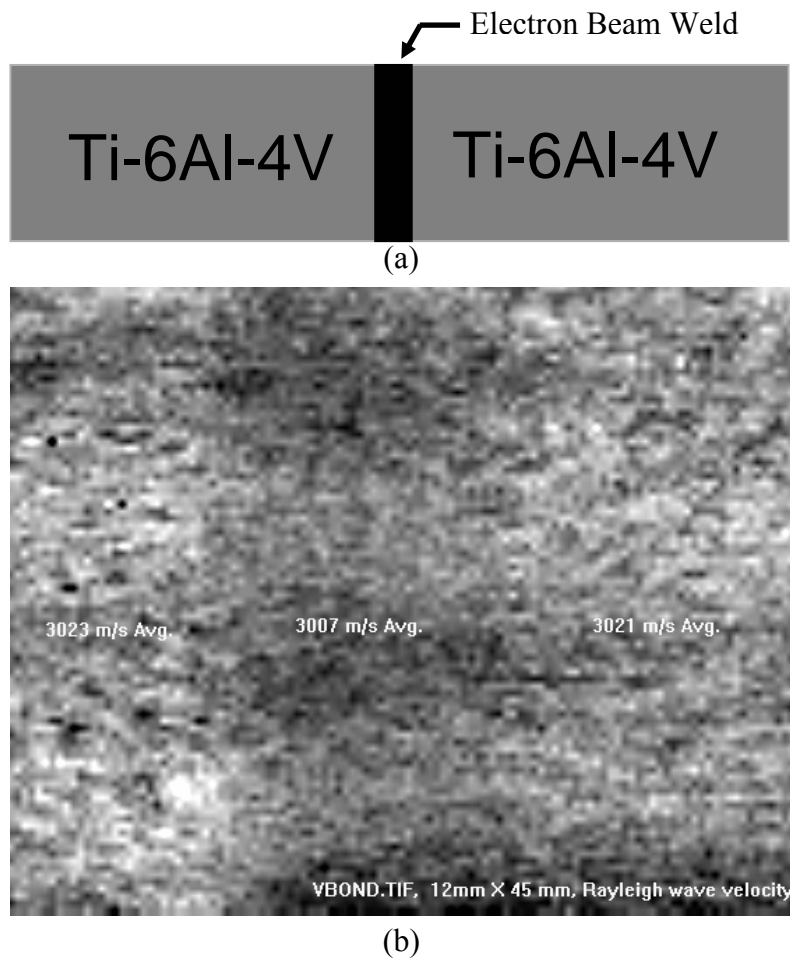
Figure 3.2.4-2. E-beam welded Ti-6Al-4V specimen: (a) sketch of the specimen and (b) velocity map across the weld line using the two-point defocus method.
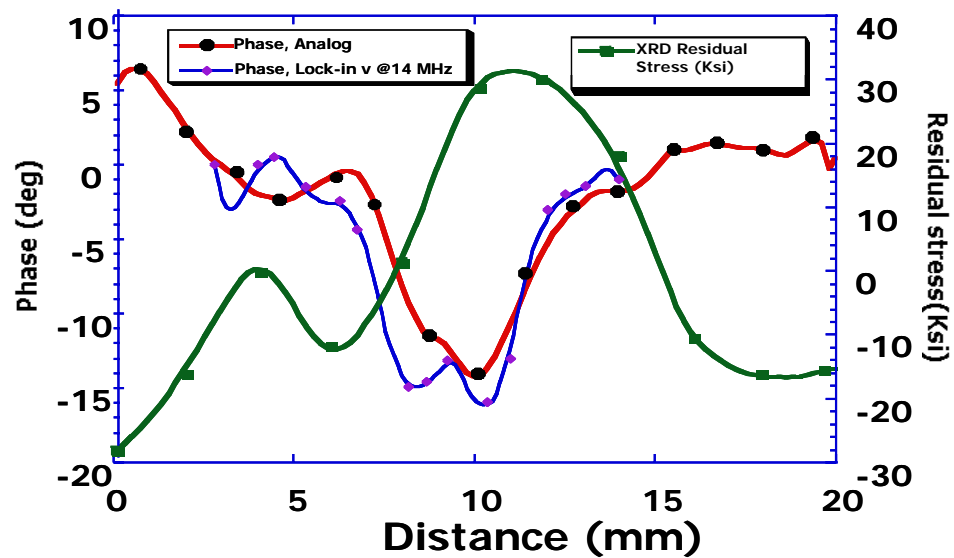
Figure 3.2.4-3. Variation of phase-difference measurements and x-ray diffraction residual stress measurements across a weld line in Ti-6Al-4V.

The relatively wide-band (10 to 25 MHz), three-element, focused acoustic transducer has been found to be very sensitive to small variations in residual stress. Thus, the quantitative measurements of RSW dispersion in surface-treated aerospace materials should be possible with this three-element transducer. UDRI has made RSW velocity measurements on shot peened material and also on low-plasticity-burnished samples of Ti-6Al-4V. The results are shown in Figures 3.2.4-4 and 3.2.4-5, respectively. The plots in those figures demonstrate that RSW velocity dispersion is present in both samples. The dispersion is independent of the direction of measurement in the case of the shot peened sample, while on the low-plasticity-burnished specimen, the RSW dispersion is dependent on the direction of measurement.
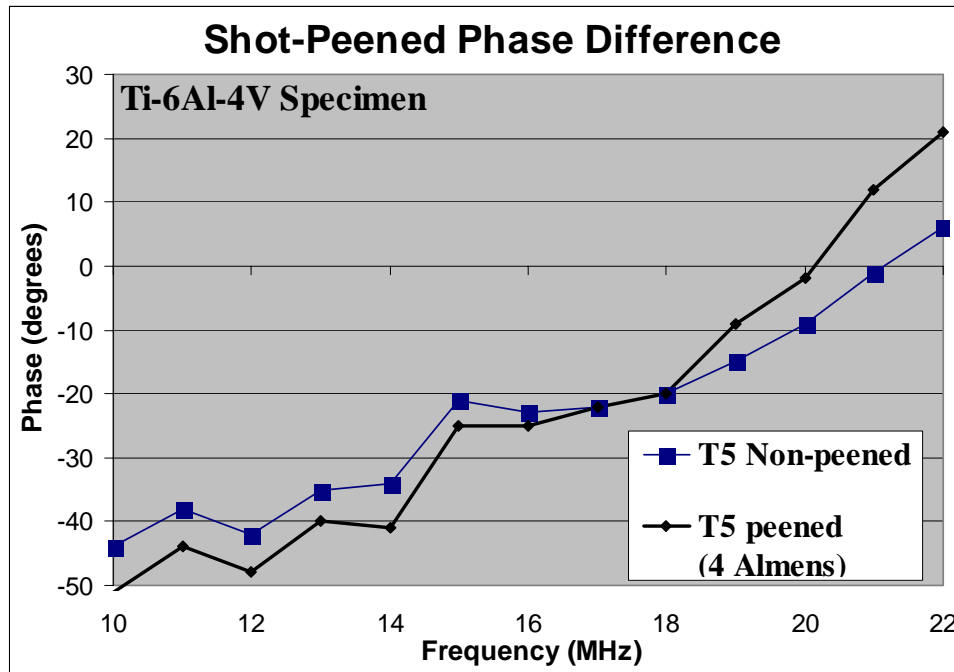
Figure 3.2.4-4. Phase difference data on peened and non-peened Ti-6Al-4V.

LPB Phase Difference
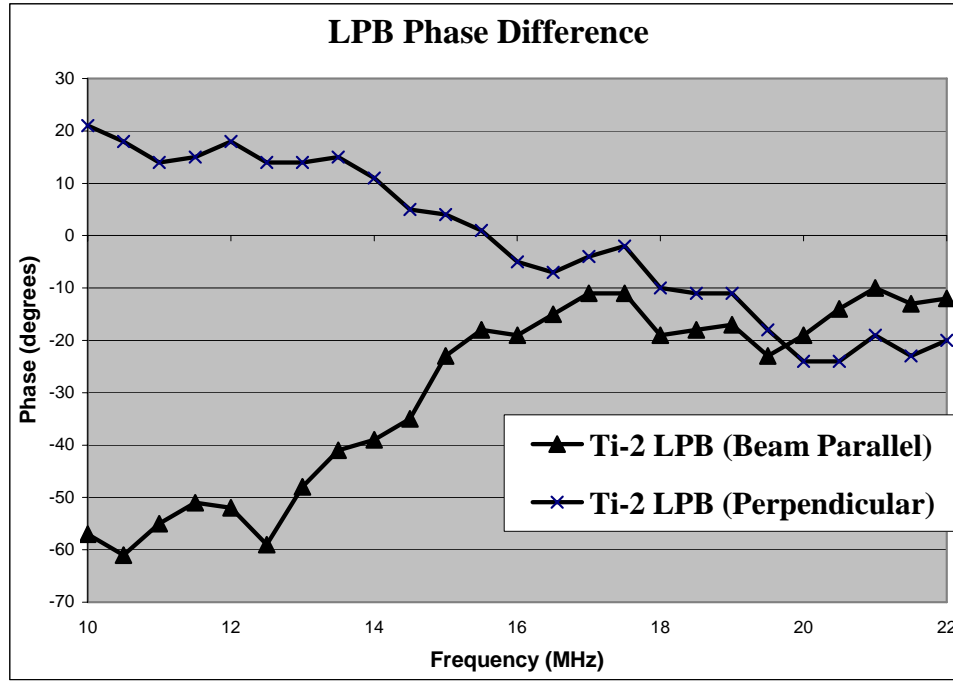
Figure 3.2.4-5. Rayleigh surface wave phase-difference measurements on LPB material.

3.2.5 For Additional Information

Additional information about this topic can be found in the articles titled: "Local Phase Measurements with focused Acoustic Transducer" and "Acoustic Interferometer for Localized Rayleigh Wave Velocity Measurements". These articles are included in Appendix A.

3.3   Mathematical Calculation of Velocity Dispersion from Ultrasonic Data

3.3.1 Basic Technique

This effort was undertaken to determine the precision to which the difference in the phase velocity of individual frequency components of an RSW wave could be calculated in the case for which no velocity dispersion existed. The phase velocity difference between individual frequency components of an RSW signal can be calculated directly from the Fourier-phase spectrum (cross-spectrum) of a reference signal (initial transmitted pulse) that is cross-correlated with a received RSW signal [6,7]. In fact, the relationship between phase difference and the arrival time difference as a function of frequency is given by [6] equation 3.

$$\Delta\Phi_f = 2\pi f \Delta t_f \qquad\qquad (3)$$

In that equation, $\Delta\Phi_f$ is the phase difference for the component at frequency, f, and Δt_f is the arrival time difference for the component at frequency, f. If there is no velocity dispersion, "$\Delta\Phi_f/(2\pi f) = \Delta t_f$" will be constant for all f, i.e., the relationship between $\Delta\Phi_f$ and f will be linear. If, however, the velocity is dispersive, the relationship between $\Delta\Phi_f$ and f will be nonlinear. It is this departure from linearity that must be precisely calculated to quantify the dispersion relationship and, from that dispersion relationship, the residual stress as a function of depth can be inferred. Thus, the first step in this mathematical process was to determine the precision to which the relationship defined by equation 3 could be determined for nondispersive RSW propagation.

3.3.2 Procedure

A single digitized broadband ultrasonic pulse was used as the reference signal and was used also to simulate the signals of interest (time-delayed signals). The signal data was acquired with an 8-bit digitizer operating at a rate of 1 giga-sample per second using an acquisition-window-length of 2048 points (2.047 micro-seconds). The digitized signal and its Fourier magnitude spectrum are shown in Figure 3.3.2-1. As shown in Figure 3.3.2-1b, the peak in the Fourier magnitude spectrum occurred at approximately 20 MHz. Thus, the sampling rate was approximately 25 times the Nyquist criterion for the frequency at which the maximum magnitude occurred.

Since the intent of this study was to examine the precision of the time-delay estimates derived from application of the cross-correlation technique, it was important to eliminate extraneous factors such as noise and differences in frequency content between the reference and the time-delayed signal. Deriving the time-delayed signal from the digitized reference signal eliminated those extraneous factors. The derivation procedure is outlined in the diagram in Figure 3.3.2-2.

3.3.3 Results

The differences between time delays calculated from the linear phase-slope relationship and the actual time delays are presented in tabular form in Table 3.3.3-1. The calculated time delays did not deviate from the actual time delays by more than 0.4% in any of the cases studied. In fact, most of the calculated time delays were within less than 0.2% of the actual time delays. The original intent of this effort was, however, to calcu-

late a statistical measure of the precision to which the time delay (phase difference) could be estimated for nondispersive wave propagation. As demonstrated in Figure 3.3.3-1a, the relationship between phase (unwrapped) and frequency is linear for nondispersive wave propagation. But, as Figure 3.3.3-1b clearly shows, the residuals from the linear fit are autocorrelated, i.e., there is a significant non-random pattern. Thus, no statistical statement as to the precision of the estimate of arrival times (phase difference) could be established. These results have not been published.
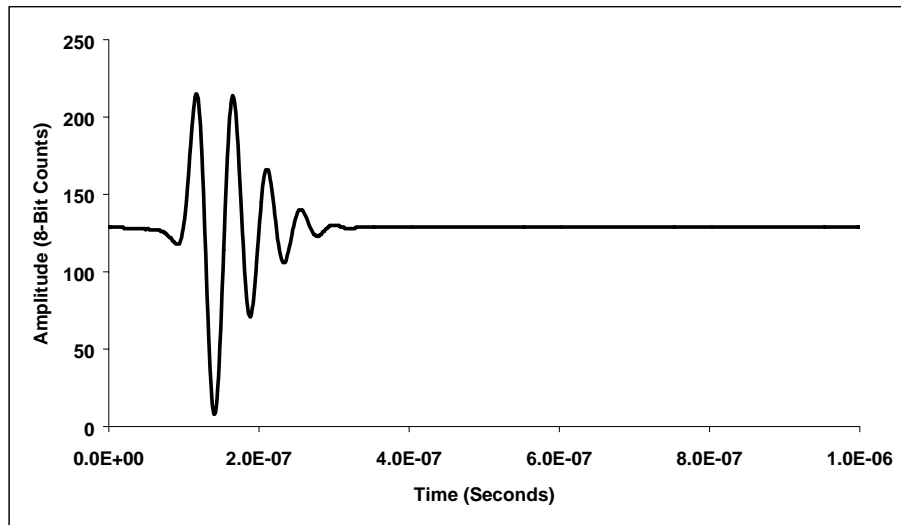
(a)
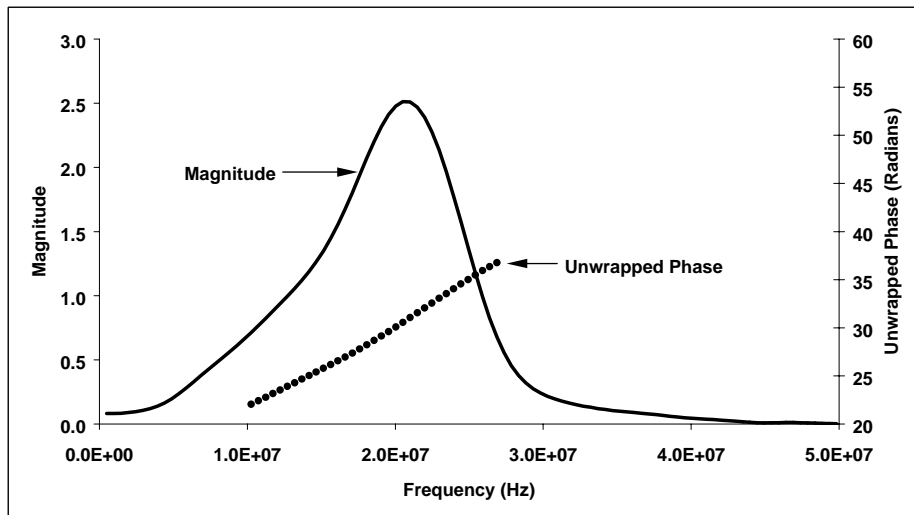
(b)

Figure 3.3.2-1. Reference signal: (a) time domain and (b) Fourier Domain

22
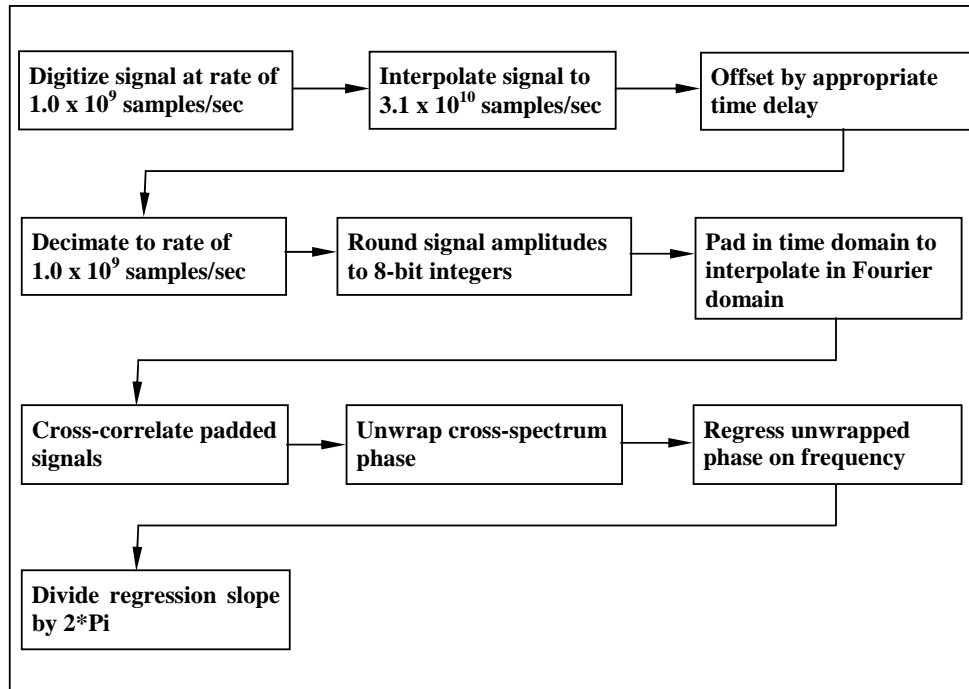
Figure 3.3.2-2. Flow chart of simulation procedure

Table 3.3.3-1. Difference Between Phase-Slope Estimate of Time Delay and Actual Time Delay

Interp Factor	Column Headings Are Actual Time Delays in Seconds					
	5.0968E-09	5.1290E-09	5.4839E-09	5.5161E-09	5.9032E-09	5.8710E-09
1	-9.5287E-12	-3.1631E-12	1.5958E-12	1.8145E-11	5.7167E-12	3.8611E-12
2	-8.9903E-12	-2.8970E-12	3.1602E-12	2.0657E-11	8.1681E-12	6.0942E-12
3	-8.7691E-12	-2.7781E-12	3.6781E-12	2.1505E-11	8.9555E-12	6.7965E-12
4	-6.2800E-12	-2.5916E-13	4.2961E-12	2.1059E-11	6.8905E-12	4.7178E-12
5	-6.7045E-12	-7.3186E-13	4.3628E-12	2.1493E-11	7.6337E-12	5.4291E-12
6	-6.9798E-12	-1.0400E-12	4.4118E-12	2.1782E-11	8.1225E-12	5.8958E-12
7	-5.8194E-12	1.4424E-13	4.6601E-12	2.1988E-11	8.4684E-12	6.2254E-12
8	-6.1403E-12	-2.0006E-13	4.6559E-12	2.1707E-11	7.5093E-12	6.0775E-12
9	-6.3869E-12	-4.6506E-13	4.6546E-12	2.1876E-11	8.4721E-12	6.3245E-12
10	-5.6354E-12	3.0484E-13	4.8043E-12	2.2012E-11	8.6844E-12	6.5189E-12
11	-5.8849E-12	4.0442E-14	4.6117E-12	2.1674E-11	7.9598E-12	5.7901E-12
12	-6.0912E-12	-1.7846E-13	4.6146E-12	2.1803E-11	8.1805E-12	5.9976E-12
13	-5.7392E-12	-3.6266E-13	4.6177E-12	2.1913E-11	8.3659E-12	6.1715E-12
14	-5.7392E-12	1.7744E-13	4.7273E-12	2.2006E-11	8.5237E-12	6.3194E-12
15	-5.9139E-12	-6.7581E-15	4.7215E-12	2.1854E-11	8.0059E-12	5.8010E-12
16	-6.0661E-12	-5.2556E-13	4.7169E-12	2.1940E-11	8.1672E-12	6.3606E-12
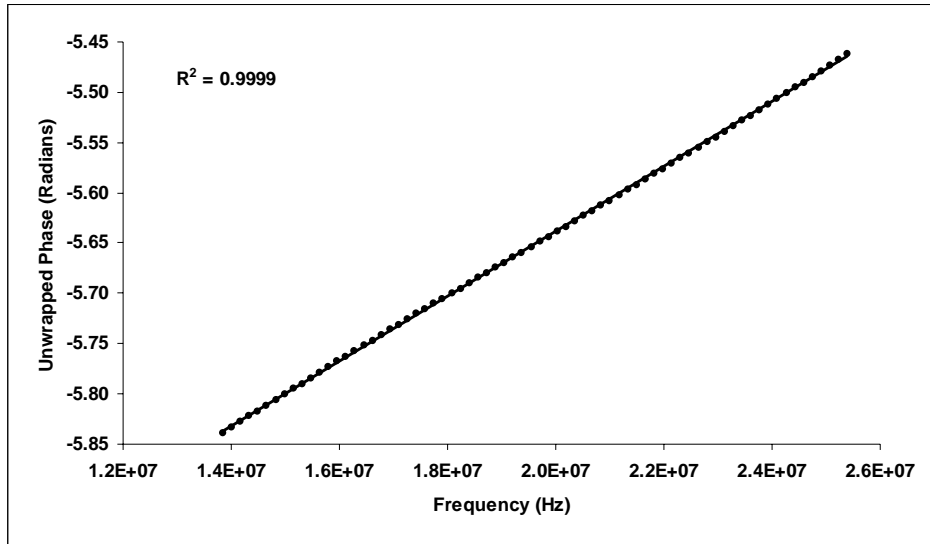
(a)
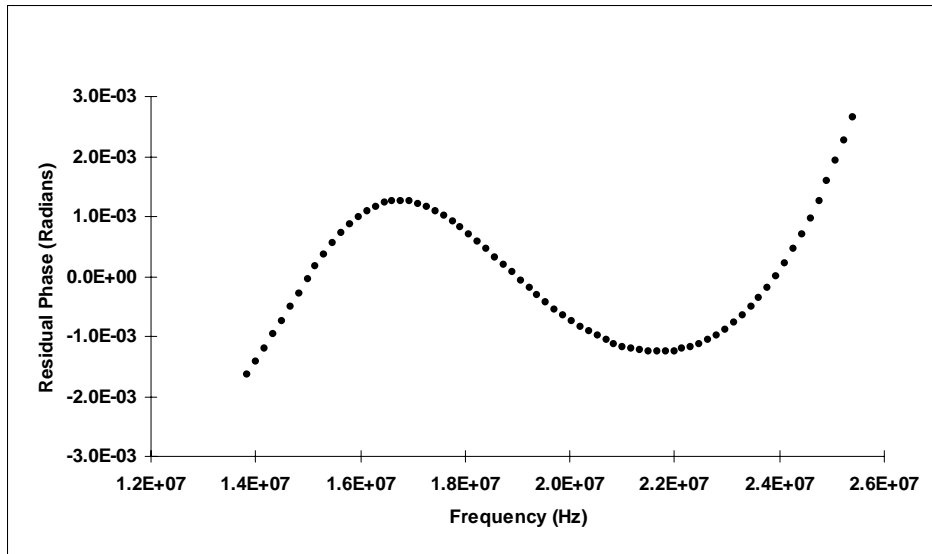
(b)

Figure 3.3.3-1. Linear regression of phase on frequency: (a) least squares linear line fit and (b) residuals from regression fit in "a"

3.4   Residual Stress Gradient Measurements Using Energy-Dispersive X-Ray Spectroscopy

3.4.1   Approach

The measurement of residual stress as a function of depth by x-ray techniques is limited by practical considerations, namely counting time. The basic limits on penetration depth, set by background and peak overlap, imply that the required energies are high compared to standard diffraction sources. A series of breadboard tests at the ARACOR

laboratories in California did show that shifts in diffraction peaks due to stress could be measured using energy-dispersive spectroscopy. The study also indicated that it is more feasible to make that type of measurement by using the higher energies available in the FeinFocus source or the LAM/DE source.

Experiments were then conducted in AFRL/MLLP using the 420 kV source of LAM/DE to obtain x-ray diffraction data from titanium samples. Spectra were recorded using a titanium sample with a peened area, as well as an unpeened area. The spectra from the unpeened area showed that the diffraction peaks did not show a shift in energy as the psi angle was varied. However, the spectra from the peened area demonstrated that the diffraction peaks shift in energy as the psi angle was varied.

3.4.2 Results

The analysis of the spectra obtained from the peened area of the titanium sample indicated very convincingly that this technique showed a depth dependence of the stress. The final step of the analysis was the conversion of the results relating stress as a function of attenuation depth in the material to stress as a function of geometric depth into the material.

3.4.3 Reports (Not Published)

The following unpublished reports were written by ARACOR personnel and provided to AFRL/MLLP at the time of completion of each of the tasks on this project:

- "Measurement of Residual Stress Gradient Using Energy-Dispersive X-Ray Spectroscopy – A Feasibility Study"
- "Technique for Extracting Depth Dependence of Stress."
- "Analysis of the Additional Ti-6-4 Data Taken at WPAFB"
- "Conversion of τ-Dependence of Stress to Z-Dependence"
- "Identification of Peaks Other Than α-Titanium"

3.5 Nondestructive Characterization of Fretting Fatigue

3.5.1 Air Force Need

Fretting fatigue occurs between two surfaces in contact under a load that are experiencing small amounts of relative motion (20 to 100 microns). The near-surface damage caused by fretting-induced fatigue (fretting fatigue) has been the origin of cata-

strophic failures in many industrial and aerospace components. Examples of catastrophic failures due to fretting fatigue can be found in varieties of parts in helicopters, fixed-wing aircraft, engines, construction equipment, orthopedic implants, blade/disk dovetail joints, keys, cranes, nuclear reactor components, turbine blade rotors, etc. [8,9]. Recent problems in high-performance aircraft, especially in engine components, have caused the Air Force to seek a basic understanding of the problem so that measures for prevention can be developed and applied.

3.5.2 Current Approach

Since fretting occurs at the surface of components, it can often be detected by visual means. At present, many of the aerospace components are replaced simply as a result of visual observations. The decision is based on personnel experience and there is no quantitative reasoning behind this visual methodology. More recently, there have been attempts to provide quantitative information based on measures of surface roughness. The surface roughness has been found to increase as the number of fretting cycles increases [10]. These measurements were performed on as-machined surfaces, but most components that are intended for fretting-prone use are subjected to surface treatments, such as shot peening, after machining. This shot peening introduces crack-growth-inhibiting very-near-surface compressive residual stresses that also roughen the surface of the component.

3.5.3 UDRI Approach to Fretting-Fatigue Characterization

UDRI developed a research project to: (1) gain understanding of the behavior of residual stress under fretting-fatigue conditions, and (2) determine the capabilities of x-ray diffraction residual stress measurements for detecting precursors to fretting-fatigue damage, especially in a laboratory setting. Several dog-bone shaped samples of Ti-6Al-4V were shot peened to three different intensities – 4, 7 and 10 Almen – with complete surface coverage in each case. X-ray diffraction was used to measure the surface residual stress prior to subjecting the samples to fretting. The samples were then subjected to fretting fatigue, after which x-ray diffraction residual stress measurements were again made. These measurements were made across the width of the scar, both parallel and perpendicular to the direction of fretting as shown in Figure 3.5.3-1. Figure 3.5.3-2 shows typical measurements results before and after fretting.
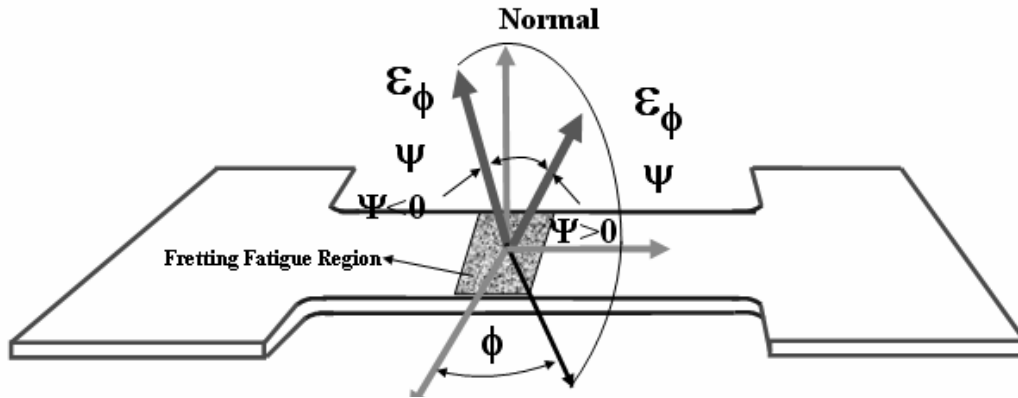
Figure 3.5.3-1. Locations and directions of x-ray diffraction measurements relative to the direction of fretting.
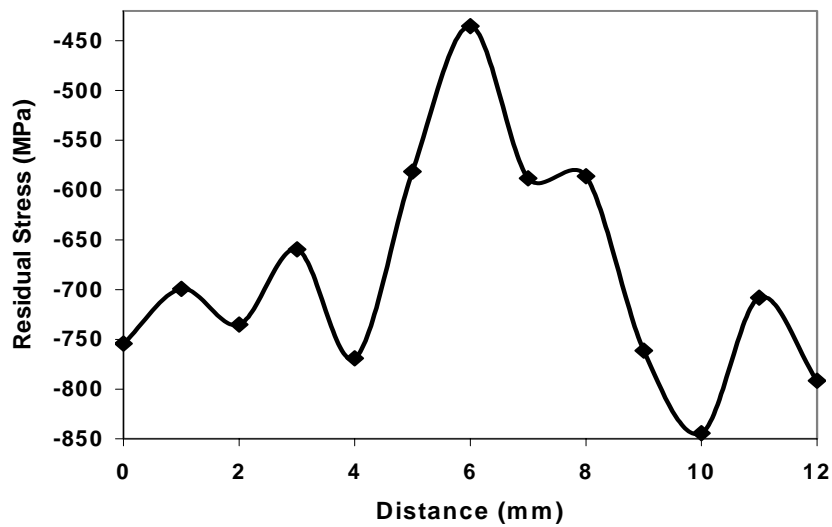
Figure 3.5.3-2. Results of x-ray diffraction measurements of residual stress across a fretting scar in shot-peened Ti-6Al-4V

3.5.4   Results

The major results obtained as a result of analyzing the data from this study are as follows:

1. Prior to fretting, the residual stress in shot-peened samples was found to be spatially and directionally uniform across the samples.

2. Fretting significantly reduced the residual stress both within and beyond the fretting contact region.

3. The reduction in residual stress was found to be proportional to the number of fretting cycles.

4. After fretting, the residual stress was found to be nonuniform across the fretting scar.

5. The residual stress was reduced to zero before the onset of cracking.

6. The residual stress becomes anisotropic in the fretting contact region.

3.5.5 For Additional Information

Additional information about this study can be found in Appendix A in the articles titled "Residual Stress Relaxation Due to Fretting Fatigue in Shot Peened Surfaces of Ti-6Al-4V", and "Residual Stress Distribution on Surface-Treated Ti-6Al-4V by X-Ray Diffraction".

3.5.6 Acknowledgements

This research was performed in collaboration with Sonia Martinez (graduate student), Prof. Shankar Mall, AFIT, Dr. Mark Blodgett, a civilian employee of AFRL/ MLLP, and Dr. Shantanu Namjoshi, former post-doctoral student at the Air Force Institute of Technology.

3.6 Nonlinear Acoustic Parameter Measurements for Accumulated Fatigue Damage Evaluation

3.6.1 Air Force Need

The Air Force needs more reliable assessments of remaining-fatigue life if it is to keep components of the fleet longer than anticipated and yet prevent catastrophic in-service failures. One method for improving the reliability of remaining-fatigue-life-assessments is to improve the ability to nondestructively detect smaller amounts of macro-sized damage, such as cracks and delaminations in materials and structures. However, another and potentially even better method is to detect the accumulation of micro-scale damage, such as the slip bands and dislocations that occur as precursors to the macro-scale damage.

3.6.2 Background

Cyclic loading is known to cause continuous changes, i.e., degradation in the microstructure of metallic materials. That micro-structural degradation over a period of time ultimately leads to fatigue failure. A number of investigations that used high-

resolution transmission electron microscopy (TEM) have provided a basic understanding of the sub-microstructure-level mechanisms that lead to fatigue failure [11-16]. The wealth of literature, particularly on single crystalline materials, indicates different stages in the degradation of microstructure due to cyclic loading. The very first few cycles of load produce dislocations with positive and negative Burger's vectors that accumulate on the primary glide planes of the material. When the positive and negative dislocations approach each other, a dislocation dipole is formed. With continued cyclic loading, the density of dislocations increases, forming network or veins/bundles. Increased dislocation density leads to the formation of slip bands that appear on the surface of the sample. On further cyclic loading, the slip bands act as stress concentrators that initiate micro-cracks. Continued cyclic loading assists the growth of micro-cracks to create final failure [11,16].

Research in the field of fatigue damage has been largely limited to mechanical testing, TEM, and fracture mechanics. While these techniques have provided a means for basic understanding of the mechanisms and a criterion for designing components based on laboratory testing, they do not offer a methodology for inferring accumulated fatigue damage in a nondestructive way. Recent developments [17-23] in nondestructive evaluation have shown that nonlinear acoustic properties of metals are sensitive to accumulated fatigue damage. In nonlinear acoustic measurements, an acoustic wave of fundamental frequency "f" is propagated through the sample and the second harmonic signal "2f" that is generated by the material is detected. The amplitude of the transmitted fundamental frequency signal "A_1" and the amplitude of the second harmonic signal "A_2" are used to determine the nonlinear acoustic parameter, "β" as,

$$\beta = [2v_l^2/af^2\pi^2]\,(A_2/A_1^2) \tag{4}$$

where "v_l" is the longitudinal wave velocity, "f" is the frequency of the acoustic wave and "a" is the sample length.

The nonlinear acoustic parameter has been shown to increase with increasing number of load cycles. A dramatic increase of 200 to 300% has been observed in metallic materials before final fracture. Recent experiments at UDRI on dog-bone-shaped Ti-6Al-4V specimens [24] have shown that the nonlinear acoustic parameter changes dramatically and also varies across the gauge length of the specimen used in the investi-

gation (see Figure 3.6.2-1). The nonlinear acoustic parameter remains close to that of a virgin specimen in the grip section, but increases exponentially and approaches 200% near the fracture edge. These experiments have provided a new methodology for quantitatively evaluating the accumulated fatigue damage. While the experimental results have shown a correlation between the nonlinear acoustic parameter and micro-structural fatigue-damage accumulation, the question remains as to what change in value of the nonlinear acoustic parameter indicates a significant probability of failure. Answering that question requires a better understanding of the basic mechanisms that are responsible for the increase in the nonlinear acoustic parameter due to fatigue-damage accumulation.

It is known that, due to cyclic loading, dislocation structures are generated in the metal. When an acoustic wave propagates through a metal that has been subjected to cyclic loading, it interacts with the metallic lattice, grain boundaries, defects, and the dislocation structures. One of the important features of cyclic-loading-generated fatigue damage is the presence of dislocation dipoles. The acoustic waves interact both with individual dislocations as well as with the dislocation dipoles. The contribution of individual dislocations to the value of the nonlinear acoustic parameter is quite small in polycrystalline materials [18,25].
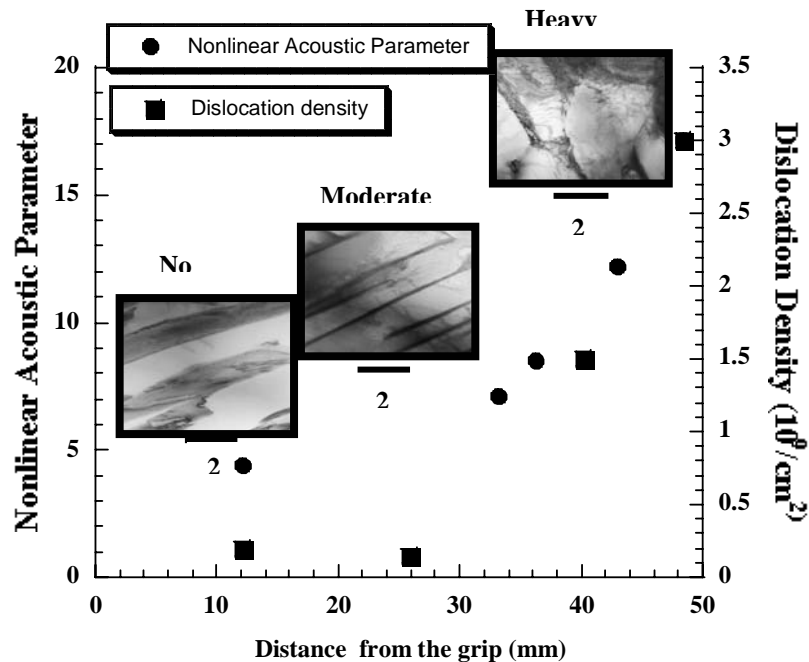
Figure 3.6.2-1. Variation in dislocation density and nonlinear acoustic parameter across a fractured Ti-6Al-4V dog bone sample (from ref. [24,27]).

30

In general to study the interaction of acoustic waves with dislocation dipoles and to evaluate their contribution to the nonlinear acoustic parameter, the geometric displacement of an acoustic wave by the lattice structure and by dislocation dipoles has to be calculated. This displacement was used by Cantrell and Yost [18] to solve the acoustic wave propagation equation. The results obtained by Cantrell and Yost [18] are provided in equation 5:

$$\beta = \beta_{lat} + \beta_{dip} = -\left(\frac{3C_{11} + C_{111}}{C_{11}}\right) + \frac{16\pi^2 gR^2(1-\nu)^2(C_{11})^2}{G^2 b}\Lambda\left[\frac{Gb}{8\pi(1-\nu)\tau_s}\right]^3 \qquad (5)$$

In equation 2, "C_{11}" is the second order elastic constant of the material, "C_{111}" is the third order elastic constant, "g" is the conversion factor from dislocation displacement in the slip plane to the longitudinal displacement "u_{dip}", "R" is the Schmidt factor that defines the directional dependence of slip, "ν" is Poisson's ratio, "G" is the shear modulus, "b" is the Burgers vector, and "τ_s" is the critical resolved shear stress. The first term in equation 5 is the contribution from the lattice "β_{lat}" and the last term is the contribution from the dislocation dipole "β_{dip}". Generally, equation 5 is applicable to FCC- and BCC-structured metals [11,26].

During fatigue of metallic materials, the microstructure of the material undergoes continuous change. Particularly the density of dislocation as well as the dislocation dipole density increases. The lattice contribution to the total nonlinear acoustic parameter doesn't change. Thus, it can be seen from equation 5 that the nonlinear acoustic parameter increases with increasing dislocation density. Recent high resolution TEM studies have established that the deformation behavior of titanium and titanium alloys under cyclic loading are similar to that of BCC-structured metals [11,26]. Based on these observations it should be possible to utilize equation 5 to theoretically evaluate the nonlinear acoustic parameter in fatigue-damaged Ti-6Al-4V.

3.6.3 Results

Maurer [27] recently performed extensive transmission electron microscopic examinations of fatigued Ti-6Al-4V samples. These samples were obtained from the same batch of titanium plates as those that were used in nonlinear acoustic parameter measurements performed by Frouin [24]. Assuming that near the fractured edge the majority of

the dislocations are dipoles and that the nonlinear acoustic parameter can be evaluated using equation 5 the contribution of dislocation dipoles, "β_{dip}" can be calculated. By substituting G = 40 GPa, C_{11} = 150 GPa, C_{111} = -1100 GPa, b = 0.25 nm, R = 0.33 (unitless), ν = 0.33, τ_s = 0.1 GPa into equation 5 and using the TEM measurement of dislocation density the contribution of dislocation dipoles (β_{dip}) was calculated to be 12.

The experimentally-measured total "β" for different samples near the fractured edge was found to be in the range of 14-18. On the same samples, the "β" value in the grip section was found to be between 5 and 6. Assuming the grip to be in the undamaged state, the measured "β" is approximately that of the metallic lattice nonlinear acoustic parameter "β_{lat}". The average change in the nonlinear acoustic parameter due to fatigue is, therefore, between 9 and 12. This change is essentially due to the contribution from dislocation dipoles. The experimentally-determined nonlinear acoustic parameter due to dislocations of 9 to12 is in good agreement with the theoretically evaluated result of 12.

The agreement between the experimental measurements and theoretically-evaluated result shows that the nonlinear acoustic parameter can be utilized to evaluate accumulated fatigue damage in metallic materials.

Section 4
Corrosion-Related Research

4.0   **Introduction**

4.0.1   <u>Air Force Need</u>

The Air Force decision to continue use of major portions of its existing fleet to well beyond the designed-for lifetime obviously necessitates the need for reliable nondestructive evaluation methods for detecting fatigue damage. Increasing the service life of aircraft also increases the likelihood of corrosion. Since corrosion increases the probability of initiation of crack initiation and growth, increasing the service life also necessitates the need for NDE methods that can reliably detect and characterize corrosion. That is especially true for corrosion that is hidden from view in multi-layer structures or that has initiated under corrosion-preventive coatings.

4.0.2   <u>UDRI Approach</u>

UDRI personnel conducted and/or participated in several corrosion-related projects to fulfill the Air Force's need for corrosion detection and characterization. One of these, "Characterization of Corrosion in Aircraft Structures", explored the capabilities and limitations of Giant Magnetoresistive (GMR) sensors for characterizing corrosion in thick, multi-layer structures. That project had four major thrusts: (1) GMR sensor characterization, (2) development of a corrosion metric, (3) optimization of material processing, and (4) model validation. This major Air Force collaborator on this project was Mr. Jeremy Knopp, a civilian employee of the Air Force in AFRL/MLLP.

Another project, "NDE Methods for Characterizing Corrosion-Prevention Coatings", explored the capabilities of Fourier Transform Infrared (ATRFTIR) spectroscopy and White Light Interference Microscopy (WLIM) for characterizing the degradation of corrosion-preventive coatings that are used on aircraft structures.

"Corrosion and Fatigue Studies on Aluminum and Titanium Alloys" was conducted in collaboration with Dr. James Blackshire, a civilian employee of the Air Force in AFRL/MLLP. That project focused on methodology for controlled growth of corrosion damage and, specifically, for controlled growth of corrosion pits. In addition, the

use of near-field scanning interferometry was studied for its use in monitoring fatigue crack initiation and growth that originated from corrosion pits.

"Three-Dimensional Corrosion-Growth Monitoring" was a collaborative effort among ARACOR, UDRI, and AFRL/MLLP personnel. X-ray CT and ultrasonic techniques were used to monitor – in three dimensions – accelerated intergranular corrosion growth in a cylindrical rod of 2024 T4 aluminum.

The "Operability of the Honeywell Corrosion Environment Monitor System (CEM)" was conducted in collaboration with Mr. John Barnes and Mr. Charles F. Buynak, both civilian employees of the Air Force in AFRL/MLLP. This program concentrated on calibration of sensors in the CEM, determining the accuracy of the CEM sensors, and analyzing environmental data that was recorded by the CEM while installed on a C-141 aircraft.

"Corrosion Detection and Quantification Capabilities of SAIC System" was funded through this contract, but was conducted offsite as a part of the Automated Corrosion Detection Program" managed by Mr. Wally Hoppe, a UDRI employee. Personnel assigned to this project collected and analyzed data to determine the corrosion detection and quantification capabilities of SAIC eddy-current and ultrasonic scanning systems in a depot-like environment.

4.1   Characterization of Corrosion in Aircraft Structures

4.1.1   UDRI Approach to Corrosion Characterization

Results from a previous Automated Corrosion-Detection Program [28-30] have identified ultrasonic and eddy current as the two best nondestructive technologies for detecting and quantifying (at least in terms of POD) corrosion that is hidden between the first and second layers of aircraft fuselage skins. Both of these technologies have limitations for detecting corrosion beyond the first layer. With eddy current, the frequency must be extremely low to penetrate beyond a few millimeters. With what is considered to be conventional eddy current techniques, this results in a significant loss of sensitivity. Also, the variable air gap that sometimes exists between layers in a multi-layer structure can become a significant source of variability in eddy current output. With ultrasonics, an air gap between layers results in nearly 100% reflection of the interrogating energy, thereby making inspection beyond the air gap impossible.

Thus, eddy current would appear to be the characterization method of choice for the inspection of multi-layer structures, especially if the loss of resolution at lower frequencies can be overcome. The loss of sensitivity results from the ineffectiveness of a conventional eddy-current coil to sense the low-frequency magnetic field because the output of the coil is proportional to the time derivative of the magnetic field. Thus, as the frequency decreases (time increases), the time derivative decreases. However, the more-recently-developed Giant Magnetoresistive (GMR) sensors sense the magnetic field directly and, therefore, do not lose sensitivity at lower frequencies. Thus, it may be possible to use a GMR sensor for reception of the eddy-current signal during inspection of multi-layer structures at lower frequencies without the usual loss of sensitivity.

Because of this potential for relatively-high sensitivity at the low frequencies that are necessary for inspection of thicker or multi-layer structures, UDRI undertook a four-part study to determine the capabilities and limitations of the use of GMRs for corrosion characterization. Those four parts (areas) were: (1) sensor characterization, (2) development of a corrosion metric, (3) material substitution, and (4) model validation. The four areas are briefly described in the paragraphs that follow.

4.1.2 Area 1 – GMR Sensor Characterization

Air Force Need

At an operating frequency of 2 kHz, eddy currents will penetrate to a depth of about 2.7 mm in aluminum with unity permeability and resistivity of 5.766×10^{-08} Ohm-meter. That is equivalent to two layers of a typical aircraft aluminum structure. As the thickness increases to 4 mm – a typical four-layered aluminum aircraft structure – the operating frequency must drop below one kilohertz. Indeed, frequencies as low as 100 Hz are needed for the 12 mm thickness that is sometimes encountered. As discussed in preceding paragraphs, the typical eddy-current coil receiver would be very insensitive at such low frequencies. Thus, UDRI decided to characterize the more promising GMR sensors for such low-frequency applications.

Technical Approach

The initial focus of the effort was the response of the sensor to a DC field. Results of the DC-field test indicated that the strength of the magnetic field was inversely

proportional to the cube of the distance between a magnet that generated the DC magnetic field and the GMR sensor.

For the AC-field test, a coil driven by a function generator was used to create a magnetic field. The magnetic field generated by the coil was, in turn, used to evaluate a GMR sensor. Initially, a homemade Brooks coil was used to generate the magnetic field and a function generator was used to generate single-frequency sinusoidal waves that drove the Brooks-coil transmitter. An oscilloscope was used to measure the amplitudes of the input to the transmitter and the output from the GMR receiver. The ratio of the output amplitude from the GMR to the input amplitude applied to the transmitter served as a measure the GMR response.

A series of resonant circuits consisting of coils with various capacitors was then constructed to allow generation of magnetic fields in the desired frequency range. The measured resonant frequencies of these coils ranged from 18 kHz to 17 MHz. They were subsequently used to generate the dynamic (AC) magnetic fields that were needed for characterizing the frequency responses of GMR sensors.

Test Results

Figure 4.1.2-1 shows received signals for both a 1st and an effective 2nd harmonic signal taken from two separate tests. The generation of an effective 2nd harmonic signal is common with a GMR sensor. The effective 2nd harmonic signal is generated during the normal mode of operation (which is without a DC bias) because the sensor does not discriminate the direction of the received field. Thus, the received signal appears to be rectified and its frequency content becomes twice of that of the input signal. Because this effective 2nd harmonic signal is analyzed exactly as if it was a true 2nd harmonic signal, it will be referred to hereafter as simply 2nd harmonic. Applying a bias with a small magnet that was moved toward the GMR sensor until the signal amplitude was maximized generated the 1st harmonic signal. The signal was acquired at that maximum amplitude. The 2nd harmonic signal was acquired without any external bias. The minor imbalance in the received signal might be due to the hysteresis in the sensor. It can be seen that the amplitude of the maximized 1st harmonic signal was about twice that of the 2nd harmonic

mode and the period was doubled. The background level (dotted curve) was also plotted for comparison.
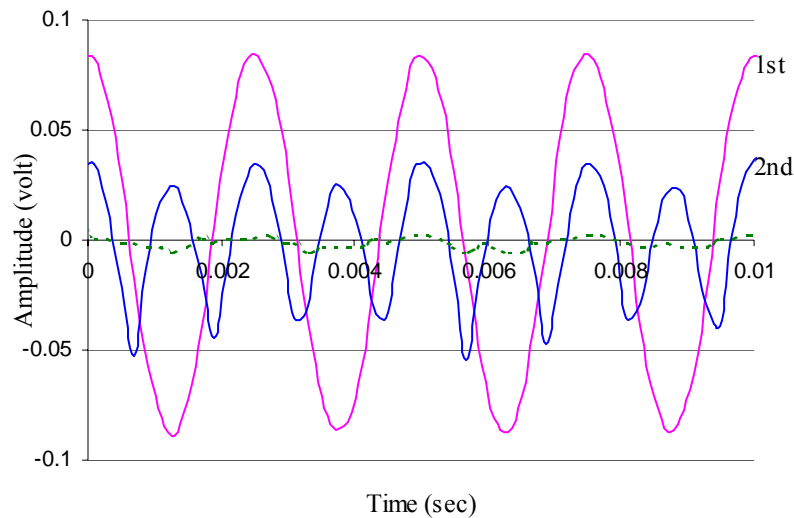
Figure 4.1.2-1. Comparison of time domain signals from the 1st (larger amplitude) and 2nd (higher frequency) harmonic mode, and background noise (in dotted curve).

A series of quantitative measurements was conducted to characterize the frequency response of a GMR sensor. Figure 4.1.2-2 shows the frequency response of a GMR sensor in an unbiased case. An exponential curve was fit to the data to better illustrate the trend. The experimental results showed that the GMR sensor has a flat response at low frequencies up to 1 MHz. For frequencies above 1 MHz, the amplitude response of the GMR sensor decreased steeply (a 20 dB drop from 1 MHz to 17 MHz). To further test the low-frequency response of the GMR sensor, a 3 mm (122-mil) thick aluminum plate, which simulates the two-layer lap joints commonly found in KC-135 and Boeing 707 aircraft, was used to determine whether or not the sensor could detect the magnetic field through the plate. The results indicated that the sensor could easily detect signals in the kHz range through the thickness of the plate. Then, to qualitatively test the sensitivity of the GMR sensor to thickness variations that would occur as a result of buried corrosion, an additional 0.75 mm (30-mil) thick aluminum plate was placed next to the 3 mm (122-mil) plate. The GMR sensor was able to distinguish the difference in thickness well.
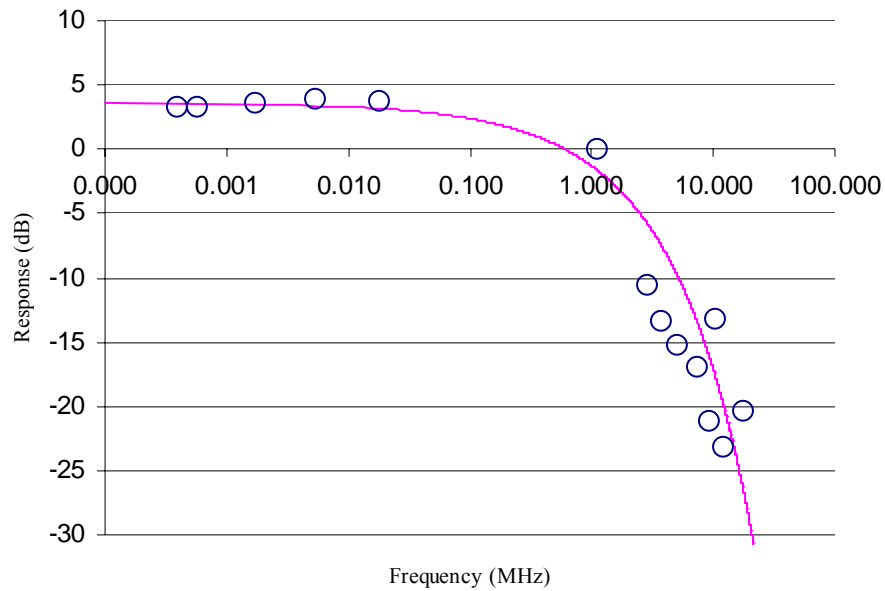
Figure 4.1.2-2. Experimental measurement of the frequency response of a GMR sensor.

The results of the sensor characterization testing indicate that the frequency characteristics of the GMR sensor should be adequate for most of the conventional eddy current testing. But more important, the two characteristics of the GMR sensor that could be most useful for nondestructive testing are bandwidth and low-frequency response. The broad bandwidth could have an advantage over the conventional coil for those tests in which more than one frequency is needed. Potential applications of this characteristic are multi-frequency testing and pulsed eddy current testing. The low-frequency response characteristic, on the other hand, makes the GMR sensor a good candidate for detecting hidden anomalies under highly-conductive materials. This is the case for aluminum alloys for which it is difficult to inspect at some of the required depths with a coil receiver.

For Additional Information

Additional details of the sensor characterization in this task can be found in the articles titled: "The Use of Giant Magnetoresistive (GMR) Sensor for Characterization of Corrosion in a Laboratory Specimen", and "Application of a Giant Magnetoresistive (GMR) Sensor for Characterization of Corrosion in a Laboratory Specimen". These articles are included in Appendix A.

4.1.3   Area 2 – Development of Corrosion Metrics

Air Force Need

Advancing corrosion converts the metal structure into corrosion products, thereby reducing the local thickness of the metallic structure or skin. It is this local material, or thickness loss, that is sensed by the eddy current. Thus, to accurately measure and/or image this local thickness loss, a metric (signal characteristic) is needed.

Technical Approach

The skin effect (signal decay with depth) for a changing magnetic field in an infinite half-space [31] can be described in two ways: (1) the exponential decay of current density as a function of depth in materials, and (2) the linear phase lag as a function of depth. Both of these characteristics provide a potential metric for the application of a GMR sensor for local thickness loss (corrosion depth) monitoring. In this case, the phase lag is different from the commonly-known impedance-plane phase angle that is widely used in conventional eddy current instruments for flaw detection purposes. That impedance-plane phase angle describes the angle between a flaw signal and a liftoff signal. These two quantities are related, but the phase lag bears a direct physical relationship to the local thickness of the material and, therefore, to the thickness loss due to corrosion.

Because of its very high precision and accuracy, a lock-in amplifier was used to drive the transmitting eddy-current coil and to monitor the output from the GMR receiving sensor. This amplifier uses a technique known as phase-sensitive detection to identify the component of the signal at a specific frequency and phase. Noise signals at frequencies other than the reference frequency are rejected. Figure 4.1.3-1 shows a schematic of the instrumentation that was used for the data acquisition during development of an eddy-current corrosion metric.
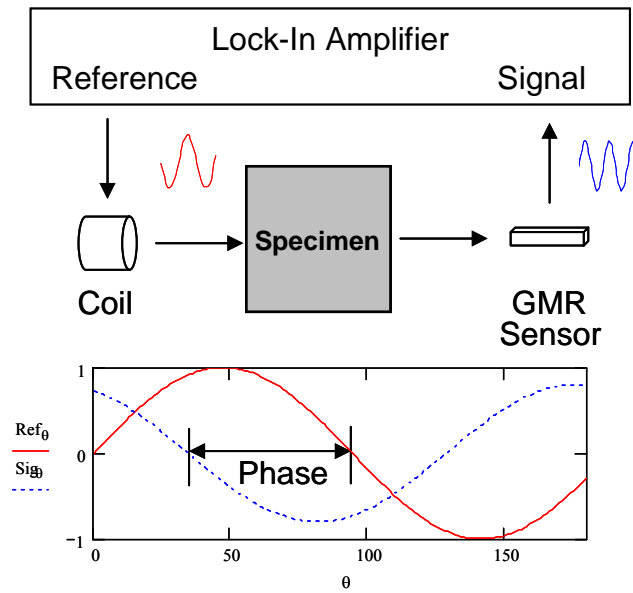
Figure 4.1.3-1. Schematic of the instrumentation together with a plot illustrating the phase difference between the reference signal and the through thickness, as-received GMR-detected eddy-current signal.

A multi-layered specimen that consisted of seven 0.75-mm-thick layers was fabricated to test the capability of a GMR sensor for monitoring local thickness variations under conditions that are likely to be encountered during hidden-corrosion monitoring. Since the measurement was conducted with an un-biased GMR sensor, the output mode in the lock-in amplifier was set to the frequency of the 2nd harmonic. Both the amplitude and phase components of the signals were examined experimentally. The results indicate that the amplitude decreases exponentially as the thickness increases in the test range from 1.2 kHz to 2.7 kHz. The phase, as derived from the output of the lock-in amplifier, also decreases as the thickness increases. The phase must be unwrapped if it decreases beyond -180 degrees.

Test Results

The plots in Figures 4.1.3-2 and 4.1.3-3 show the magnitude and phase values of the signal from the GMR sensor as a function of the material thickness. The three frequencies (1.3, 1.9, and 2.5 kHz) were chosen to represent the low, medium, and high frequencies in the range of interest. The plot in Figure 4.1.3-2 shows that the magnitude of the received signal decreased exponentially as the thickness increased. As the thickness became large, the difference in amplitudes among the signals decreased. However, the plot in Figure 4.1.3-3 shows that the phase difference among the frequencies

increased as the thickness increased. In addition, the relationship between the phase change of each signal and the thickness was linear. Thus, this phase value could be a potential metric for monitoring local thickness variations due to hidden corrosion.
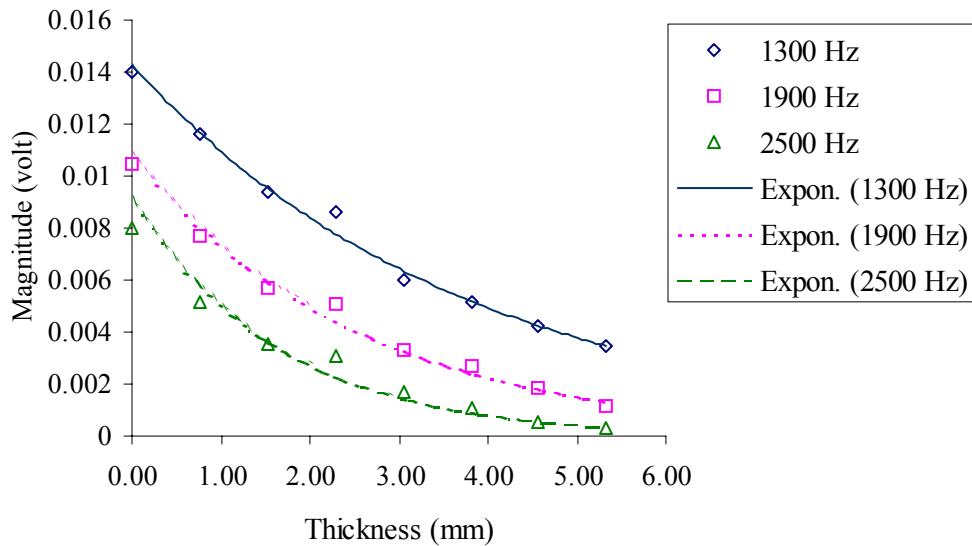
Figure 4.1.3-2. Changes in GMR signal magnitude (at three frequencies) with thickness. The sample was a multi-layered laboratory specimen.
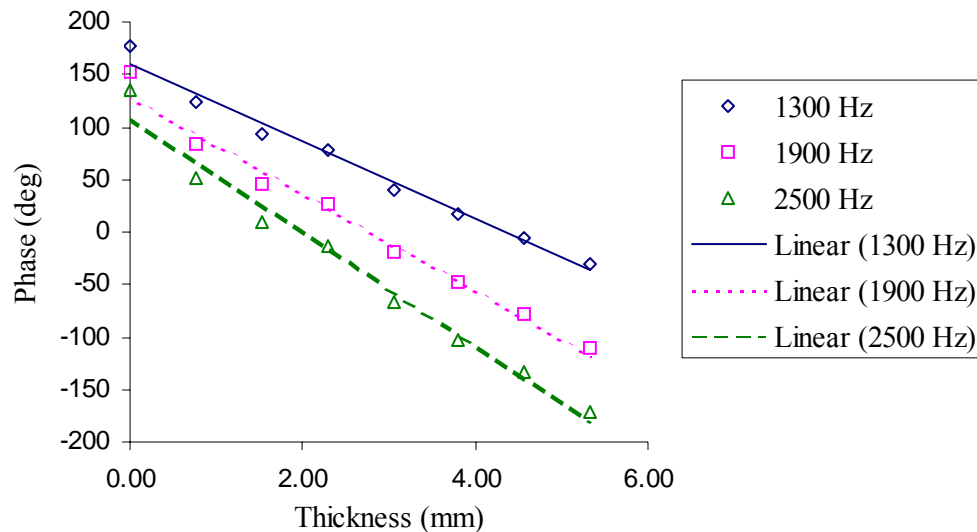
Figure 4.1.3-3. Changes in GMR signal phase (at three frequencies) with thickness. The sample was a multi-layered laboratory specimen

The phase of circular functions is only measured modulo π. Therefore, it must either be arithmetically unwrapped by adding π radians to the output or subtracting π radians from the output when a boundary is crossed; or, the analyst can rotate the impedance plane so that the phase data does not cross the $\pm\pi$ radians boundaries.

Rotating the impedance plane was chosen due to its ease of implementation. This rotation is similar to changing the reference phase angle in the more-conventional impedance plane measurements. It changes the absolute phase angle, but does not effect the change in phase as a function of material thickness. Experimental data showed that, after rotation, the phase angle does not cross one of the reversal boundaries for thickness in the range 0 to 5.3 mm (0 to 0.210 in.), at least for frequencies between 1.3 kHz and 2.5 kHz. This verifies that the phase approach – after a proper rotation of the initial phase angle – can be used as a metric to quantify local material thickness variations such as those that are caused by corrosion. Figure 4.1.3-4 shows the rotated lock-in amplifier phase from a multi-layered laboratory specimen at various frequencies.
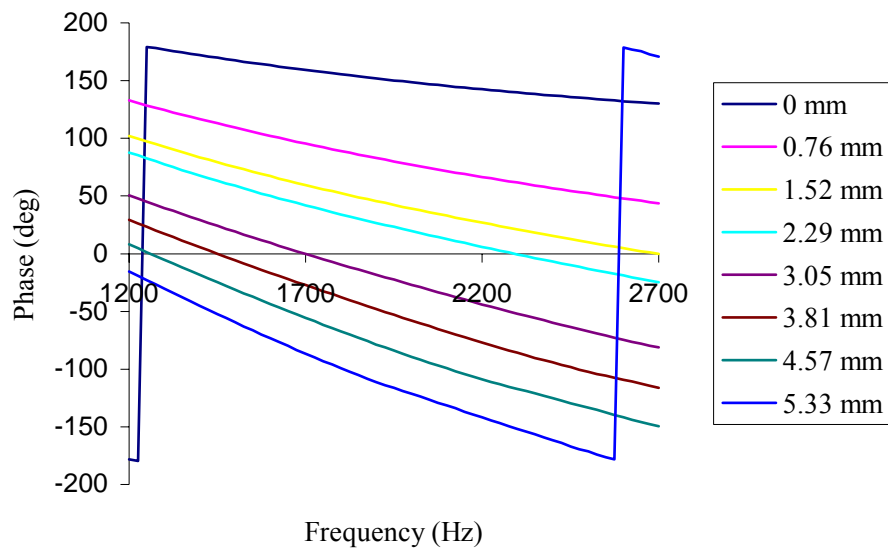
Figure 4.1.3-4. Lock-in amplifier phase output (at various thicknesses) as a function of frequency. The sample was a multi-layered laboratory specimen.

After identification of metrics for measurement of local thickness loss due to corrosion, a computer-controlled system – referred to as NETSCAN II – was developed in AFRL/MLLP for acquisition of the metrics during scanning of laboratory specimens. This allows images to be generated from the acquired values. While phase is the metric of choice, both signal magnitude and phase can be acquired and used to generate images of local thickness variations with NETSCAN II.

For Additional Information

Additional details of the sensor characterization in this task can be found in the articles titled: "The Use of Giant Magnetoresistive (GMR) Sensor for Characterization of Corrosion in a Laboratory Specimen", and "Application of a Giant Magnetoresistive (GMR) Sensor for Characterization of Corrosion in a Laboratory Specimen". These articles are included in Appendix A.

4.1.4   Area 3 – Material Substitution

Air Force Need

AA 7075-T6, a widely-used aircraft material, has been found to be prone to corrosion. To maintain the high strength of the T6 temper, but gain the corrosion resistance of the T73 temper, a two-step heat-treatment process (retrogression and reaging) [32,33] is applied as shown in Figure 4.1.4-1. The timing in the retrogressing step, as highlighted in the figure, is critical to obtain the needed material qualities, so a hardness measurement is typically used to determine the material strength. Because the currently-used hardness test is destructive, the Air Force needs a nondestructive characterization method to assure that the optimal material state has been achieved.
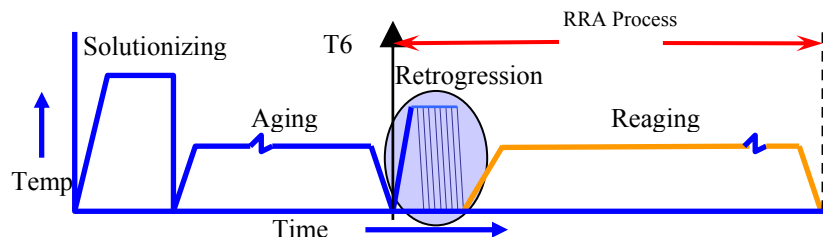
Figure 4.1.4-1. Schematic of the Retrogression and Reaging (RRA) process for AA 7075-T6: (1) Retrogressing (at 195°C for a few minutes) and (2) Reaging (at 121° C) for 24 hours.

Technical Approach

Eleven specimens that had been solutionized and aged were subjected to retro-gression (heat treatment) for durations that ranged from 30 to 50 minutes in 2-minute increments. After cooling, each specimen was subjected to four different types of measure-ments. Three of the measurements (electrical conductivity, eddy-current phase lag, and nonlinear acoustic parameter) were made for correlation with the fourth measurement, i.e., Vickers hardness. The electrical conductivity data (made with a commercial conduc-tivity meter) showed only small differences (within 2% IACS) with large scatter when correlated with Vickers hardness data. Phase lag measurements made with an instrument setup as shown in Figure 4.1.3-1 (coil transmitter, GMR receiver and lock-in amplifier) provided reliable data with low scatter. The plot in Figure 4.1.4-2 shows that the phase output from the GMR receiver reached a clearly-discernable minimum at a retrogression time of 42 minutes. The nonlinear acoustic parameter shows 2 peaks when plotted as a function of retrogression time (Figure 4.1.4-3) during RRA. The first peak is between 20 and 40 minutes, whereas, the second peak is at 45 minutes. This is similar to the results obtained by Cantrell and Yost for aging of AA 2024-T4 to T6 [34-36]. Additional measurement with Vickers hardness as a function of retrogression time also shows two peaks. The first peak occurs after 20 min. and the second at 40 min. A maximum of the nonlinear acoustic parameter and a minimum of eddy current phase occur at a time of 42-45 minutes where optimized material hardness and corrosion-resistance properties have been observed.
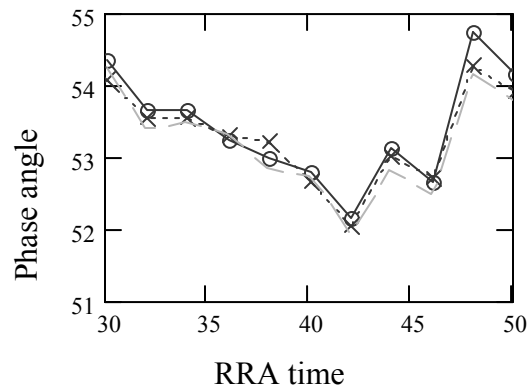
Figure 4.1.4-2. Eddy-current phase angle (degrees) as a function of heat-treatment [Retrogression and Reaging (RRA)] time.
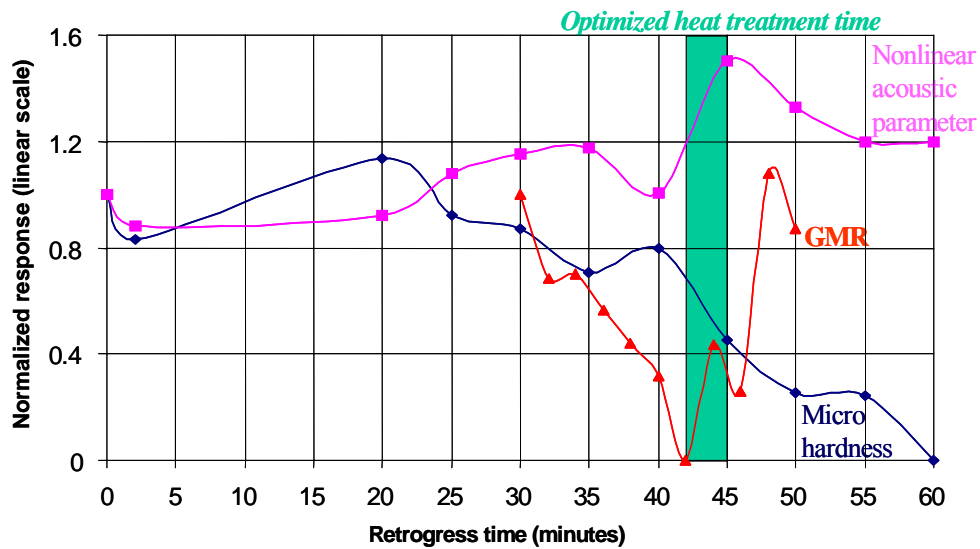
Figure 4.1.4-3. Plots showing a maximum in the nonlinear acoustic signal and a minimum in the GMR-detected eddy-current phase difference at a time of 42 to 45 minutes, at which time optimized material properties were observed.

In addition to the nonlinear acoustic parameter measurement, the phase-lag measurement can provide a precise nondestructive test for monitoring the minute conductivity change during the RRA process. Use of the phase-lag measurement method significantly increases the opportunity to identify the exact heat treatment situation and to achieve the best corrosion and strength properties of the material.

For Additional Information

For more detailed information about this task, please see the article titled: "Nonlinear Acoustics and Eddy Current Characterization of Retrogression and Re-Aged AA 7075", "Characterization of Retrogression and Re-aging Heat Treatment of AA 7075-T6 Using Nonlinear Acoustics and Eddy Current". These articles are included in Appendix A.

4.1.5   Model Validation

Air Force Need

A well-validated model of eddy-current generation and reception that uses a variety of transmitting-coil configurations and a variety of materials and geometries in conjunction with different GMR receivers could significantly improve the interpretation of eddy-current characterization results and extend the general usefulness of the eddy-current

technique. For those reasons, a decision was made to develop and validate a model of eddy-current response under a variety of operating, material, and geometrical conditions.

Technical Approach

Mr. Jeremy Knopp, a civilian employee of the Air Force in AFRL/MLLP, is developing a model of eddy-current response to cracks around fastener holes using the newly-acquired software-modeling tool, VIC-3D®. Dr Ray Ko, a UDRI employee, designed and conducted an experiment that would serve as a guide for the model development.

In this task, a benchmark problem was devised to validate the accuracy of the model. Two 2024-T3 aluminum plates with a conductivity of 18.76 MS/m were used. The plates each had a length, width, and thickness of 76.2 mm, 76.2 mm, and 0.81 mm, respectively. A hole with a radius of 4.0 mm was drilled through both of the plates. Finally, a notch with a width of 0.22 mm and a length of 2.27 mm was made in one of the plates as shown in Figure 4.1.5-1.

Initially, a coil was used as the transmitter and a GMR was used as the receiver to monitor the response of the signal. Experimental results using this setup showed a change of the symmetrical pattern in both magnitude and phase due to the presence of the flaw. However, it was difficult to model this experimental setup with the VIC-3D® modeling tool. Therefore, data were acquired with a different experimental setup. This second setup used a commercial coil for both transmission and reception of the eddy-current signal. The geometric dimensions of the coil and ferrite core were measured and used as inputs to the model. With this setup, a 20 mm square area was scanned using a step size of 0.5 mm and a measured liftoff of 1.0 mm. The experimental data was acquired using a lock-in amplifier that measured both the magnitude and phase of the voltage across the coil. The eddy current probe contains two bobbin coils manufactured by UniWest, but only the coil facing the specimen was used for this experiment. The amplifier excited the coil with a 5.0 kHz sinusoidal signal and the received signal was compared to the excitation signal for phase and magnitude determination.
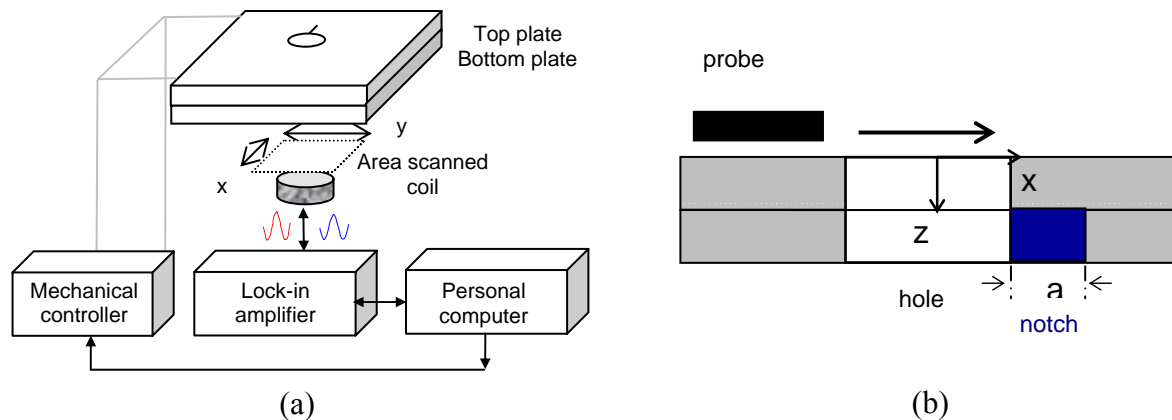
Figure 4.1.5-1. (a) A schematic view of the experimental setup showing a coil scanning of the hidden side of a through-thickness flaw in the top plate of a two-layer fastener-hole specimen, (b) Raster line scan over the flaw.

Test Results

The results for the phase and magnitude components of voltage measurements are shown in Figure 4.1.5-2. Results from preliminary numerical modeling efforts were qualitatively similar to the experimental results obtained by scanning a fastener hole that had a flaw. The preliminary numerical model was modified to include the effects of the cables that were used to acquire the experimental data. The cable parameter for the modeling effort was estimated from a simple one-port circuit, and this one-port circuit was used to relate the experimental results in voltage with the modeling results in impedance. The unknown parameters (current and voltage) were estimated from the results of applying a non-linear least squares fit to the data.

Additional numerical analyses at a series of different liftoff distances confirmed that the best agreement between experimental and numerical modeling results was obtained at the same 1 mm liftoff condition that had been used to acquire the initial data. Repeated measurements at different liftoff distances have been conducted to estimate the error in the experimental system. The phase difference between the two minima from two edge-signals that was obtained from the most recent data collection effort was very close to those obtained during previous data collection efforts, however, the absolute phase obtained

during the most recent experiment was shifted from those obtained previously. This shift may be due to the variations of the mechanical setup, such as the alignment between the probe and the specimen or alignment of the setup.
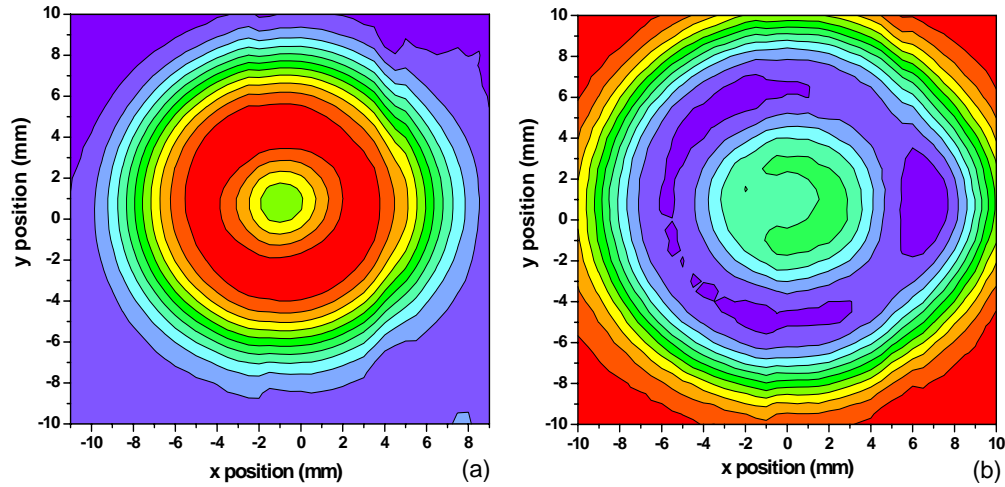
Figure 4.1.5-2. Experimental voltage data: (a) magnitude and (b) phase.

The magnitude and phase of the experimental and simulation results for the raster line scan across the flaw are shown in Figure 4.1.5-3(a) and 4.1.5-3(b), respectively. Over-all, the agreement for both magnitude and phase between the model and experiment was quite good. The asymmetry of the phase response due to the crack is clearly shown. Based on the increased need for model validation, it was decided that the construction of a second NETSCAN system, NETSCAN II, was needed to continue collaborative support for the fastener research while simultaneously maintaining the on-going GMR corrosion study.

For Additional Information

Details of the model validation study conducted in Area 4 can be found in the articles titled: "Numerical and Experimental Study of Eddy Current Crack Detection Around Fasteners in Multi-layer Structures" and "Modeling Eddy Current Crack Detection in Multi-Layer Airframe Structures Using the Volume-Integral Method". These articles are included in Appendix A.
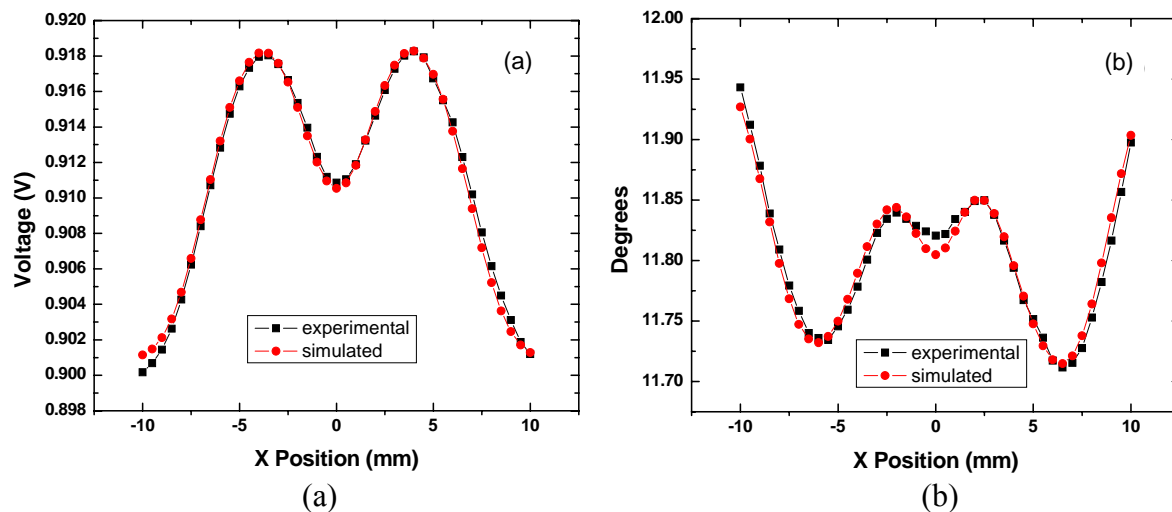
Figure 4.1.5-3. Comparison of experimental and simulated voltage data: (a) magnitude and (b) phase.

4.2 NDE Methods for Characterizing Corrosion-Prevention Coatings

This project was initiated to develop a nondestructive technique for assessing and monitoring the degradation of corrosion-prevention coatings. Exposure to weather, contaminates and mechanical loads results in a degradation of the protective properties of polymeric coatings that are used by the Air Force for corrosion prevention. These degradations eventually lead to potential sites for corrosion initiation. The Air Force's current investment strategies for corrosion protection on aircraft structures are directed toward a "monitor and manage" maintenance philosophy. The Air Force needs an NDE technique that can both assess the current state of coating degradation and monitor coating degradation so that they can optimize the time interval between paint-removal procedures.

4.2.1 NDE Methods for Coating Characterization

Coating degradation can be divided into two types: mechanical degradation and chemical or physical property degradation. Mechanical degradation results in defects such as cracks, pores, and delaminations leading to a rapid breakdown of the coating and attack of the metallic surface. Chemical degradation results in coating property changes, but may not be immediately associated with a mechanical defect within the coating. The research described here was directed toward assessing the applicability of several NDE characterization methods for monitoring and quantifying both mechanical and chemical degradation in aircraft structural coatings produced by exposure to water, heat and UV radiation.

UDRI chose to begin by examining the primer layer only, rather than the entire coating system. It was thought that this would eliminate some of the variability in the initial experiments. Characterization of primer degradation was determined to be a good starting point for the project, since the primer is the main protection layer for the substrate. Degradation in the primer directly affects adhesion to the substrate which, if compromised leads to corrosion initiation. The polymeric coating used in this study was a bisphenol A epoxy primer that is typical of that used in AF coating systems.

The approach chosen in this program was to examine the physical and chemical changes induced in a model structural coating during weathering exposures using multiple inspection techniques. The results of the examination were then correlated with weathering exposure times. The weathering environment consisted of cyclic exposures to UV light (xenon) heat and humidity, as described in MIL-PRF-85285C. The 2-hour cycles consisted of 102 minutes of xenon light exposure at 60°C, followed by 18 minutes of xenon light with water spray at room temperature. The weathering cycles were repeated to achieve the required exposure time interval. Coating degradation was characterized as a function of total accumulated weathering exposure time.

Chemical changes occurring over a large region of the epoxy during weathering exposure were monitored using Attenuated Total Reflection – Fourier Transform Infrared (ATR-FTIR) spectroscopy. Local changes in the IR absorption spectra were monitored using IR microscopy. Coating surface topographical changes were monitored using white light interference microscopy (WLIM). Changes in the mechanical response were monitored using nanoindentation techniques. Changes in the through thickness acoustic properties were monitored using scanning acoustic microscopy (SAM).

4.2.2 Results and Conclusions

Degradation in the polymer chemical structure due to weathering was successfully characterized using ATR-FTIR. A continuous decrease in absorption peak height and area correlated well with increasing coating exposure time (Figure 4.2.2-1). Local measurements of the IR absorption spectra using the IR microscope attachment showed higher peak amplitudes than those obtained using ATR. The source of increased sensitivity with the IR microscope may be explained by examining the way the spectra are measured.

Measurements of IR absorption using either method rely on a good optical contact between the coating and measurement crystal. The ATR crystal is approximately 1×3 cm^2, whereas, the diamond-shaped IR crystal is ≈ 50 µm in diameter. The large flat contact surface for the ATR crystal results in a reduction in IR absorption for any increase in coating surface irregularity or stiffness. Therefore, higher peak amplitudes from the IR microscope indicated that the attenuation in the ATR spectra might be due in part to degradation in the optical contact between the ATR crystal and epoxy coating. Nevertheless, degradation in the optical contact between the crystal and coating surface indicates that a change in the physical and mechanical properties of the polymer surface occurred during weathering that can then be correlated with chemical property changes.
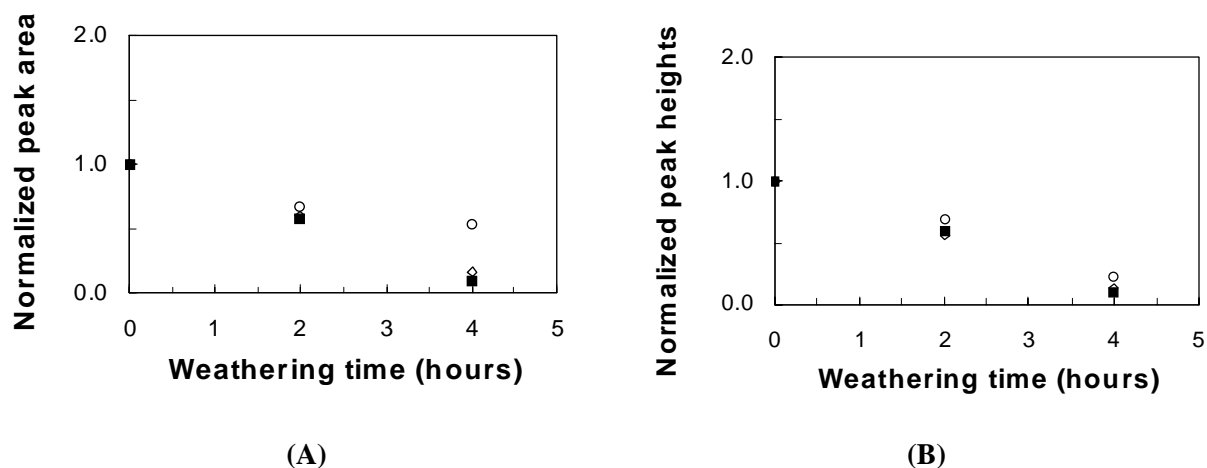
Figure 4.2.2-1: Changes in peak (a) area and (b) height as a function of weathering time for the IR absorption peak at 1509 cm^{-1}.

Characterization of the surface topography using WLIM revealed a cell pattern on the coating surface that may have been formed in the coating during the cure. A comparison of the topographical images from the unexposed and weathered coatings showed that, after weathering, the cell structure continued to dominate the topography. However, the local height variations showed some differences after weathering (Figure 4.2.2-2).

Prior to weathering, the height variation was approximately 600 nm. In contrast, after weathering, the height variation was somewhat lower, approximately 200 nm. Details of a fine structure between the larger cells were also detected in the WLIM images. Additional images acquired using Atomic Force Microscopy (AFM) showed a similar cell pattern, but did not show the fine structure of the topography between larger cells.

(a)   (b)
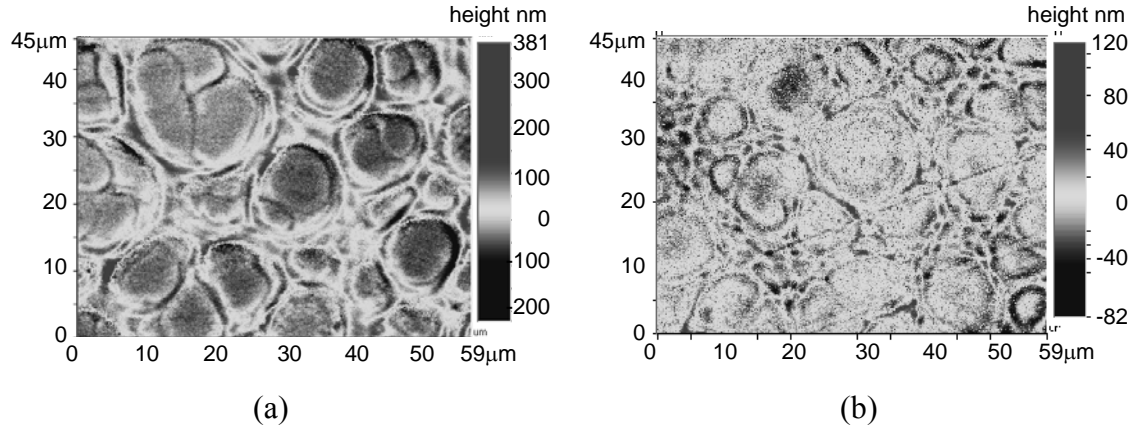
Figure 4.2.2-2. Epoxy coated panels imaged using WLIM: top surface reflection of coating (a) prior to weathering and (b) after 24 hours weathering (magnification 105.3×). The contrast has been enhanced in the images to clarify the topographical features.

Changes in the elastic response of the very near surface region (to a depth of 2 μm) of the coating were measured using nanoindentation. The plot in Figure 4.2.2-3b shows that a slight increase in elastic modulus occurred after 24 hours of weathering. The values plotted in Figure 4.2.2-3b were calculated from the nanoindentation data. In contrast to the near surface properties measured using nanoindentation, acoustic microscopy was used to obtain a measure of the average mechanical properties through the coating thickness. By measuring the amplitude of the acoustic wave reflected from the substrate, information on the variation in coating density and elastic modulus can be obtained. The A-scans show reduced reflectivity amplitudes for the degraded epoxy coating (Figure 4.2.2-4). This corresponds to an overall softening of the polymer due to destruction of the epoxy binder structure. A softening of the epoxy coating is in apparent contrast to the slight increase in elastic modulus with weathering time indicated by the nanoindentation results discussed previously. The differences in elastic behavior measured by the two approaches

may be due to differences in coating depths that were interrogated by each technique. The nanoindentation results are highly localized at the coating surface, while the SAM measurements are based on a through-thickness measurement of reflected amplitude. The differences in the results may further indicate a failure mode induced by a large gradient in the elastic properties through the thickness of the coating, thus resulting in internal stresses that ultimately lead to cracking.
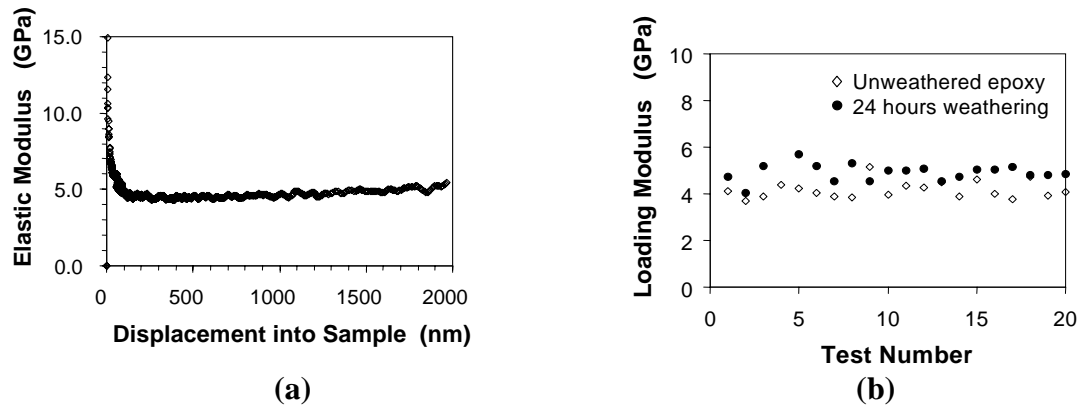
Figure 4.2.2-3. Elastic modulus measured using nanoindentation (a) as a function of penetration depth and (b) average loading modulus for unweathered coatings and after 24 hours of weathering.

The research performed under this effort showed that the methods used were applicable for characterization of coating degradation during weathering exposures. However, to use these techniques to effectively monitor coating degradation, a complete assessment of the variability in the measurements due to normal material variability must be performed. An extensive evaluation of the variability in elastic properties using nanoindentation was initiated to determine if the changes in elastic modulus observed during weathering are within the normal variability of the panel. Similarly, correlations among the changes in surface condition and the IR absorption and acoustic properties and as-processed coating properties must be established before these techniques can be used as robust NDE approach for monitoring degradation in polymeric protective coatings.
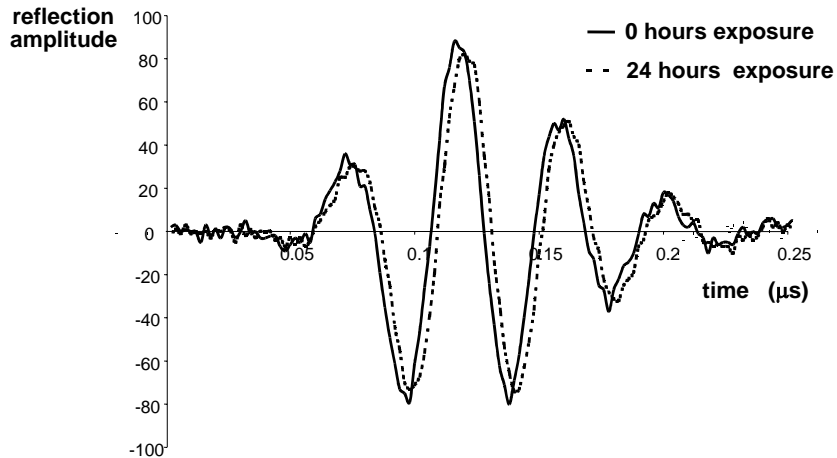
Figure 4.2.2-4. Acoustic response with and without weathering exposure. A-scans of 25 μm thick epoxy coating.

4.2.3   For Additional Information

For additional details please see the articles titled: "Characterization of Weathering Degradation in Aircraft Polymeric Coatings Using NDE Imaging Techniques" and "Characterization of Weathering Degradation in Aircraft Polymeric Coatings Using NDE and Microscopic Imaging Techniques". These articles are included in Appendix A.

4.3   Corrosion and Fatigue Studies on Aluminum and Titanium Alloys

4.3.1   Introduction

During his graduate studies in pursuit of a Masters Degree in Materials Engineering at the University of Dayton, Mr. Chris Kacmar conducted an experimental project to provide information about fatigue cracks that originated from a variety of sources. These sources studied were corrosion damage, notch damage, treated damage, and undamaged specimens of aluminum and titanium alloys. The project included the optimization of the electrochemical corrosion pitting process for creating cracks of desired depths, the effects of different pitting parameters on fatigue life, the use of a new nondestructive technique, Near-Field Scanning Interferometry (NFSI) for detecting crack initiation and monitoring crack growth, and the effects of laser treatment of damage on the fatigue life of the material. Pit parameters were measured using a White Light Interferometetric Measurement (WLIM) system.

4.3.2   Approach

Four major objectives were established to help guide the experimental efforts. The four major objectives were:

1. Determine how electrochemical parameters can be altered to produce predictable amounts of corrosion damage.

2. Determine what corrosion pitting parameters (e.g. depth, width, volume, etc.) can be correlated with fatigue life.

3. Monitor fatigue crack initiation and growth originating from a corrosion pit using a Near-Field Scanning Interferometry.

4. Determine what effect laser treatment of the material's damaged area has on its fatigue life.

Objective one was necessary for creating pits with the characteristics required by objectives two and three. Objectives two and three involved fundamental research projects that were necessary for understanding the intricate relationship between two complex, material-degrading mechanisms. Objective four was undertaken to determine whether or not the fatigue life of specimens with pre-existing damage could be extended by special treatments.

4.3.3   Conclusions from the Project:

1. No correlation was found between any of the corrosion pit parameters studied (depth, width, volume, etc.) and fatigue life.

2. NFSI is a valuable tool for future work in the characterization of micron-sized fatigue cracks. Use of NFSI allows cracks to be monitored from approximately 50% of a specimen's fatigue life.

3. It was found that, in some cases, the laser treatment extended the fatigue life of the specimens and, in other cases, it reduced the fatigue life. There was a difference in the effect that the laser treatment had on the two types of materials, with the aluminum specimens having more-significant cracking problems after the laser treatment than did the titanium specimens.

4. An exponential relationship between the corrosion pit depth and the amount of electrical charge used for the creation of the pit was observed. The results demonstrated that increases in exposure time created corrosion pits of greater depth.

5. The results of this study should be considered to be preliminary. More extensive tests are required for understanding the mechanisms behind crack initiation/growth, laser treatment and corrosion creation.

4.3.4 For Additional Information

For detailed information about this project please see the report titled "Corrosion and Fatigue Studies on Aluminum and Titanium Alloys" in Appendix B.

4.4 Three-Dimensional Corrosion-Growth Monitoring

4.4.1 Air Force Need

Many studies of corrosion growth are one-dimensional in nature. However, corrosion growth, especially intergranular corrosion, is three-dimensional. Therefore, UDRI and ARACOR initiated a study to monitor three-dimensional corrosion growth in aerospace materials.

4.4.2 Technical Approach

ARACOR and UDRI conducted a small study to determine the capabilities of the AFRL/MLLP branch's Tomoscope x-ray CT system for monitoring the three-dimensional growth of intergranular corrosion. For this effort, intergranular corrosion was grown at an accelerated rate in a 6.35 mm (0.25 inch) diameter cylindrical rod of 2024 T4 aluminum. The corrosion was grown by applying a constant potential voltage to the rod that was immersed in a solution of sodium chloride, copper chloride and acetic acid. The corrosion-growth setup is shown in Figure 4.4.2-1. The specimen was corroded for a total of three corrosion-growth exposures at 48 hours per exposure. X-ray CT slice images were made at depths of 0.4 mm, 0.75 mm, 1.10 mm and 1.45 mm after each 48-hour corrosion-growth period.

Figure 4.4.2-1. Corrosion-growth setup.

In addition to the x-ray CT examinations, a series of acoustic-microscope C-scans were conducted in planes parallel to the axis of the cylindrical rod specimen. The C-scan data were acquired at 20-μm lateral intervals using a transducer with a 5.08 mm focal length and a 32 MHz center frequency. That data were acquired at depths of 0.0064 mm, 0.0127 mm, 0.190 mm, and 0.254 mm parallel to the axis of the cylinder.

4.4.3   Results

Figure 4.4.3-1 shows four CT slice images at different depths into the material after the first 48 hours of corrosion exposure and four CT slice images at the same depths after 96 hours of corrosion exposure. It is evident from the images in Figure 4.4.3-1 that very little additional corrosion growth occurred after the first 48-hour exposure period. It appears that an oxidation layer was built up at the corrosion site when the corrosion growth was stopped after the first 48-hour period, and that this oxidation layer severely retarded subsequent corrosion growth.

The ultrasonic approach was less successful than the x-ray CT approach. The shadow of the corrosion on the top surface of the specimen appeared in all subsequent

layers and masked the existence of any corrosion at greater depths. Only the C-scan image acquired at the 0.190 mm depth indicated possible further corrosion growth.

| Corrosion after 48 hr at 0.4 mm depth | Corrosion after 48 hr at 0.75 mm depth | Corrosion after 48 hr at 1.10 mm depth | Corrosion after 48 h at 1.45 mm depth |
| Corrosion after 96 hr at 0.4 mm depth | Corrosion after 96 hr at 0.75 mm depth | Corrosion after 96 hr at 1.10 mm depth | Corrosion after 96 h at 1.45 mm depth |
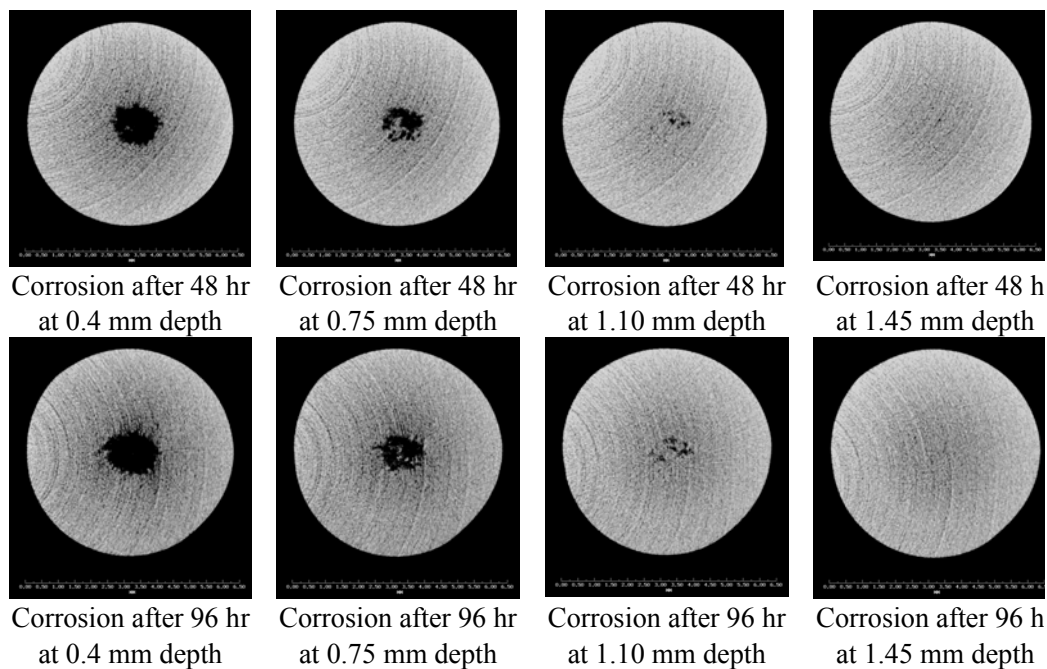
Figure 4.4.3-1. X-ray computed tomography slice images of corrosion growth at different depths in 2024 T4 aluminum.

A presentation – "NDE for Corrosion Growth Rate in Aluminum" – that described the results of this effort was made by Dr. Claudia Kropas-Hughes (a civilian employee of AFRL/MLLP) at the ASNT Spring Conference, March 10-13, 2003. That presentation was co-authored by Dr. Kropas-Hughes, Dr. Shamachary Sathish (AFRL), C. Dan Daniels (ARACOR), and Dr. Mohammad Khobaib, Mr. Edward L. Klosterman, Mr. Richard Martin, and Mr. Richard Reibel (UDRI). This presentation is not included in this document.

4.5   Operability of the Honeywell Corrosion Environment Monitor System (CEM)

UDRI tested a Honeywell-developed, five-sensor Corrosion Environment Monitor (CEM) system. The system was designed by Honeywell at the request of the Air Force to monitor and record corrosion-related environmental conditions during operation of Air Force aircraft. The CEM that UDRI tested was also used to record environmental data obtained from the wheel well of an operational C-141 aircraft. The research and tests conducted by UDRI are provided in Table 4.5-1.

Table 4.5-1 UDRI Research and Tests on the Honeywell CEM

1. Determine the rated operational environment specifications for the probes and electronics of this system that will define the environmental limitations of the complete system.
2. Check the calibration of the five sensors in the laboratory at about 25 °C.
3. Check the operation and accuracy of the sensors in the laboratory with environmental changes that simulate in-flight conditions.
4. Analyze environmental data that was recorded by the CEM while installed on a C-141 aircraft.

4.5.1   Main Features of the CEM

The Honeywell CEM system consists of two main components: (1) a sensor unit that records six corrosion-environment-related parameters at equal time intervals, and (2) a long-term battery-operated data recorder that stores data on a PCMCIA card. The six parameters that can be stored are: (1) temperature, (2) humidity, (3) PH, (4) free potential voltage from a corrosion cell, (5) CL-, and (6) battery voltage of the CEM recorder power supply. The system includes a read-out program for a host computer, and all data can be analyzed with Microsoft Excel.

4.5.2   Test Procedure

Prior to establishing a test procedure, it was necessary to determine the safe operating temperature and relative humidity ranges for the sensors, cable, and data recorder. After establishing those ranges, the test procedure outlined in Table 4.5.2-1 was designed.

Table 4.5.2-1 – CEM Sensor and Recorder Test Procedure

1. Operate the CEM recorder at the fastest data acquisition rate of one sample per minute for all of the tests.
2. Verify the calibrations of all sensors at 25°C.
3. Conduct a temperature-humidity profile study of the operation of all sensors to cover the ranges of 10% to 95% RH at temperatures between 5 and 60°C. Dwell at each setting for chamber and CEM recorder stabilization.
4. Conduct a temperature-only profile of the operation of all sensors to cover the range of -30°C to +60°C.
5. Conduct a PH sensor test with solutions measured with a calibrated PH meter from 2 to 10.
6. Conduct a Cl test with solutions measured using a calibrated Cl meter. From the results of this test, create a voltage versus Cl-level calibration chart.
7. Create conversion charts of voltage output versus measurement units for the PH-, Corrosion cell, and Cl- sensors.

4.5.3 <u>Results</u>

The experiments for exposing the five CEM sensors to different temperatures, liquids, and humidity levels were completed. These tests included various humidity levels from 10 to 100% and various NaCl-water-solution concentrations. The liquid experiments were performed at approximately 25°C. The resulting data records were analyzed and plotted. The CEM data for temperature was in error by -1.8 to -4.1°C, from 0°C to 60°C. The relative humidity was in error by +4.9% to +14.3%, from 2 to 100% RH. The pH, chlorine ion, and corrosion cell probes had no calibration tables supplied, and the data was recorded in volts only. Therefore, calibration tables, graphs, and equations to convert these voltages to meaningful measurement units were created.

The Honeywell CEM calibration tests were completed for the temperature and humidity sensors that were used in the C-141 wheel well test. Analysis of the data record showed the temperature probe saturates near minus 18°C. No temperature changes were recorded below this temperature. The calibration error for the temperature probe was nearly constant from -10°C to +60°C. The offset of the temperature sensor data record was approximately four degrees below the actual temperature. The calibration error for the relative humidity probe was plus 6% at 4% relative humidity. This error increased with increasing humidity to plus 19% at 90% RH, which produced a data record value of 109% RH. Any relative humidity levels above 82% that were recorded by the CEM produced values over the physical limit of 100%. The maximum humidity obtained in the environmental test-chamber measured 99.7% with a calibrated humidity probe and this level produced a CEM data record value of 121%.

Data were analyzed from the CEMs mounted in the wheel well of an operational Air Force C-141 aircraft. The temperature, humidity, and pH data showed the diurnal cycles. They also recorded low temperatures and very low humidity at high altitudes. The chlorine ion and corrosion cell indicated damp corrosive environments for longer time periods then did the humidity sensor. The maximum RH recorded from a CEM mounted in a C-141 wheel well was 133%; that probably occurred when moisture had condensed on the probe. This event occurred three times in the data record; each time,

it was within an hour after the flight. Most occurrences of humidity greater than 100% occurred just after flights.

Surface contaminants were deposited on the cases of the CEMs while they were mounted in the wheel well of an operational C-141. The identification of these contaminants was accomplished by ChemSys Inc. No water-soluble contaminates that could affect pH were found. The PH level of the test rinse water was the same before and after rinsing the CEM cases. The elements found in the surface contamination were as follows: major (>10%) Ca, Si, Fe; minor (1-10%) Al, Zn; with traces (<1%) K, Ti, and Cu. The main compounds identified by microscope based FTIR were calcium carbonate and inorganic silicates. Other compounds in the contamination were aliphatic hydrocarbons, and a grease-like hydrogen-ester that also contained inorganic silicate and carbonate compounds. Some of these compounds might affect the sensor calibrations and sensor insulation resistance.

4.5.4   Reports and Presentations

The results of this effort were presented as PowerPoint slides to AFRL/MLLP on April 3, 2002. A draft report that described the project and the results obtained was written and provided to the appropriate AFRL/MLLP personnel.

4.6   Corrosion Detection and Quantification Capabilities of SAIC Systems

The Air Force's pressing current needs for nondestructive detection and quantification of hidden corrosion in its fleet necessitates not only the evaluation of techniques that may be used in future years, but also the capabilities and limitations of currently-available depot-applicable techniques. For that reason, the hidden-corrosion detection and quantification capabilities of SAIC's Ultra Image IV with eddy current and ACES™ ultrasound were evaluated using funding from this contract. These systems were evaluated using a probability of detection (POD) methodology for percent material loss that is similar to well-established crack-detection methods. All of the evaluations of SAIC's eddy-current and ultrasonic systems were performed off site; none were performed within AFRL/ML.

A combination of real aircraft lap joints and doublers believed to have areas with and without corrosion and specially-designed engineered specimens were chosen for the

evaluation and incorporated into the test matrix. A measurement of the spatial resolution of each system was made in the first test. Although this aspect is not inherent to the analysis, inspection outputs are potentially influenced by features of a lap joint or doubler. A test of both the edge and fastener effects was implemented to determine the size of the area or zones affected so that they could be eliminated from the analysis. The POD determination required inspection information on both corroded and non-corroded structures. Tests were established on four-layer lap joints, two-layer lap joints, and two-layer doublers in both corroded and non-corroded aircraft specimens. There also were tests designed for POD using corroded and non-corroded structures with different top skin layer thicknesses.

4.6.1   SAIC Ultra Image IV with Eddy Current

SAIC's eddy-current system is a conventional fixed-frequency technique using a commercially-available eddy-current instrument and probe. For application on aircraft, the probe is mounted in a gimbaled holder and attached to the ultra Image IV ruggedized, automated X-Y scanner.

This system employs a conventional single-frequency eddy current technique. Changes in amplitude reflect changes in top skin thickness, gap, and liftoff. A Nortec 2000 eddy current instrument was used to perform eddy current inspections, with the eddy current output fed into the external input of the SAIC instrumentation unit. The frequencies selected for the test were based on one skin thickness equal to the top layer thickness using a conductivity of the specimens of 34% International Annealed Copper Standard (IACS). Rounded to the nearest kilohertz, this works out to 5 kHz for 63-mil cases and 12 kHz for 40-mil cases.

The evaluation data showed a clear correlation between thickness loss and eddy current output. This system was found to have a spatial resolution of 0.34 inches. Fastener zones were estimated at 0.56 inches for this system. Trial POD test results show a clear trend in the data, with fair discrimination and a relatively low signal-to-noise ratio at the calculated threshold. Evidence of corrosion detection was apparent in the image of corroded aircraft specimens, whereas, the aircraft specimen with no corrosion looked clean, as expected. Inspection output for this technique was converted to voltage and was

used in an "a-hat vs. a" analysis. A threshold was selected to produce a 90% POD at 6% thickness loss. With this threshold, the 50% POD corresponded to 5.2% thickness loss. Since low levels of corrosion are not detected, this system was judged to have excellent discrimination capability. Also, the threshold was well above the noise, making this system relatively insensitive to false calls. In summary, this technology has good sensitivity to thickness loss, good spatial resolution, excellent discrimination, and excellent signal-to-noise on the four-layer lap joint aircraft specimen.

Advantages of this eddy current method include that it is sensitive to the top layer thickness. It is a relatively-rapid scanning technology, with thirteen scans completed during the test. The output is a digital image, which allows for convenient data archival and processing. The technique could be used with a crawler or other automated system.

The system did have a few problems. For instance, protruding rivets obstruct the probe motion. Pad wear during use is also a problem for the system. And, the use of a single frequency during the evaluation did not allow for differentiation between changes in top-layer thickness and the presence of a gap between layers; so, calibration was performed on single layers.

Future developments proposed by SAIC include implementing dual-frequency techniques for multi-layer inspection and redesigning probe holders to increase service life. The addition of a rotary scanning head to accommodate fastener-hole inspection using conventional and phased array probes is also proposed.

4.6.2 SAIC Ultra Image IV with ACES™ Ultrasound

SAIC's ultrasonic system implements a conventional pulse-echo immersion technique with a high-frequency (HF), broadband, focused probe. The probe is an integral part of SAIC's ACES™ scanning head that is affixed to the Ultra Image IV automated X-Y scanner for on-aircraft inspections.

This system uses conventional high-frequency ultrasound with a novel water couplant recirculation device, which makes immersion pulse-echo techniques with focused transducers possible. This technique is sensitive to top layer thickness. It makes use of an automated X-Y scanning system. One of the main features of the SAIC system is the

ability to perform "immersion" inspections on the side of an aircraft using their ACES (Automatic Couplant Ejection System) transducer holder. ACES is a "dripless bubbler" unit made of concentric ovals of brushes that are used to supply water and capture it again for recirculation. Inclusion of a vacuum system in the ACES leaves the surface of the specimen practically dry to the touch after scanning.

The SAIC ultrasonic system employs immersion pulse-echo focused ultrasound to do time-of-flight measurements of the front surface thickness. A clear correlation to actual thickness loss is depicted in correlation data. Resolution was estimated at 0.07 inches, with the cell size chosen at 0.11 inches. The fastener zone was determined to be 0.40 inches. Inspection output for the POD tests were converted to thickness, from which thickness loss was calculated using the maximum measured thickness from specimen characterization as a reference. Tests of "a-hat vs. a" analysis assumptions revealed that this data did not pass the normality assumption due to the discrete nature of the data. The output was limited to discrete values by the sampling rate of the ultrasonic digitizer (100 MHz). Since the POD generated with this data using an "a-hat vs. a" analysis would be inaccurate, a pass/fail analysis method was employed. Due to the discrete nature of the data, it was not possible to set a threshold to achieve a 90% POD at 6% thickness loss, so a threshold was selected at 5.6% thickness loss for four-layer lap joint inspection. This threshold was above the noise, but not appreciably.

Images of an engineered, simulated corrosion specimen indicate sensitivity to thickness loss in this 0.040 inch top skin thickness specimen, with poor discrimination (seen in the detection probabilities for lower levels of corrosion), and a poor signal-to-noise ratio at the corresponding threshold.

Enhanced inspection images show evidence of corrosion in the corroded aircraft specimen; the uncorroded aircraft specimen inspection was clean. Discrimination was moderately good, evidenced by a gradual dropoff in POD at the smaller percent thickness losses. The 50% POD was found to be at 4.1% thickness loss. As mentioned previously, the threshold was not appreciably above the noise floor, suggesting that this system is susceptible to false calls. This system does not discriminate between low levels and high levels of thickness loss as well as the eddy current systems do. In summary, for the four-

layer lap joint region, this ultrasonic technology has good sensitivity to thickness loss, excellent spatial resolution, good discrimination capability, and a fair signal-to-noise ratio.

This system has several advantages. It scans relatively rapidly. The ACES unit leaves the scan surface dry and can ride over protruding rivets unlike the other contact techniques. The output is in the form of a digital image, which allows for convenient data processing and archiving. This technique could be used with a crawler type automated scanner.

Some issues were encountered with the use of the ACES scanner head during the evaluation. It was designed for angled transducers for use on an aircraft wing, but was used during evaluation with a vertically-oriented, focused transducer, which became a natural trap for bubbles. Air entering the ACES head was also a problem near lap joint edges. Consequently, it was necessary to place aluminum shims adjacent to lap joints with tape covering the gap to avoid pulling bubbles into the system. The rigid scanner used for the evaluation is heavy and would require multiple people to move and operate. SAIC has proposed several further developments of this system, including a redesign of the ACES head to accommodate scans on the fuselage sections and to remove trapped bubbles. They also propose to add a 360-degree rotary head for inspection around fasteners using conventional and phased array probes.

4.6.3   For Additional Information

For detailed information about the procedures used for data collection and evaluation, the results obtained, and the conclusions reached from analyses of the data, please see the report titled: "Automated Corrosion Detection Program – Final Report", AFRL-ML-TR-2001-4162, authored by Mr. Wally Hoppe, Ms. Jennifer Pierce and Ms. Ollie Scott, all of whom were UDRI employees at the time-of-writing of that report. Due to size, that report is not included in Appendix A, but can be obtained from UDRI or from AFRL/MLLP. Much of the material for the above SAIC description was extracted from this report.

Section 5
Vehicle Health Monitoring (VHM)

5.0   Self-Power Generation for In-Flight Ultrasonic NDE

UDRI is developing a system that will generate power from in-flight aircraft structural vibrations for transmitting, receiving, and storing ultrasonic data. The data could be used for detecting fatigue cracks and monitoring their growth, which is of vital importance given that the Air Force is extending the use of aircraft beyond their design lifetimes.

5.0.1   Requirements

The system needs to operate with a minimum of components, very few wires, and no battery or external power. The current and voltage levels generated by in-flight structural vibrations will be very low, so a charge-discharge circuit that will provide power using only low-power electronic elements is required. This circuit must have high impedance and low-frequency response, which is very difficult to achieve simultaneously.

5.0.2   The Approach

A parallel developmental approach was chosen for this effort. The approach consists of developing and testing some potential self-power generation systems, while simultaneously attempting to acquire information about the frequencies and amplitudes of vibration resonances that are generated by in-flight aircraft.

For self-power generation, a piezoelectric transducer is being investigated for conversion of mechanical energy from structural vibrations to electrical energy. An electronic circuit consisting of a diode, an RF step-up transformer, a silver mica capacitor, and a tantalum capacitor was constructed to increase the voltage level from the piezoelectric transducer and store it for future use in the ultrasonic NDE system. The small silver mica capacitor works with the step-up transformer to form a tuned LC oscillator that resonates at about 62 KHz. The diode rectifies the 62 KHz AC voltage to a DC voltage that is then stored in the tantalum capacitor.

5.0.3 Tests and Results

Structural vibrations were first simulated by an ultrasonic cleaning tank. Using the ultrasonic cleaning tank, the voltage stored by the electrical system sometimes reached 12 volts DC.

The 12-volt DC level described in the previous paragraph was achieved because the ultrasonic cleaning tank had a strong resonance near the 62 KHz resonance of the electrical circuit. However, it is unlikely that aircraft structural resonances would occur at frequencies above 1 KHz. Therefore, a new circuit was designed to produce 1 to 10 volts at resonances of approximately 50 Hz and 320 Hz. This new circuit was tested with a mechanical shaker as the vibration source. At 50 Hz and 320 Hz, the new circuit produced a maximum of 10 volts DC, and less than 0.5 volt DC at other frequencies.

In the actual self-powered application, consistent and stable voltage levels need to be produced over a wide range of vibration frequencies. Using a very low-power single-chip DC-to-DC converter, any input voltage in the range of 2 to 12 volts may be stepped-up to 12 volts reliably. However, the amount of current used by the converter is a concern. Other converters have been tested and are capable of increasing 3V to a level of 24V, but the power usage by these converters is too great. The search for lower-power versions continues.

A number of circuits that may be used to discharge a charged capacitor into a piezo-electric transmitter element (spike pulse) have been investigated. These have included avalanche diodes, SCR's, Triacs, Diacs, and Bilateral Trigger Diacs. All of these devices work well if the power consumption of the device (or its associated circuitry) is ignored. So far, the power consumption is too high and only a very small amount of the power would be transmitted. UDRI has asked three semiconductor companies to offer their suggestions.

5.0.4 Conclusions

More electrical circuits must be designed and tested, and additional information about the frequencies and amplitudes of actual aircraft structural vibrations must be obtained before a self-power generation system can be tested on operational aircraft.

5.1   Sensing Technology for *In Situ* Health Monitoring of Gas Turbine Engine Blades Feasibility Study

5.1.1   Air Force Need

Gas turbine engines are subject to a variety of problems, such as crack initiation and growth, protective coating failure, foreign object damage, non-uniform air flow, blade vibration modes, etc. Real-time, nondestructive measurements of some of these conditions could provide data to better diagnose operation problems, verify and/or improve analytical models of engine performance, and material/structural data for component designers.

5.1.2   Technical Approach

The research performed under this program examined the feasibility of using surface acoustic waves (SAW) to measure the vibration modes and frequencies that are experienced by blades on rotating engine components. The technique used the SAW transducers in a pitch-catch mode with the transmitter sending a 5 MHz continuous wave to the receiver. The phase of this continuous acoustic wave was sensitive to modulation by strain in the section of the test article between the transducers. As strain was induced in the test article, the distance between the transmitter and receiver changed, changing the differential phase that was measured between the transmitting and receiving SAW transducers. In order to induce uniform strain and stress over a significant distance in the test article, a four-point bend fixture was used to create a uniform bending moment between the loading points. A steel bar, 12.7 mm thick and 50.8 mm wide was used for this testing. Strain data were acquired at various points in the center section of the bar to insure that there was a uniform strain field in the region of interest.

5.1.3   Results

Analysis of the four-point bend data demonstrated that a linear relationship exists between the measured phase of the surface acoustic wave and the material strain. This is shown in Figure 5.1.3-1.
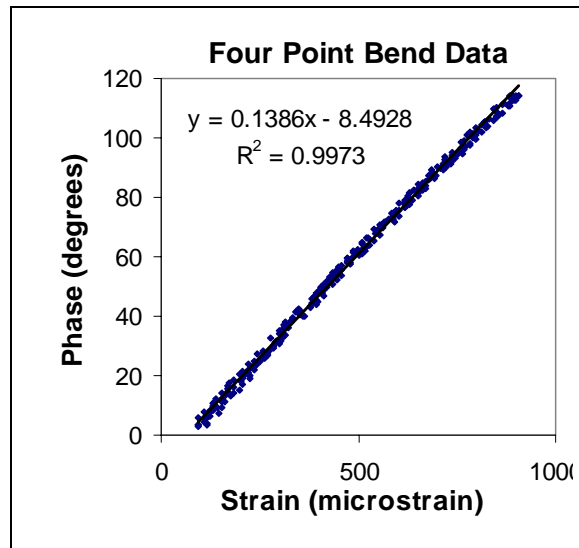
Figure 5.1.3-1. Phase vs. strain relationship.

5.1.4   <u>For Additional Information</u>

Additional details of this effort can be found in Appendix A in the article titled "Strain Measurement Using Surface Acoustic Waves". This effort was performed with AFRL/ML Director's Funds that were added to this contract.

Section 6
Special Projects

6.0   Introduction

In addition to the large projects conducted during the contractual period-of-performance (i.e., residual stress measurement, corrosion-related research, and vehicle health monitoring), several smaller but significant projects were also executed. These included: (1) a largely theoretical study of the feasibility of using acoustic emission techniques for monitoring certain metal processes, (2) an experimental x-ray-computed tomography technique for characterizing particulate-matter distribution in metal-matrix composites, and (3) several Collaborative Technology Clusters (CTeC) efforts. There were also numerous short service-type projects; these are listed and very briefly described in Table 6.5-1.

**6.1   Feasibility of Using Acoustic Emission Techniques for Monitoring
          Metal Processing**

Bulk metal working causes significant changes in both the microstructure and the shape of a material. Macro-scale defects that may result from metal-working processes can usually be detected by conventional NDE techniques. However, defects at the micro-structural level (which can also cause failures during service) often go undetected by conventional NDE techniques. In-service failures present a safety hazard, and they can result in very high maintenance and replacement costs. Even detectable macro-scale defects can significantly increase the cost of manufacture because of the investment in manufacturing the part that occurs prior to detection of the defect. This is particularly true of aerospace components because of their high manufacturing costs and stringent quality requirements. Thus, the development of an on-line, non-destructive technique for detecting the formation of defects (micro and macro) very early in the metal-working process could significantly reduce costs to the Air Force.

6.1.1   Selection of Dr. Prasad

UDRI did not have any scientist or engineer on staff with sufficient experience and knowledge in this field to conduct meaningful research for AFRL/MLLP. Therefore, Dr. Yellapregada Prasad, a world expert in the field, was hired as a consultant for the

effort. Dr. Prasad, a citizen of India, worked on the UD campus for the entire term of his contractual effort.

6.1.2 Goal and Approach

The goal of this project was to explore and identify an NDE method that would detect the macro and micro defects during metal-working processes, preferably on-line. Dr. Prasad undertook an extensive and intensive literature review to accomplish this goal. During the first phase of this review, he identified acoustic emission as the most likely candidate for accomplishing the goal. During the second phase of his literature-review efforts, he focused on the following two tasks:

- Determining the feasibility of using acoustic emission for monitoring microstructural evolution during hot working with particular emphasis on detecting microstructural defects, and

- Determining the applicability of the acoustic emission technique for detecting process-related problems – such as those caused by die failure, material flow, and friction – on the basis of general theoretical considerations and experimental results from the literature.

6.1.3 Conclusions from the Study

- Acoustic emission has a very high potential as an NDE technique for monitoring metalworking processes.

- There is considerable evidence already available that substantiates the usefulness of acoustic emission for detecting macro defects, cracking, and lubrication failure in processing.

- Important micro-structural defects such as void formation at hard particles, wedge cracking, and flow localization can be detected with acoustic emission.

- Micro-structural mechanisms involved in "safe" hot working are essentially "quiet" processes and generate little acoustic emission, even compared to plastic deformation caused by dislocation avalanche. Therefore, any acoustic emission generated during hot working indicates the formation of a defect or defects.

- Further research is required at three levels to develop acoustic emission into a viable industrial tool for monitoring metal processing. These steps are:
  - Fundamentally characterize the acoustic emission signals from micro-structural processes in their deterministic domains on carefully selected materials.

- Validate the modeling results with the help of controlled experiments on laboratory-scale manufacturing processes such as superplastic forming, drop forging, and extrusion. This must be supported by finite element simulation modeling of the process.

- Develop an acoustic emission system – on the basis of the results from fundamental characterization and model validation studies – so that it is suitable for an industrial environment where several of the previously-listed defects must be detected when they occur simultaneously.

6.1.4 For Additional Details

In-depth details of Dr. Prasad's work can be found his report titled, "Feasibility of Using Acoustic Emission Techniques for Monitoring Metal Processing". That report is included in Appendix B.

6.2 Eddy-Current Characterization of Cracks Around Fasteners in Multi-Layer Structures

6.2.1 Air Force Need

Operator interpretation of eddy-current NDE data is often subjective and variable. This subjectivity and variability can lead to unnecessary replacements and repairs, as well as the postponement of repairs and replacements when they are necessary. For these reasons, the Air Force needs methods to automate the detection and characterizations of eddy-current data.

6.2.2 Potential Solution

Dr. Claudia Kropas-Hughes, a civilian employee of AFRL/MLLP, had developed neural-network methodology that was perceived to be capable of automating the interpretation of eddy-current NDE data. However, implementation of the methodology required data for training the neural-network methodology and for evaluation after training. To fulfill the need for training and evaluation data, UDRI undertook an extensive project to collect eddy-current data for the training and evaluation phases of the neural-network implementation effort.

6.2.3 Approach

Eddy-current C-scan type data was collected from 100 simulated C-5 multi-layer aluminum lap joint specimens with titanium fasteners. The top layer was 4 mm (0.156 in)

thick and the bottom layer was 2.5 mm (0.1 in) thick. Cracks of known length had been intentionally introduced around many of the fasteners. There were cracks in all four layers – top and bottom surfaces of the top layer, and top and bottom surfaces of the bottom layer – but not around the same fastener. Automated eddy-current data-collection scans were conducted using a probe frequency of 600 Hz for cracks on all but the top surface of the top layer. Scans for cracks on the top surface of the top layer were conducted using a probe frequency of 20 kHz.

6.2.4   Results

The data were carefully reviewed and analyzed manually, and compared with the results obtained by other investigators to ensure that the data had been collected correctly. Crack analysis was conducted by viewing the reconstructed impedance plane display around selected fasteners. Cracks of 2.5 mm (0.10 in) and longer were reliably detected on all four surfaces of the lap joints. Smaller cracks were detected in some cases. Cracks on the two faying surfaces – bottom surface of the top layer and top surface of the bottom layer – were detected with the highest reliability because the eddy-current instrument was optimized for crack detection on those surfaces. The data was then provided to Dr. Kropas-Hughes.

6.3   Characterizing Particulate-Matter Distribution in Metal-Matrix Composites

6.3.1   Air Force Need

The Air Force's interest in the use of metal-matrix composites in aircraft structures necessitates improvements in the fabrication processes. Therefore, ARACOR initiated a process-improvement study to explore the feasibility of using x-ray CT to examine the three-dimensional compositional distribution of particulate matter in a particulate-reinforced metal-matrix composite.

6.3.2   Approach

Traditional methods to characterize particulate-reinforced metal-matrix composites suffer from three disadvantages: they are labor intensive, subjective in nature, and destructive. Consequently, process design and control strategies for this class of materials are slow and often relegated to trial and error. A more-robust means of characterizing the internal distribution as a function of processing variables would allow materials designers to engineer these composites to match specific mechanical requirements.

73

By combining high-resolution x-ray CT with the established science of geostatistics, ARACOR endeavored to describe the spatial distribution of the particulate phase within a given metal matrix. Such a methodology, if successful, would provide a critical link between the processing variables and final mechanical properties of these materials.

The material chosen to explore this analytical technique was a novel composite of aluminum and fly-ash particulate matter. This new material possesses many improved mechanical properties over monolithic aluminum, in addition to offering the benefit of energy and waste material savings during processing. However, the distribution of the ceramic particulate undoubtedly plays a key roll in establishing its mechanical properties. Also, current processing techniques are known to generate widely-fluctuating spatial variations of the fly ash in the aluminum matrix.

The original scope of the project called for an analysis of two separate samples of the fly ash composite. It was hoped that samples with similar bulk contents of fly ash, but with different processing histories, could be compared against one another. In this way, the effectiveness of ARACOR's proposed technique as a quantitative process development tool could be evaluated. However, only one specimen of the composite was obtained for the study. As a result, no process comparison could be made from data collected during this study. Instead, the single specimen was used to benchmark the effectiveness of CT to detect the fly ash particulate matter and to compare variogram analysis with more simple statistical methods for image reduction, e.g., using the mean and standard deviation.

6.3.3 Results

ARACOR's results demonstrate that the CT approach can identify both the fly ash particles and the porosity that are present in the sample volume. The results of semivariogram analysis of CT slices show qualitative agreement with CT image analysis of fly ash and porosity clustering as a function of sample depth. The semivariogram was therefore shown to be an effective spatial-statistics analysis tool for data reduction.

6.3.4 For Additional Information

A separate report titled "The 3D Compositional Distribution of Particulate Reinforced Composites: A Novel NDE Protocol" is provided in Appendix B.

6.4   Collaborative Technology Clusters (CTeC) Studies

The CTeC program was a collaborative effort between the State of Ohio's Edison Materials Technology Center (EMTEC) and AFRL/ML. UDRI's On-Site NDE contract in AFRL/MLLP was one of the contractual efforts that participated in the CTeC program. The main objective of the program was to allow businesses – particularly small businesses that were headquartered in Ohio – access to excellent research facilities for studies that would enhance their chances for development of profitable products. The projects undertaken during the time period that the CTeC program was operative are listed below.

- X-ray computed tomography examination of high-performance, low-density composite material from a local contractor. Numerous samples were brought into the CT Facility and scanned on both LAM/DE and Tomoscope.

- X-ray CT examination of several drilling core samples brought in by the Ohio Department of Natural Resources. LAM/DE was used to provide characteristic density data on these samples.

- X-ray CT imaging of sand mold/core samples from participating foundries with the objective of providing density data that would allow improvements to be made to the casting processes.

- X-ray CT-Scans on electromagnetic launcher barrels and components made from composite materials. The expectation was to confirm delamination-free manufacture at various stages of the process.

- X-ray CT to help understand the origin of the differences between powder material and laminate properties in magnetic materials. The original project was planned using the Tomoscope. The samples proved to be too large and too dense for the Tomoscope, so LAM/DE was used.

- X-ray diffraction measurements of residual stress in cylindrically-shaped steel rods.

Results from the studies were provided to the sponsoring companies.

6.5   Service Projects

Table 6.5-1 provides a list, along with brief descriptions, of the many very short service-type projects that were conducted during the course of this contractual effort.

Table 6.5-1. Service Projects		
Material/Component	**Objective**	**Results**
C-17 landing gear teeth	Image stress variations in C-17 landing-gear teeth using Rayleigh Surface Waves.	Several areas of high compressive stress were imaged, but these were not in the anticipated locations.
MOSFET power transistor in Predator UAV	Detect and locate depth of voids in MOSFET power transistor.	Acoustic microscope images indicated large voids in the 4th layer of the 6-layer transistor.
Laser-shock-peened leading-edge specimens	Detect and locate delaminations in six laser-shock-peened leading-edge specimens.	High-resolution ultrasonic scans did not detect any delaminations in the specimens.
Fiber-matrix interface	Detect and monitor fiber-matrix interface debonding in composite material.	Shear-wave back-reflectivity imaged the initiation and progression of fiber matrix debonding in an interrupted single-fiber load test
Gallium Arsenide Twist Bond	Detect and locate voids and delaminations.	None found, slight waviness on y-axis scan.
Ti-additive-process plate from MLSA	Detect and locate voids.	One crack found visually and also detected with ultrasonic scan. No other defects found.
Patch on turbine blade	Detect and locate delaminations.	None found.
Shear and cleavage joint specimens	Detect and locate voids and delaminations.	No significant defects found.
Beam patterns of three-element acoustic lens	Detect field strength and focus patterns.	Field intensities and focal plane were imaged.
Laser-shock-peened Ti sample	Detect depth profile of laser shock-peen.	Maximum depth was 17 microns of a repeating sine wave length of 4.8mm.
Adhesive-bonded Al plates, from Scotland	Detect and locate voids and delaminations.	Minor delamination found.
MAUS IV Scanner Arm Attachment Failure	Repair scanner arm for CNN video report at Area C, WPAFB the day of taping.	Re-tightened pulley attachment screw. System worked fine for the Demo.
Aircraft Coatings	To accurately measure the IR radiation and temperature when heating samples on a hot stage.	A thermocouple was first calibrated with a calibration standard meter. This thermocouple was used to calibrate the black body radiator and IR microscope.

Table 6.5-1. Service Projects		
Material/Component	**Objective**	**Results**
High-voltage diode	Examine diode for disbonds and delaminations.	A severe disbond was detected where a large connector attaches to the silicone of the diode. Disbonds were detected in the epoxy encapsulation package
Steel BBs in a small container	Determine if LAM/DE data could be used to locate the centroid of each BB as a first step in a study to verify grain packing and distribution models.	Individual BBs were imaged, but the boundaries were very noisy and not sufficiently well-defined to provide good centroid data for desired packing and distribution modeling data.
Ceramic matrix composite rotors	CRADA effort to develop thick section infiltration capabilities.	CT images and density profiles were provided for research studies to develop thick section infiltration capabilities.
Developmental carbon-carbon heat exchanger material	Determine the utility of CT to investigate the quality of braze in a prototype heat exchanger constructed with carbon-carbon material.	The CT slices proved to be useful in showing overall migration and concentration of the braze material on internal braze planes.
Sand and sand casting material	Continuing effort to find and demonstrate new applications of CT in materials research and to provide data for ongoing studies.	Density gradient and distribution data were provided for casting process improvement and compaction studies, as well as verification of predictive models.
Powdered bronze, sintered zirconia, alumina, and ZnO samples	To measure density gradients resulting from different compaction techniques in an effort to improve materials produced from powder.	Compaction and density gradient and distribution data were provided for research studies relating to the ceramics community.
Metal engine castings	Feasibility study to demonstrate the capability of LAM/DE to measure internal wall thickness of complex castings.	Critical internal wall thicknesses were measured.
Powder metal automotive gears	Feasibility scans to determine capability of CT to reveal manufacturing defects and problem areas in powder metal components before or after sintering.	LAM/DE has insufficient energy and resolution to image the defects that were known to exist in the powder metal gears.
Reusable Solid Rocket Motor (RSRM) nozzle material	Continuing effort to characterize the response of the rocket motor nozzle material to heat provided by the CO_2 lasers in the LHMEL facility.	Density data was provided on all samples scanned.

Table 6.5-1. Service Projects		
Material/Component	**Objective**	**Results**
Radiation detector assembly	Feasibility scans to determine how many detectors can be scanned at once and still provide the required data on seal depth.	The desired measurement of the seal depth was not straightforward from the CT data.
Composite flywheel	To provide a series of scans for use in constructing a 3D density model of the part.	Full volume scan data was provided for constructing a 3D density model.
Alkaline battery cell	To perform feasibility scans to show the utility of CT in making critical density measurements.	The results show a potential alternative to current destructive methods of measuring density gradients within the cathode material.
Teflon cylinder for acoustic tomography study	To provide CT image data for comparison to acoustic tomography data on the same part.	CT image data was provided for comparison to acoustic tomography data on the same part.
Composite cylinders	To examine the uniformity of the composite layers in the cylinders.	The individual layers were just barely resolvable.
Composite material with metal cooling tubes	Investigate the nature and extent of some apparent cracking or separation of composite layers in a sample that had undergone thermal testing.	The metal cooling tubes caused severe artifacts in the LAM/DE CT image obscuring the separation in composite layers.
Carbon composite aircraft brake disks	To obtain density data throughout the disks to help understand and improve the materials manufacturing process.	Many scans were completed for several different companies and organizations. Density data were provided to aid and support research on production densification processes. Most of the scanning was performed under CRADA arrangements
Control valves	Determine if CT examination of good and bad valves could show a definite manufacturing problem that was causing a low yield of good valves.	The CT images showed differences between the good and bad valves, but the differences did not clearly indicate a problem. It turned out that the problem was of a production control nature, since the valves had been manufactured successfully for some time with a much higher yield of good valves
Glass samples	Feasibility study to obtain density data on some cylindrical glass samples to determine if CT could be a useful tool in the production of this material.	For the most part, the samples were very uniform in density. The visible irregularities did not show up in the CT scans as density gradients. Some bubbles or porosity very near one of the ends of the cylinders was evident in the CT scans.

	Table 6.5-1. Service Projects	
Material/Component	**Objective**	**Results**
Metal knee joint	To develop a 3-D model of an artificial knee joint part based on CT data that will be used in a fluid flow analysis of this part.	Full-volume CT scan data were collected by taking multiple scans at small incremental steps in scan plane height throughout the volume of interest. The data were then used to develop a point cloud model of the part
Fiber Optic Guided (FOG) Missile bobbin	CRDA effort to examine through CT a FOG Missile bobbin wound with about 20 kilometers of fiber optic cable. The effort will attempt to detect differences in the wind after the bobbin has been subjected to thermal cycling. The bobbin has been designed to match the thermal properties of the fiber optic cable, so it is hoped that there will be no differences.	Several scans were made of the bobbin wound with the fiber optic cable. Scans through the longitudinal axis of the bobbin failed to show even a clear demarcation line between the bobbin and the wind. Scans perpendicular to the longitudinal axis showed details in the bobbin material, as well as a clear boundary between the bobbin and the fiber optic cable wind. The scans were repeated after thermal cycling and no changes were detected.
Small rocket motor nozzle	Feasibility scans to explore possibility of using the dual-energy capability of LAM/DE to reveal internal characteristics of a silicon nitride rocket nozzle formed by a fused deposition modeling technique.	The walls of the rocket nozzle were too thin for LAM/DE to be able to resolve any significant compositional changes within the walls.
Missile seeker head	Feasibility scans to demonstrate the possible use of LAM/DE for determining internal construction and composition of foreign military components without destruction of the part. An unclassified missile seeker head was scanned with the idea of obtaining data for radar cross-section calculation and modeling.	Scans were made at half-millimeter increments to form a volume scan of a portion of the seeker head. The scan data were evaluated using 3D visualization and modeling software to explore possibility of using CT data in examining hardware for classified programs.
Carbon fiber billet	To study the densification process on a carbon fiber billet. CT scans will be made to show the density of the billet throughout its 7-in by 10-in by-10-in volume. Scans will then be made after each step of the densification process.	Twenty-eight scans were made at quarter-inch increments to cover 7 inches in the Z-axis. The billet was then returned to Phillips Laboratory for succeeding steps in the densification process. The scans were repeated three more times at different stages of the process. After machining and additional densification, the billet was returned a fifth time

	Table 6.5-1. Service Projects	
Material/Component	**Objective**	**Results**
Zirconia pellets	To study the density distribution in zirconia pellets compacted by differing compaction techniques. This is a continuing effort to find applications for CT in the ceramics and castings community.	Numerous scans of samples created using different compaction techniques were completed. The images were best if only a single pellet were scanned at a time.
Stiff composite rod material used for fishing poles	To examine the internal structure of the rod material to explore possibilities of using CT in production quality control.	Four rods were scanned together. The internal structure could be seen, but the resolution of LAM/DE is not sufficient to provide any useful results.
Steel sample from canceled nuclear power plant	To provide data that will be used to compare and correlate data taken on the same sample using radiography and ultrasonics.	A complete volume scan was completed for the rectangular steel sample. The features of interest resulting from a repair weld were clearly shown and precisely located within the volume.
Power steering cylinder	To examine the injection-molded portions of the part for manufacturing defects, such as internal voids and porosity.	The portion of the part that was scanned showed some definite voids or very low-density pockets in critical areas. A single slice through a second part in the same region also showed the same problem.
Rotor clips for brake disks	To determine if CT could be used to detect casting defects in a specific area of the small steel parts.	After a couple of feasibility scans, it was found that no conclusive evidence of any casting defect could be shown using LAM/DE.
Snowmobile helmet	To determine the utility of CT scans in assessing damage to helmets after impact testing.	The feasibility scans did show internal damage to the helmet as a result of impact testing. The utility of the data for analysis weighed against the cost of obtaining it needs to be assessed.
Composite fiber filters	To provide density distribution data for evaluation of the manufacturing processes.	Density distribution data was obtained from two filters that were in different stages of manufacturing for evaluation of the manufacturing processes.
Composite pipe sections	To provide density distribution data for evaluation of the manufacturing processes.	Composite pipe sections from two different manufacturers were scanned at the same time to provide a graphic demonstration of the differences in manufacturing processes.
Ablative rocket nozzle chamber	To verify that LAM/DE can provide scans similar to ones performed at Hill AFB in anticipation of some future work.	Scans showed separations or voids in the asbestos layer in the sample section of a rocket nozzle chamber that was sent. The data was similar to data taken at the Hill AFB facility.

Table 6.5-1. Service Projects		
Material/Component	**Objective**	**Results**
Metal matrix composite ring	To investigate density variations within the ring assembly.	No density variations could be distinguished within the ring assembly. Crosstalk effects were more pronounced than any real density variations.
Titanium cubes manufactured through laser deposition of powdered metal	To determine if there is any density variation within the bulk material.	The material appeared very uniform in density. Cross talk artifacts were the only noticeable features in the scans. Images and density profiles were provided.
Automobile tire	To determine if CT scans could be used to evaluate delamination within the tire.	Only a portion of the full tire could be scanned due to field-of-view limitations, but the internal construction could be seen.
Copper billets used for an experimental aluminum extrusion process	To provide digital radiographs of the copper billet to show the quality of an aluminum extrusion within the copper billet.	Preview images provided digital radiographs of the copper billet to show the quality of an aluminum extrusion within the copper billet. These scans were for a manufacturing process study.
F-15 wing spar	To provide metrology data of sufficient density to build a good 3D model of a 28-inch-long F-15 wing spar for a reverse engineering study.	324 slices at a Z-increment of 1 mm were completed. A 3D model was then developed from the data.
C/SiC turbine rotors	To provide density distribution data to the manufacturer of the turbine rotors to aid them in failure analysis and developing improved manufacturing processes.	Density data was supplied on a failed rotor, a machined rotor before testing, and a pre-machined rotor. Material density variation was noticed to correspond with the machining that was done to balance the rotors. Material delaminations were also observed.
Aging aircraft parts	To demonstrate the capability of CT to provide data that can be used to develop accurate CAD drawings of out-of-production parts.	A volume scan of a steel pin was performed to provide data to a contractor for their effort in reverse engineering of aging aircraft parts.
Composite parts for the Army	To compare the capability of LAM/DE with an Army CT scanner by duplicating scans of parts already scanned by the Army.	The scans were very similar.
Lug section of an F-22 AFT body titanium casting	To demonstrate the capability of CT to find defects that are difficult to find using film radiography.	Twenty out of twenty-one artificial defects machined into the lug section were easily found in the LAM/DE scans.

	Table 6.5-1. Service Projects	
Material/Component	**Objective**	**Results**
Fossilized dinosaur eggs	To determine if there is any internal structure that could be attributed to an embryonic dinosaur.	Numerous scans were performed on a small collection of fossilized dinosaur eggs. There wasn't anything that could be identified as an embryonic dinosaur.
High-performance low-density composite material	To determine density and density gradients within the material to aide in the improvement of the production process	Gross density data was obtained and provided for a CTeC program.
Drilling core samples	To investigate the use of CT as an alternate method of measuring density within drilling core samples.	Density data was provided on drilling core samples of rock formations to Ohio Department of Natural Resources under a CTeC effort.
Aircraft fuel pump inlet housing	To provide scan data that could be used to create a 3D image file that could then be used by the manufacturer to compare the casting to the original design represented by a CAD file.	A full-volume scan was performed on the aluminum casting for a developmental inlet housing for an aircraft fuel pump assembly. The scan data was converted to an STL file and provided to the manufacturer.
Stir-welded aluminum plate	To examine a sample weld to determine if the equipment at the CT Facility could be used to evaluate the quality of the weld.	Neither the DR nor the CT capabilities of LAM/DE proved useful in revealing anomalies in the weld.
Automobile engine mounts	To verify and characterize defects in the parts to help validate other more cost-effective techniques of inspecting the parts.	Engine mounts that had failed or had known defects in the casting were scanned. The CT scans showed that LAM/DE could image the defects in the castings. UDRI is looking at other, more cost-effective NDE techniques to find these defects, but LAM/DE data could be very useful in validating the other techniques.
F-15 gridlock sections	To determine if CT could be used to inspect the finished product for proper insertion of the ribs into the channels on the interior.	We found that the resolution of LAM/DE was not sufficient to inspect these areas
Aluminum engine block	To determine if LAM/DE could produce good images of a large aluminum part.	The feasibility scans were surprisingly good and only a little noisy for long attenuation-length paths.
Developmental rail gun assembly	To inspect the parts of the rail gun as it is being assembled for defects in manufacture.	The CT scans showed the presence and extent of delaminations in the composite material used to construct the assembly.

Table 6.5-1. Service Projects		
Material/Component	**Objective**	**Results**
Aluminum alloy formed by extrusion	To provide density data on the aluminum alloy formed from powder through an experimental process.	Unfortunately, the aluminum was extruded within a copper ingot. The CT images could provide general dimensional information about the aluminum, but could not provide good density data due to artifacts from the copper ingot.
SiC composite disk samples	To demonstrate the ability of CT to provide meaningful density data within the sample disks.	The CT scans provided density gradient data throughout the disks and revealed an internal crack in one of the disks.
Lithium battery for the Navy	To determine if LAM/DE has sufficient energy and resolution to investigate problems in large lithium batteries.	The scans showed sufficient detail to reveal some of the problems that the Navy was looking for.
Turbine blades	To generate a 3D model of the base of the turbine blade and to look for evidence of microshrink in a critical region of the blade.	Three turbine blade parts were scanned. Eighty-five CT scans at 0.5 mm increments in height were completed on the first part to provide data to build a 3D model of the attachment end of a turbine blade. The resulting STL file was provided, but the conversion of the STL file to a file that could be used in a CAD program is considerably more work. The other two turbine blade parts were scanned, but no evidence of microshrink was detected in the area of interest.
Concrete core samples	To find anomalies in the material that might contribute to structural deficiencies.	We were able to show some evidence of cracks, as well as the normal density variations between the rocks, cement, and voids in the concrete.
Composite arbor	To find separations in the composite layers that might cause the material to fail at high rotational speeds.	No separations in the layers were detected.
Cast iron intake manifold	To determine if LAM/DE could be used through a CTeC effort to provide scans to reverse engineer an automobile engine manifold that is no longer manufactured.	Although the image was surprisingly good, it was inadequate for the desired task. The scan artifacts for regions containing long path lengths for x-ray absorption were too disruptive for producing threshold contours.

Section 7
System Upgrades, Maintenance, and Repair

7.0   HIPSAM I

7.0.1   Operating-System and Scan-Control Software

Requirements for hardware upgrades to the HIPSAM I system, e.g., scan axis motors, necessitated the installation of newer operating-system and scan-control software. The WIN95 operating system was installed and scan-control modules were developed in the LabWindows/CVI development system. New parallel I/O and GPIB boards have been tested and partially integrated into the system. A user-friendly graphical users' interface has been written and tested, while the first of the 6 scanner capabilities is near completion.

7.0.2   Signal-Tracking Capabilities

Two new software algorithms were implemented for determining the arrival times of low-amplitude, flat-peaked signals. The problem occurs because of the necessity for simultaneous single-channel acquisition of adjacent high- and low-amplitude transient signals. Because of the limited 8-bit digitizer used for this purpose, the low-amplitude signal had ill-defined (flat-topped) maximums. Two different algorithms were developed. One estimates the "true" location of the peak signal from the leading and trailing non-flat parts of the low-amplitude signal; the other locates zero crossings of the low-amplitude signal. Both of these techniques have been tested and implemented.

7.1   Material Properties Scanning System (MAPSS)

MAPSS is a digital ultrasonic data acquisition system with high mechanical precision (0.001 mm resolution) and high-frequency (up to 100 MHz) insonification capabilities. This currently-under-development system represents a significant upgrade relative to the HIPSAM system. At the present time, it can only acquire software-gated C-scan type data, but as development continues, it will be capable of acquiring digitized A-scan data and multiple (three-dimensional) B-scan data. The configuration, capabilities, and specifications as they exist at the time of this writing are provided in Tables 7.1-1, 7.1-2, and 7.1-3. The configuration, capabilities, and specifications will change as the development continues.

Table 7.1-1 Major Features and Specifications for MAPSS

Feature	Specification
Maximum transducer frequency	100 MHz
Maximum A-scan digitizing rate	2 gigasamples/secend
Maximum number of points per A-scan	16384 points
Maximum B-scan storage size	4 megabytes
Maximum image display dimensions	1024 by 1024 pixels
Time-Of-Flight (TOF) resolution	16 bits
Amplitude resolution	8 bits
Maximum dimensions of C-scan	1024 points by 16384 lines
Number of simultaneous software gates	6
Maximum scanning resolution	0.001 mm (0.00004 in.)
Maximum scan length	101.6 mm (4 in.)
Maximum scan width	101.6 mm (4 in.)
Scan and index axes	Any paired combination of X, Y, Z

Table 7.1-2. MAPSS Control and Software Collection Capabilities and Features

Item	Capability or Feature
B-Scan Data Collection	• Single-line scans • Gated scans – store all and/or selected portion of each A-scan
C-Scan Data Collection	• Minimize scan times by collecting scans on the fly as opposed to stop-start method • Amplitude data collection option for each software gate includes: Peak To Peak, Positive Peak, Negative Peak, Absolute Peak, and Mean Value. • TOF data collection option for each software gate includes: Positive, Negative, and Threshold Crossing. • User-defined 8- or 16-bit resolution TOF data collection and data storage • Precise post-data-collection transducer positioning in X, Y, and Z to collect smaller-area higher-resolution scan
Display	• Simultaneous display of up to 4 scan images from software gates during data collection • Each scan image can have an individual color map during scan collection • Auto-contrast function to conveniently maximize detail during initial scan • User-defined color maps can be added easily • Full screen display of any of the scan images
Gate Selection	• Optional automatic focus on a gate • Mouse wheel integration to maximize ease of use • Measuring tools to allow simple waveform analysis by the user during gate selection • Gate creation and manipulation optimized for mouse input • Separate map of the waveform display provides reference point when zooming in • Gate width displayed in terms of microseconds, data points, and frequency simultaneously • Optional automatic tracking of positive or negative peak within a gate

Table 7.1-2 *(Cont'd.).* **MAPSS Control and Software Collection Capabilities and Features**

Item	Capability or Feature
Motor Control	• Visual feedback to user to show when motor is moving • Ability to move in terms of absolute and local position • User-defined search box allows quick and precise movements along scanning area • Intuitive motor controlling with ability to rotate axis in search box • Feedback of motor location during scans
Error Handling	• Additional error and instruction messages to assist operator • Device errors are output to the user
Miscellaneous	• Data collection and display algorithms integrated into a single program • Optimum motor-speed computation algorithm • New control-file options to make MAPSS-generated control files compatible with pre-existing data • UDRI-developed analyses and signal/image-processing algorithms on both VAX and PC-based systems • Software-controlled, hardware-induced trigger delay • National Instruments Digital Data Acquisition (NI-DAQ) library • Windows XP style operator interface with CVI 6.0 • Emergency stop button available whenever user causes motor movement • Ability to pause or stop scans midway through without losing any data already collected • Reload software settings from any previous scan through scan's control file for easy repeatability

Table 7.1-3. MAPSS Hardware and Software Systems and Specifications

System or Subsystem	Item/Specifications
Computer Hardware	• 800 MHz Pentium III processor with 256 MB of RAM • ICS 15-slot chassis, 300 W power supply • Floppy disk • Zip 100 MB disk • DVD/CDRW disk • 19.0 GB system disk • 27.9 GB user disk • Intel 82810E graphics interface with a 21" Sony monitor • ATI Rage II graphics interface with a 19" Dell monitor • Network interface • National Instruments PCI-DIO-32HS parallel interface • National Instruments GPIB/TNT IEEE-488.2 interface
Scanner Hardware and Specifications	• Aerotech Unidex 500 PCI three-stage scanner • Machine resolution – 0.0005 mm (0.000019685 in) • Programming resolution – 0.001 mm (0.0001 in) • Maximum speed – 440,000 steps/sec or 26400 mm/min (1039.37 in/min) • Maximum travel – X,Y, Z – (101.6 mm by 101.6 mm by 101.6 mm) • PC-PSO DSP-Based Programmable Output Control Card
Digitizer	• Tektronix RTD 720A Digitizer • 2 input channels • External clock and trigger • 4194304 maximum points per waveform • 10 MS/s – 2 GS/s collection rates
Signal Generation and Conditioning	• SRS Delay Generator • Panametrics Pulser/Receiver
Software	• Windows 98 second edition • MS Office (Word and Excel) • National Instrument LabWindows/CVI 6.0 – 32 bit real time development system

7.2   X-Ray CT – Tomoscope

7.2.1   Ring and Beam-Hardening Correction Algorithm

The Tomoscope CT system acquires data using a typical rotate-only scan geometry. With this data acquisition scheme, any mismatch in detector response to the incident x-ray beam will result in ring artifacts in the CT image. Ring artifacts is a term used to describe correlated noise in an image that appears as concentric rings, similar in appearance to growth rings in wood.

Depending on their severity, ring artifacts in an image can be a minor effect that does not mask the underlying data, or they can greatly diminish the diagnostic utility of the image. Typically, the artifacts have little effect on the qualitative usefulness of the image, but they always impact the quantitative nature of the image.

Software for detector corrections was written. It includes the corrections for the nonlinear response of detectors. The detector response was modeled as a zero-intercept quadratic function of the thickness of the material along the ray-path. This has effectively eliminated the "cupping" phenomenon in the reconstructed image caused by beam hardening. The ring artifacts have also been significantly reduced. The software also eliminates random streaks artifacts and increases the image sharpness and contrast. Near the center, rings appear harder to eliminate, and further study is recommended.

A report for this project was written and provided to AFRL/MLLP personnel. That report is not included with this final report.

7.2.2   Gantry System

An analysis of the Tomoscope system conducted on a separate contract identified the gantry control computer, the gantry control software, and the gantry control electronics, motors, and stages as the subsystems meriting the highest priority for the upgrade program. Supportability was a major concern for each of these subsystems. The Tomoscope gantry control computer was a Compaq 386-processor-based PC, which included several one-of-a-kind, wire-wrap processor boards. The gantry control interface module also included aging wire-wrap boards. The gantry motors and stages were manufactured by a now defunct company, making repair and support difficult.

The Tomoscope gantry control computer, gantry control software, gantry control module, gantry motors and gantry stages were all replaced. The new system utilizes Aerotech's software motor control system linked to digital motor amplifiers through a FireWire connection. The software resides on a modern PC running the Windows XP operating system. The control system is accessed through software that fully duplicates the functionality of the former gantry control software, including replicating the exact interface with the Tomoscope scan control system. The software was written in Visual Basic to allow maximum future supportability.

The separate contract concluded prior to final installation of the upgraded hard-ware and software for the Tomoscope CT system. The upgrade was then completed on this On-Site NDE contract.

Two documents for this effort were written by ARACOR and provided to AFRL/ MLLP personnel. These documents are not included with this final report.

7.2.3 Detector Control Modules

A failed detector control module was sent directly to Princeton Instruments, Inc. for repair, since they built the original circuit boards. Fortunately, they were able to repair the module. The module that had been kept by David Saar to aid in troubleshooting of other modules was returned to the CT Facility. Two of the other spare modules may have problems that could be fixed by Princeton Instruments.

7.2.4 FeinFocus X-Ray Tube

Vacuum in the FeinFocus x-ray tube was an occasional problem that was most often solved by cleaning interior surfaces and replacing o-rings.

The fiber optic communication link between the FeinFocus control chassis and generator caused problems from time to time. One time it was fixed by eliminating a short length of fiber optic cable in the generator, and another time it was fixed when we discovered an internal ribbon connector that was not seated properly.

The roughing vacuum pump developed an oil leak due to a design problem and was replaced with a newly designed pump.

The overall performance of the FeinFocus x-ray source was a problem for a long time after it was purchased. Frequently, it would shut down during a scan due to a generator breakdown. Finally, the tube was upgraded, at no cost to the government, by replacing the entire head and control cards. After some initial integration problems during the break-in period, it became much more reliable and has been functioning well ever since.

7.3   X-Ray CT – LAM/DE

7.3.1   Source-Side Resolution Apertures

A simple design for a source-side resolution aperture was developed for LAM/DE to provide an inexpensive enhancement to the resolution capability of the system. The design concept is an aperture plate with 72 1-mm grooves machined into it that would each lie on a source-to-detector path, effectively reducing the x-ray spot size for each detector. The machined aperture plate is inserted into the existing steel source-side aperture block. It is easily inserted or removed depending on the desire for higher resolution scans. The design was sent to a local precision machine shop for machining. Tests of the system with the new source-side resolution apertures yielded better than a 43% increase in the spatial resolution of the system with 1024 × 1024 images. An 89% increase in spatial resolution was achieved with 2048 × 2048 images.

7.3.2   Gantry

An intermittent problem causing corrupted and shifted data in sinograms for many months was finally fixed by replacing one of the four brushes in the tachometer, which is located in the motor assembly that drives the x-axis.

The Sony Magnescale on the gantry x-axis was damaged during troubleshooting and was then sent back to Sony for repair. Sony found that reversing the direction of the rod and replacing the read head would repair the damage caused to the Magnescale.

A problem with abnormal vibration when the gantry was driven in the X-direction was solved. After a serious examination of the control circuits and documentation, several troubleshooting conversations with Fanuc service technicians, and some help from on-site personnel, it was finally discovered that there was a misplaced jumper on the X-axis servo control card that attenuates the feedback in the control loop. Apparently, this had been a problem, perhaps from the beginning. As the equipment aged, the problem became

much more noticeable. When the jumper was correctly positioned, the vibration disappeared. The gantry is now working better than it has ever worked. Scans with short integration times that would not run before can now be run. The scanner would frequently fail when the field of view was set below 150 mm. Now, it seems to run with no problems with even smaller fields of view.

7.3.3 Array Processor

Replacing bad boards with functional boards obtained from residual array processors obtained from Hill AFB solved some problems with the LAM/DE array processor. Burning programs onto new PROMs and exchanging the new ones for those with corrupted programs solved other problems. Additional spare array processors were later obtained from Johns Hopkins University from a Navy contract that was upgrading their computer equipment. With the spare array processor equipment now available, any future array processor problems should not be fatal to the LAM/DE system.

7.3.4 Motorola Scan Control Computer

The disk control card in the Motorola scan control computer failed. Fortunately, we had a spare in the equipment we received from Hill AFB when they upgraded their system.

We were able to successfully make additional backups of the LAM/DE Motorola scan control computer. Previously the only backup was on 5-1/4-inch floppy disks. We found some 5-1/4-inch floppy disks and made an additional backup. We also installed the spare 40 M hard drive in the Motorola computer obtained as excess from Hill AFB and loaded all the LAM/DE software files onto that drive. We now have a spare hard drive with the required files already loaded.

7.3.5 X-Ray Source

A new Seifert x-ray tube was purchased and installed in LAM/DE since the existing tube had long since exceeded its normal lifetime prediction. Although the old tube continued to perform well until it was removed, we could not depend on its continued performance. Keeping the new tube as a spare until the old tube failed was not a viable option because the new tube would degrade if not put into use.

At different times, both the positive and negative high-voltage generators for the Seifert x-ray tube had to be sent back to the factory for repair of cracked sockets. In both instances, the generators were refurbished and returned in a couple of weeks.

7.3.6   Application Software

The version of MAESTRO has been upgraded on the Alpha computer system several times during the program. There was no charge to the Air Force for these upgrades. The MicroVAX continues to run on a much older version of MAESTRO and cannot be upgraded to the latest version. The latest version enhances our ability to reconstruct, display, and analyze CT images once the MicroVAX has collected the data.

7.3.7   Data Archive

The image archive data that was stored on nearly three hundred large ½-inch magnetic tape reels was transferred to a single 80-gigabyte hard drive archive. Now, nearly all scans that have been completed on LAM/DE are immediately available for viewing on the Alpha workstation. The data on nineteen remaining tapes could not be completely transferred due to problems reading the magnetic tape. These reels have been retained for future attempts to retrieve the data. All other tapes have been taken to the shredder for disposal.

The Scan Record database that was formerly hosted on a Macintosh Power PC in 4th Dimension has been converted to a Microsoft Access database. All the data in the previous database was recovered from the failed hard disk of the Power PC, incorporated into this new database, and is now readily accessible on any PC with Microsoft Access.

Section 8
References

1. K.K. Liang, S.D. Bennett, B.T. Khuri-Yakub, and G.S. Kino, "Precise Phase Measurements with the Acoustic Microscope", *IEEE Trans. Sonics and Ultrasonics,* Vol. Su-32, No. 2, pp. 266-273, March 1985.

2. M. Obata, H. Shimada, and T. Mihara, "Stress Dependence of Leaky Surface Wave on PMMA by Line Focus Beam Microscope", *Exp. Mech.* 30, pp. 34-39 (1990).

3. Y.C. Lee, J.O. Kim, and J.D. Achenbach, "Measurement of Stresses by Line Focus Acoustic Microscopy", *Ultrasonics* 32, p. 359 (1994).

4. S. Sathish, R.W. Martin, and T.E. Matikas, "Rayleigh Wave Velocity Mapping Using Scanning Acoustic Microscope" *Review of Progress in QNDE*, Vol. 18B, pp. 2025-2030, Eds. D.O. Thompson, D. E. Chimenti, Plenum Press, New York (1999).

5. S. Sathish and R.W. Martin, "Development of a Scan System for Rayleigh, Shear, and Longitudinal Wave Velocity Mapping", *Proceedings of the 1999 IEEE International Ultrasonics Symposium*, Lake Tahoe, Nevada, October 17-20, 1999.

6. G. Piersol, "Time Delay Estimation Using Phase Data", *IEEE Trans. Acoustics, Speech, and Signal Processing*, Vol. ASSP-29, No. 3, pp. 471-477, June 1981.

7. L. Kostić, "Local Steam Transit Time Estimation in a Boiling Water Reactor", *IEEE Trans. Acoustics, Speech, and Signal Processing*, Vol. ASSP-29, No. 3, pp. 550-560, June 1981.

8. D.W. Hoeppner, "Mechanisms of Fretting-Fatigue and Their Impact on Test Methods Development" in *ASTM-STP 1159*, pp. 23-32, 1992.

9. P. Blanchard, C. Colombie, V. Pellerin, S. Fayeulle, and L. Vincent, *Metallurgical Transactions*, Vol. 22A, p. 1535, (1991).

10. E. Shell, T. Matikas, and P. Nicolaou, "Nondestructive Evaluation of Fretting Damage in Jet Engine Materials", *Proceedings of SAMPE 2000 Conference*, Long Beach, CA, May 1999.

11. S. Suresh, "Fatigue of Materials", 2nd ed., Cambridge University Press, New York (1998).

12. J.A. Collins, "Failure of Materials in Mechanical Design", John Wiley, New York (1993).

13. S.J. Basinski, Z.S. Basinski, and A. Howie, "Early Stages of Fatigue in Copper Single Crystals," *Phil. Mag.,* Vol. 19, p. 899 (1969).

14. U. Essman, U. Gosele, and H. Mughrabi, "A Model for Extrusion and Intrusions in Fatigued Metals," *Phil. Mag.,* Vol. A44, p. 405 (1981).

15. C. Laird, J.M. Finney, and D. Khulmann-Wilsdorf, "Dislocation Behavior in Fatigue IV: Variation in the Localization of Strain in Persistent Slip Bands", *Materials. Science and Engineering,* Vol. 50, p. 127 (1981).

16. A. Puskar and S.A. Golovin, "Fatigue in Materials: Cumulative Damage Processes", Elsevier, New York (1985).

17. O. Buck, "Harmonic Generation for Measurement of Internal Stresses as Produced by Dislocations", IEEE Transactions on Sonics and *Ultrasonics,* Vol. SU-23, pp. 346-350 (1976).

18. J.H. Cantrell and W.T. Yost, "Acoustic Harmonic Generation from Fatigue-Induced Dislocation Dipoles", *Phil. Mag.,* Vol. A69, pp. 315-3269 (1994).

19. P.B. Nagy, "Fatigue Damage Assessment by Nonlinear Ultrasonic Materials Characterization", *Ultrasonics,* Vol. 36, 375-381, (1988).

20. J.K. Na, J.H., Cantrell, and W.T. Yost, "Linear and Nonlinear Ultrasonic Properties of Fatigued 410Cb Stainless Steel", in *Review of Progress in Quantitative Nondestructive Evaluation*, Vol. 15, eds., D.O. Thompson and D.E. Chimenti, pp. 1347-1351 (1996).

21. H. Ogi, M. Hirao, and S. Aoki, "Noncontact Monitoring of Surface-Wave Nonlinearity for Predicting the Remaining Life of Fatigued Steels", *J. Appl. Phys.*, Vol. 90, pp. 438-442 (2001).

22. K.Y. Jhang and K.J. Kim, "Evaluation of Material Degradation Using Nonlinear Acoustic Effect", *Ultrasonics,* Vol. 37, pp. 39-44 (1999).

23. J. Frouin, S. Sathish, T.E. Matikas, and J.K. Na, "Ultrasonic Linear and Nonlinear Behavior of Fatigued Ti-6Al-4V", *J. Materials. Res.,* Vol. 14, p. 79 (1999).

24. J. Frouin, "Linear and Nonlinear Acoustic Behavior of Titanium Alloys Under Cyclic Loading", Ph. D Thesis, University of Dayton (2001).

25. A. Hikata and C. Elbaum, "Generation of Ultrasonic Second and Third Harmonics Due to Dislocations", *Phys. Rev.,* Vol. 144, p. 469 (1966).

26. H. Gu, H. Guo, S. Chang, and C. Laird, "Orientation Dependence of Cyclic Deformation in High Purity Single Crystals", *Materials Science and Engineering,* Vol. A188, pp. 23-26 (1994).

27. J. Maurer, "Characterization of Accumulated Fatigue Damage in Ti-6Al-4V Plate Material Using Transmission Electron Microscopy and Nonlinear Acoustics", Ph. D Thesis, University of Dayton (2001).

28. W. Hoppe, R. Ko, J. Pierce, and N. Schehl "Assessment of Nondestructive Inspection Methods for Corrosion Detection," presented at the *12th AeroMat Conference & Exposition*, Long Beach, CA, June 12-13, 2001.

29. W. Hoppe, J.L. Pierce, R. Ko, D. Buchanan, N. Schehl, J. Brausch, and K. LaCivita, "Results from the Hidden Corrosion Detection Evaluation on the Automated Corrosion Detection Program – Supporting Tests and Specimen Characterization," *Proceedings of the Fifth Joint NASA/FAA/DoD Conference on Aging Aircraft*, Orlando, FL, Sept. 10-13, 2001.

30. W. Hoppe, J.L. Pierce, R. Ko, N. Schehl, and D. Buchanan, "Results from the Hidden Corrosion Detection Evaluation on the Automated Corrosion Detection Program – Probability of Detection," *Proceedings of the Fifth Joint NASA/FAA/DoD Conference on Aging Aircraft*, Orlando, FL, Sept. 10-13, 2001.

31. H.L. Libby, "Introduction to Electromagnetic Nondestructive Test Methods", John Wiley & Sons, New York (1971).

32. D. Raizenne., W. Wu, and C. Poon, "In-Situ Retrogression and Re-Aging of Al 7075-T6 Parts," in *Proceedings of the Fifth Joint NASA/FAA/DoD Conference on Aging Aircraft*, Orlando, FL, Sept. 10-13, 2001.

33. D. Raizenne, P. Sjoblom, R. Rondeau, and J. Snide, "Retrogression and Re-Aging (RRA) of New and Old Aircraft Parts," in *Proceedings of the 6th Joint FAA/DoD/ NASA Conference on Aging Aircraft*, San Francisco, CA, Sept.16-19, 2002.

34. J.H. Cantrell and W.T. Yost, "Effect of Precipitate Coherency Strains on Acoustic Harmonic Generation," *J. Appl. Phys*. 81 (7), pp. 2957-2962 (1997).

35. J.H. Cantrell and X.G. Zhang, "Nonlinear Acoustic Response from Precipitate-Matrix Misfit in a Dislocation Network", *J. Appl. Phys*. 84 (10), pp. 5469-5472 (1998).

36. J.H. Cantrell and W.T. Yost, "Determination of Precipitate Nucleation and Growth Rates from Ultrasonic Harmonic Generation," *Applied Physics Letters*, 71 (13), pp. 1952-1954 (2000).

Appendix A
Publications Included with this Report

1. S. Sathish and R.W. Martin, "Quantitative Imaging of Rayleigh Wave Velocity with a Scanning Acoustic Microscope", *IEEE Trans. Ultrasonics, Ferroelectrics and Frequency Control,* Vol. UFFC-49, No. 5, May 2002, pp. 550-557.

2. S. Sathish and R.W. Martin, "Development of a Scan System for Rayleigh, Shear and Longitudinal Wave Velocity Mapping", *1999 IEEE International Ultrasonics Symposium*, Lake Tahoe, Nevada, October 17-20, 1999.

3. S. Sathish and R.W. Martin, "Scanning Acoustic Microscopy and X-Ray Diffraction Investigation of Near Crack Tip Stresses", in *Materials Research Society Symposium Proceedings Vol. 591: Nondestructive Methods for Materials Characterization*, Eds. G.Y. Baakalini, N. Meyendorf, and R.S. Gilmore, pp. 55-60, 1999.

4. S. Sathish, T. Matikas, and R.W. Martin, "Rayleigh Wave Velocity Mapping Using Scanning Acoustic Microscope", Review of Progress in Quantitative Nondestructive Evaluation, Vol. 18B, eds. D.O. Thompson and D.E. Chimenti, 1999, pp. 2025-2030.

5. S. Sathish, R.W. Martin, and T.J. Moran, "Local Surface Skimming Longitudinal Wave Velocity and Residual Stress Mapping", in *J. Acoust. Soc. Am.*, Vol. 115, No. 1, January 2004.

6. S. Sathish, R. Martin, R. Reibel, M.J. Ruddell, and T.J. Moran, "Local Phase Measurements with Focused Acoustic Transducer," *Proceedings of IEEE Ultrasonics Symposium* (2001).

7. R.W. Martin, S. Sathish, B.G. Frock, and T.J. Moran, "Ultrasonic Measurement of Stress in Titanium Alloys," *Proceedings of the Instrumentation Society of America*. Denver, CO, (2001).

8. R.W. Martin, S. Sathish, R. Reibel, T.J. Moran, and M.P. Blodgett, "Acoustic Interferometer for Localized Rayleigh Wave Velocity Measurements," in *Review of Progress in Quantitative Nondestructive Evaluation, Bellingham, Washington, 14-19 July 2002, AIP Conference Proceedings*, Vol. 22A, eds. D.O. Thompson and D.E. Chimenti, American Institute of Physics, Melville, New York, 2003, pp. 875-882.

9. S. Martinez, S. Sathish, M.P. Blodgett, S. Namjoshi, and S. Mall, "Residual Stress Relaxation Due to Fretting Fatigue in Shot Peened Surfaces of Ti-6Al-4V", in *Review of Progress in Quantitative Nondestructive Evaluation, Bellingham, Washington, 14-19 July 2002, AIP Conference Proceedings*, Vol. 22B, eds. D.O. Thompson and D.E. Chimenti, American Institute of Physics, Melville, New York, 2003, pp. 1531-1538.

10. S.A. Martinez, S. Sathish, M.P. Blodgett, and M.J. Shepard, "Residual Stress Distribution on Surface-Treated Ti-6Al-4V by X-Ray Diffraction", in *Experimental Mechanics*, Vol. 43, No. 2, June 2003.

11. R.T. Ko, "The Use of a Giant Magnetoresistive (GMR) Sensor for Characterization of Corrosion in a Laboratory Specimen", in *Proceedings of the 6th Joint FAA/DoD/NASA Aging Aircraft Conference*, San Francisco, CA, Sept. 16-19, 2002.

12. R.T. Ko and M.P. Blodgett, "Application of a Giant Magnetoresistive (GMR) Sensor for Characterization of Corrosion in a Laboratory Specimen", in *Review of Progress in Quantitative Nondestructive Evaluation, Bellingham, Washington, 14-19 July 2002, AIP Conference Proceedings*, Vol. 22, eds. D.O. Thompson and D.E. Chimenti, American Institute of Physics, Melville, New York, 2003.

13. R. Ananthula, R.T. Ko, S. Sathish, and M.P. Blodgett, "Characterization of Retrogression and Re-aging Heat Treatment of AA7075-T6 Using Nonlinear Acoustics and Eddy Current", in *Review of Progress in Quantitative Nondestructive Evaluation, Green Bay, Wisconsin, 2003, AIP Conference Proceedings*, Vol. 23, eds. D.O. Thompson and D.E. Chimenti, American Institute of Physics, Melville, New York, 2004.

14. J.S. Knopp, J.C. Aldrin, R.T. Ko, and H. Sabbagh, "Numerical and Experimental Study of Eddy Current Crack Detection Around Fasteners in Multi-Layer Structures", in *Review of Progress in Quantitative Nondestructive Evaluation, Green Bay, Wisconsin, 2003, AIP Conference Proceedings*, Vol. 23, eds. D.O. Thompson and D.E. Chimenti, American Institute of Physics, Melville, New York, 2004.

15. J.S. Knopp, H.A. Sabbagh, R.T. Ko, and J. C. Aldrin, "Modeling Eddy Current Crack Detection in Multi-Layer Airframe Structures Using the Volume-Integral Method", accepted for presentation at the *ACES 2004 Conference* to be held in Syracuse, New York from Apr. 19-23, 2004.

16. V.A. Kramb, J.P. Hoffmann, and J.A. Johnson, "Characterization of Weathering Degradation in Aircraft Polymeric Coatings Using NDE and Microscopic Imaging Techniques", in *Proceedings of the SPIE 7th Annual International Symposium "NDE for Health Monitoring and Diagnostics"*, San Diego, CA. (March 2002).

17. V.A. Kramb, J.P. Hoffmann, and J.A. Johnson, "Characterization of Weathering Degradation in Aircraft Polymeric Coatings Using NDE Imaging Techniques", in *Proceedings of the SPIE 7th Annual International Symposium "NDE for Health Monitoring and Diagnostics"*, San Diego, CA. (March 2002).

18. J.R. Sebastian and D.A. Stubbs, "Strain Measurement Using Surface Acoustic Waves", in *Review of Progress in Quantitative Nondestructive Evaluation, Ames, Iowa, July 16-20, 2000, AIP Conference Proceedings*, Vol. 20B, eds. D.O. Thompson and D.E. Chimenti, American Institute of Physics, Melville, New York, 2004.

19. C. Kropas-Hughes and E.L. Klosterman, "Simple Method to Examine the Alignment of a Residual Stress Measuring X-Ray Diffractometer", in *Materials Evaluation*, Vol. 60, No. 1, January 2002, p. 90.

Appendix B
Publications Not Included with this Report

1. S. Sathish, "Residual Stress Measurement with Focused Acoustic Waves and Direct Comparison with X-Ray Diffraction Stress Measurements", to be published in *Journal of Materials Science and Engineering*.

2. C.V. Kropas-Hughes and S.T. Neel, "Basics of Computed Tomography", in *Materials Evaluation*, Vol. 58, No. 5, May 2000, pp. 630-633.

Appendix C
Presentations Not Included with This Report

1. S. Sathish and R.W. Martin, "Acoustic Microscopy and X-Ray Diffraction Measurements of Stress in Ti6Al4V", presented at the "10th Annual Advanced Aerospace Materials and Processes Conference", Dayton, Ohio, June, 1999.

2. S. Sathish and R.W. Martin, "Surface Wave Velocity and Young's Modulus Imaging with a Scanning Acoustic Microscope", presented at the "10th Annual Advanced Aerospace Materials and Processes Conference", Dayton, Ohio, June, 1999.

3. S. Sathish and R.W. Martin, "Development of a Scan System for Rayleigh, Shear, and Longitudinal Wave Velocity Mapping", presented at the 1999 IEEE International Ultrasonics Symposium, Oct. 17-20, 1999, Tahoe, Nevada, NV.

4. S. Sathish and R.W. Martin, "Scanning Acoustic Microscopy and X-Ray Diffraction Investigation of Near Crack Tip Stresses in Ti-6Al-4V", presented at the 1999 Materials Research Society Fall Meeting: Symposium on Nondestructive Methods for Materials Characterization, Nov. 29-Dec. 3, 1999, Boston, MA.

5. R.W. Martin, S. Sathish, B.G. Frock, and T.J. Moran, "Ultrasonic Measurement of Stress in Titanium Alloys", presented at the ISA Conference in May 2001.

6. R.W. Martin and S. Sathish, "Measurement of Acousto-Elastic Constant of Ti-6Al-4V Using Scanning Acoustic Microscope", presented at the 11th AeroMat Conference, Bellevue, Washington, June, 2000.

7. R.W. Martin and S. Sathish, "Near Surface Stress Studies with X-Ray Diffraction and Scanning Acoustic Microscopy", presented at the 11th AeroMat Conference, Bellevue, Washington, June, 2000.

8. J. Blackshire and S. Sathish, "Characterization of Micro-Electro-Mechanical (MEMS) Ultrasonic Transducers Using Laser Intereferometry," presented at the Ultrasonics International 2001 Conference, Delf, The Netherlands. (July 2001).

9. V.A, Kramb. J.P, Hoffmann, and J.A, Johnson, "Characterization of Weathering Degradation in Aircraft Polymeric Coatings Using NDE and Microscopic Imaging Techniques," presented at the 6th Joint Conference on Aging Aircraft, San Francisco, CA (September 2002).

10. J. Frouin, S. Sathish, and J.K. Na, "Evaluation of Nonlinear and Linear Acoustic Properties in Fatigue Damaged Ti-6Al-4V Samples," presented at the Ultrasonics International 2001 Conference, Delf, The Netherlands. (July 2001).

11. S. Sathish, R.W. Martin, R. Reibel, M.J. Ruddell, and T.J. Moran, "Local Phase Measurements with Focused Acoustic Transducer", presented at the 2001 IEEE International Ultrasonic Symposium, Atlanta, GA. (October 2001).

12. J. Blackshire and S. Sathish, "Scanning Laser Interferometric Evaluation of Individual Elements and an Entire Micro-Electro-Mechanical Ultrasonic Array Transducer", presented at the 2001 IEEE International Ultrasonic Symposium. Atlanta, GA. (October 2001).

13. R.T, Ko, "The Use of a Giant Magnetoresistive (GMR) Sensor for Characterization of Corrosion in a Laboratory Specimen", presented at the 6th Joint FAA/DoD/NASA Aging Aircraft Conference, Sept.16-19, 2002, San Francisco, CA.

14. C. Kropas-Hughes, S. Sathish, C. D. Daniels, M. Khobaib, E. L. Klosterman, R.W. Martin, and R. Reibel, "NDE for Corrosion Growth Rate in Aluminum", presented at ASNT Spring Conference 2003, March 10-13, 2003.

15. S. Sathish, T.J. Moran, R.W. Martin, and R. Reibel, "Residual Stress Measurement with Focused Acoustic Waves and Direct Comparison with X-Ray Diffraction Measurements", presented at TMS Conference, San Diego, CA, March 2003.

16. R. Ananthula and S. Sathish, "Characterization of Retrogression and Reaging (RRA) Process of Aluminum 7075-T6 using Nonlinear Acoustics", presented at the SPIE 2003 Conference, San Diego, CA, March, 2003.

17. V.A. Kramb, J.P. Hoffmann, and J.A. Johnson, "Characterization of Weathering Degradation in Aircraft Polymeric Coatings Using NDE Imaging Techniques", presented at the 28th Review of Progress in Quantitative Nondestructive Evaluation, 2001.

18. R.T. Ko and M.P. Blodgett, "Application of a Giant Magnetoresistive (GMR) Sensor for Characterization of Corrosion in a Laboratory Specimen", presented at the 29th Annual Review of Progress in Quantitative Nondestructive Evaluations, July 14-19, 2002, Bellingham, WA.

19. J.P. Hoffmann, V.A. Kramb, J.A. Johnson, and N. Meyendorf, "Characterization of EPOXY Coating Degradation Using NDE Imaging Techniques", presented at the SPIE 7th Annual International Symposium, NDE for Health Monitoring and Diagnostics, San Diego, CA (March 2002).

20. R.T. Ko and M.P. Blodgett, "Application of a Giant Magnetoresistive (GMR) Sensor for Characterization of Corrosion in a Laboratory Specimen", presented at the 29th Annual Review of Progress in Quantitative Nondestructive Evaluations, July 14-19, 2002, Bellingham, WA.

21. R.W. Martin, S. Sathish, R. Reibel, T.J. Moran, and M.P. Blodgett, "Acoustic Interferometer for Localized Rayleigh Wave Velocity Measurements", presented at the 29th Annual Review of Progress in Quantitative Nondestructive Evaluation, July 14-19 July 2002, Bellingham, WA.

22. J. Frouin, S. Sathish, and K. Na, "Nonlinear Behavior of Fatigue Fractured Ti-6Al-4V", presented at the International Conference on Fatigue Damage, 2002, Hyannis, Massachusetts.

23. V.A. Kramb, J. Hoffman, and J.A. Johnson, "Characterization of Weathering Degradation in Aircraft Polymeric Coatings Using NDE and Microscopic Imaging Techniques", presented at the *6th Joint FAA/DoD/NASA Conference on Aging Aircraft*, 2002, San Fransisco, CA.

24. C.V. Kropas-Hughes, S. Sathish, et. al., "Corrosion Growth Rate Study Using High Resolution Computed Tomography", presented at the *X-Ray CT Symposia of the 39th Annual Technical Meeting of the Society of Engineering Science (SES)*, 2002, Pennsylvania State University.

25. C.V. Kropas-Hughes, D. Daniels, et. al., "Computed Tomography at the Air Force Research Laboratory", presented at the *X-Ray CT Symposia of the 39th Annual Technical Meeting of the Society of Engineering Science (SES)*, 2002, Pennsylvania State University.

Appendix D
Unpublished Reports

1. C. Kacmar, "Corrosion and Fatigue Studies on Aluminum and Titanium Alloys".

2. Y. Prasad, "Feasibility of Using Acoustic Emission Techniques for Monitoring Metal Processing".

3. S. Huss, C. Daniel,s and W. Chang, "The 3D Compositional Distribution of Particulate Reinforced Composites: A Novel NDE Protocol".

Acronyms

ACES	Automatic Couplant Ejection System
AE	Acoustic Emission
AFM	Atomic Force Microscope
AFRL/ML	Air Force Research Laboratory/Materials and Manufacturing Directorate
AFRL/MLLP	Air Force Research Laboratory/Materials and Manufacturing Directorate; Metals, Ceramics and NDE Division, NDE Branch
ARACOR	Advanced Research and Applications Corporation
ATR-FTIR	Attenuated Total Reflection-Fourier Transform Infrared
C/SiC	Carbon/Silicon Carbide
CAD	Computer Aided Design
CEM	Corrosion Environment Monitor
CRADA	Cooperative Research And Development Agreement
CT	Computed Tomography
CTeC	Collaborative Technology Clusters
DoD	Department of Defense
DR	Digital Radiography
EMTEC	Edison Materials Technology Center
ERLE	Engine Rotor Life Extension
FAA	Federal Aviation Administration
FOG	Fiber Optic Guided
GMR	Giant Magnetoresistive
GPIB	General Purpose Interface Bus
HIPSAM	High Precision Scanning Acoustic Microscope
I/O	Input/Output
IACS	International Annealed Copper Standard
IR	Infrared
LAM/DE	Laminography/Dual Energy
LPB	Low Plasticity Burnishing
MAPSS	Material Properties Scanning System
MAUS	Mobile Automated Scanner
NASA	National Aeronautics and Space Administration
NDE	Nondestructive Evaluation
NFSI	Near Field Scanning Interferometry
PCMCIA	Personal Computer Memory Card International Association
POD	Probability of Detection
PROM	Programmable Read Only Memory
RRA	Retrogression and Reaging
RSRM	Reusable Solid Rocket Motor
RSW	Rayleigh Surface Wave
SAIC	Scientific Applications International Corporation
SAM	Scanning Acoustic Microscope
SAMPE	Society for the Advancement of Material and Process Engineering

SAW	Surface Acoustic Wave
SCR	Silicon Controlled Rectifier
SSLW	Surface Skimming Longitudinal Wave
SSSW	Surface Skimming Shear Wave
TEM	Transmission Electron Microscope
TOF	Time of Flight
UAV	Unmanned Aerial Vehicle
UDRI	University of Dayton Research Institute
UFM	Ultrasonic Force Microscope
UV	Ultra Violet
VHM	Vehicle Health Monitoring
WLIM	White Light Interference Microscope
XRD	X-Ray Diffraction